The identification and analysis of MHD waves in localised solar atmospheric wave guides

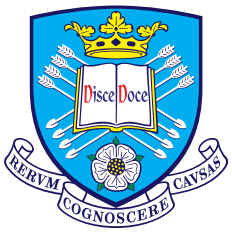

The University Of Sheffield.

Nabil Freij

Supervisor: Prof. Robertus Erdélyi

School of Mathematics and Statistics
University of Sheffield

This dissertation is submitted for the degree of
Doctor of Philosophy

September 2015

In memory of my father.

Declaration

I hereby declare that except where specific reference is made to the work of others, the contents of this dissertation are original and have not been submitted in whole or in part for consideration for any other degree or qualification in this, or any other university. This dissertation is my own work and contains nothing which is the outcome of work done in collaboration with others, except as specified in the text and Acknowledgements. This dissertation contains fewer than 65,000 words including appendices, bibliography, footnotes, tables and equations and has fewer than 150 figures.

Nabil Freij
September 2015

Acknowledgements

There are many people and organisations I would like to thank during the four years I have taken to complete my PhD.

First, the official acknowledgements. Starting with the people who created and maintain the telescopes and instruments who made this research possible. SDO/AIA and SDO/HMI data are used courtesy of NASA/SDO and the AIA and HMI science teams. The Swedish 1-m Solar Telescope is operated on the island of La Palma by the Institute for Solar Physics of Stockholm University in the Spanish Observatorio del Roque de los Muchachos of the Instituto de Astrofsica de Canarias. I want to thank Luc Rouppe van der Voort (Institute of Theoretical Astrophysics, University of Oslo) and J. de la Cruz Rodriguez (University of Uppsala, Sweden) for data reductions with MOMFBD for SST/CRISP. DST/ROSA and DST/IBIS data used were obtained with the facilities of the National Solar Observatory, which is operated by the Association of Universities for Research in Astronomy, Inc. The DOT was operated on the island of La Palma by the Utrecht University (The Netherlands) in the Spanish Observatorio del Roque de los Muchachos of the Instituto de Astrofsica de Canarias. It was funded by the Netherlands Organisation for Scientific Research NWO, The Netherlands Graduate School for Astronomy NOVA, and SOZOU. The DOT efforts were part of the European Solar Magnetism Network. The SVST was operated by the Institute for Solar Physics Stockholm at the Observatorio del Roque de los Muchachos of the Instituto de Astrofísica de Canarias (La Palma, Spain). Finishing with the computational tools used, AstroPy (Astropy Collaboration *et al.*, 2013), Ginga, IPython (Perez and Granger, 2007), Matplotlib (Hunter, 2007), NumPy (Jones *et al.*, 2001), SciPy (Jones *et al.*, 2001), scikit-image (van der Walt *et al.*, 2014), SolarSoft (Freeland and Handy, 1998), SunPy (SunPy Community *et al.*, 2015) and SymPy SymPy Development Team (2014). I want to thank J. Terradas for providing the EMD routines used for data analysis. Wavelet power spectra are calculated using a modified version of the algorithm that was developed by C. Torrence and G. Compo, and is available at http://paos.colorado.edu/research/wavelets/.

Second, the people I have meet and worked with. I would like to thank Steven Christie for inviting me to give a talk at NASA GSFC (even if it did

not go down very well). Alex for his countless help with MHD theory. Chris (and Helen by extension), for helping me throughout my PhD. Without his ability to encourage me and his technique for fine writing and science, I would have been very lost. I want to thank you for out doing me at every turn. I want to also thank Chris's seven papers for getting him two jobs thus keeping him around for Freddie for another two years. Tom, for his ability to ignore me whenever I say hello, I have never been so insulted in my entire life. Freddie, for those gains, the numerous nights out and his bitching talk at NASA GSFC. Stevie, for his inability to eat nice food which has provided many hours of entertainment and his incredible ability to eat an entire loaf of bread in a single sitting. Stuart, for all that Python support he provided me, without which my papers would have been very barren. Sky (and Beth by extension), for letting me annoy them for 4 years (or was it just 3 months?) with my grating personality. It was an honour for me to be a groomsman for your wedding and long may your marriage continue. I want to thank my fountain pen collection for being there through thick and thin (thanks Freddie). The office has been a fantastic environment, through the magic craze, the ball games, the breaking incidents and the antics of Freddie. I do apologize for the loudness that I have caused. But I can say without hesitation, that it has been the best four years so far in my life and I have met some truly amazing human beings. Sorry that I can not include everyone by name but I want to thank everyone else that I have had the pleasure of meeting during my PhD.

I would like to thank my PhD supervisor Robertus Erdélyi. Without him giving me the chance to do this PhD, I would be doing some sort of normal boring job. He believed in me and gave me this opportunity, which I am very grateful for. He has been a fantastic supervisor, encouraging me to push myself and has been patient at the times I have been slow or stupid. Furthermore, the Science and Technology Facilities Council (STFC) funded my PhD and my travels abroad.

Last but not least, my family. I want to thank my mother and sister supporting me through my time at Sheffield. It as always been a comfort to know that I can go back whenever I needed to. I'll be home soon.

Abstract

There have been ubiquitous observations of wave-like motions in the solar atmosphere for decades and the presence of magnetoacoustic waves in magnetic structures in the solar atmosphere is well-documented. By using high-resolution data sets taken from several solar telescopes, the aim was to identify magnetohydrodynamics (MHD) wave modes in the cross-sectional area of these magnetic structures. Two sunspots and four pores were chosen as good examples of MHD wave guides in the lower solar atmosphere. To achieve this aim, the cross-sectional area and total intensity was measured through time, then this signal was analysed with three signal analysis methods, namely, wavelets, empirical mode decomposition (EMD) and the fast Fourier transform (FFT). Many characteristic periods were found within the cross-sectional area and total intensity time series. To identify what MHD wave mode these oscillations are, previously derived linear MHD theory details that each MHD wave mode perturbs the cross-sectional area and total intensity differently. This phase difference is used to separate the possible MHD wave modes. These oscillations were identified as slow sausage MHD waves, as the phase difference between the cross-sectional area and total intensity was in phase which is the signature of slow sausage MHD waves. Furthermore, several properties of these oscillations such as the radial velocity perturbation, magnetic field perturbation and vertical wavenumber were determined using magneto-seismology. The calculated range of the wavenumbers reveals that these oscillations are trapped within these magnetic structures and are standing harmonics. This allowed the calculation of the expansion factor of the wave guides by employing further magneto-seismology theory. Finally was the analysis of Running Penumbral Waves (RPWs). Here, RPWs within a pore are observed for the first time and are interpreted as Upwardly Propagating Waves (UPWs) due to the lack of a penumbra that is required to support RPWs. These UPWs are also observed co-spatially and co-temporally within two emission lines that sample the Transition Region and low corona. The estimated energy of the waves is around 150 W m^{-2}, which is on the lower bounds required to heat the quiet Sun corona.

Table of contents

Chapter 1

Introduction

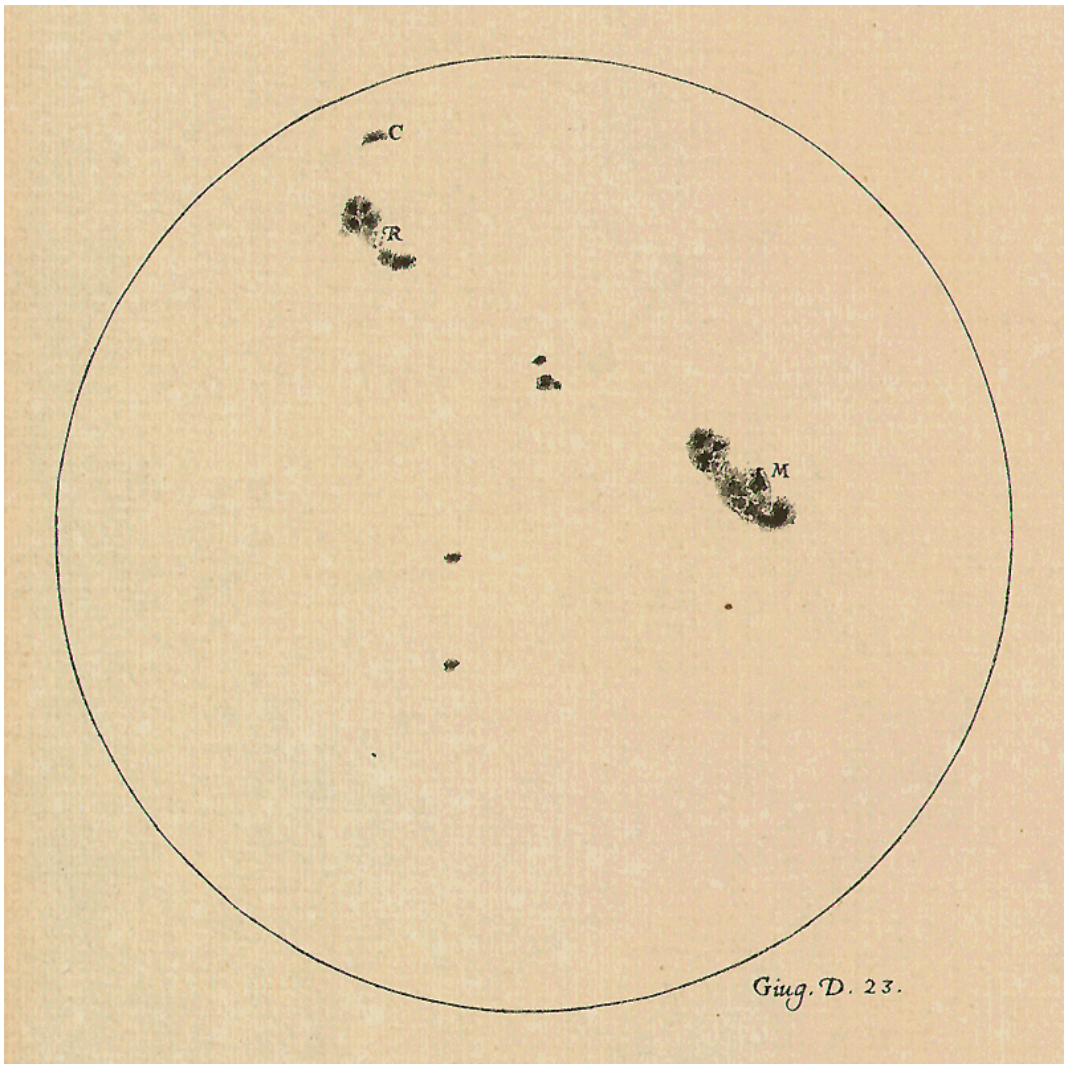

Fig. 1.1 The creation of the telescope forever changed astronomy. Here is a drawing of the solar surface by Galileo during the 17^{th} century. The sunspot structure can be resolved with the inner and outer regions seen clearly. Image credit goes to Project (2015).

1.1 The Sun

Our local star is known as the Sun and is a semi-common and uninteresting main sequence star if you happen to be an astrophysicist. However to the general public and more importantly solar physicists, it forms the backbone of their lives. From simply as mundane as waking up at sunrise, to making a long and (hopefully) successful career in solar physics.

For early humans, it was as a giant bright ball in the sky that appeared to revolve around the Earth and it defied any human understanding at that time. Since the dawn of mankind, the mythology surrounding the Sun has been numerous. From the New World, the Aztec's had a sun god called Tonatiuh. Without constant human sacrifice (mainly their enemies), they believed that the Sun would not move through the sky. From the Far East, the Chinese

originally had 10 suns who took turns moving through the sky. However, these suns were mischievous and decided to all appear at the same time. This made life utterly unbearable on Earth, so an archer bestowed with a unique bow shot down 9 of the suns, leaving the one sun we have today. From the Old World, the Greeks and Romans believed in Apollo who is the son of Zeus and Leto. He was known as the god of music, healing, light, truth and the Sun; a very busy god. With the decline of polytheism and the rise of monotheism, these gods and stories quickly became consigned to history. For a review of solar mythologies, see Olcott (1914).

The Sun had always been observed with the naked eye, sunspots have been visible and recorded by the ancient Chinese, further, many solar calenders were created to order human society. However, no systematic studies of the Sun had ever taken place. It was not until the enlightenment in Europe which marked the start of a massive transformation of European society, in which the telescope was invented (among other things). This is the beginning of modern astronomy.

The telescope was the instrument that allowed humanity's knowledge of our solar system to radically change. It was possible to observe the Sun in much greater detail for the first time. Galileo drew many full disc images of the Sun and Figure 1.1 is one such example. With the telescope, the umbra and penumbra of sunspots was easily differentiated for the first time. Furthermore, pores can be seen in the image. From here, many other discoveries were made such as the sunspot cycle, differential rotation and solar flares. With more time and a solar eclipse, layers of the solar atmosphere were finally observed, such as the chromosphere and the corona. The age of solar physics had finally begun.

The scientific understanding of the Sun has advanced by leaps and bounds, especially during the past sixty years. This is mainly due to the launch of space missions, whether it was SkyLab or the numerous satellites now pointed at the Sun. The removal of the Earth's atmosphere was a decisive step, allowing the observation of spectral lines not possible on Earth and vastly improving the quality of observational data. The solar physics community is hard at work analysing the massive amount of data that is available and expanding humanities knowledge of the Sun. However, there are still crucial challenges to overcome. They have in essence become the holy grails of solar physics: how the corona is heated and what is the dynamo process behind the solar magnetic field.

1.2 The structure of the solar interior

The Sun's internal structure is divided into four sections; the core, the radiative zone, the tachocline and the convective zone. While we cannot see these regions directly, the process of helioseismology, much like seismology on Earth, has allowed humanity to come to grips with these layers and processes that occur within the Sun. Figure 1.2 showcases the multi-layered structure of the Sun. The image starts from the core, through the various interior layers until it reaches the solar atmosphere and the interplanetary medium. This picture of the Sun has been built up over time as our understanding has improved with the use of more observations and complex mathematical models during the past 100 years.

1.2.1 The core

The core is the beating heart of the Sun, the largest fusion reactor this side of Centaurus. The core has more than 60% of the total mass of the Sun and extends roughly to 25% of the total radius of the Sun. It has a density of around 150000 kg m^{-3} and a temperature around 16 MK (Basu *et al.*, 2009). The fusion reactions occur due to the high pressure and temperatures that exist in the core, which are enough to force the hydrogen atoms together. This process, which accounts for the vast majority of the energy generated, creates a range of high energy particles such as photons and neutrinos.

1.2.2 The radiative zone

Due to the intense heat and the large pressure within this region, thermal radiation is the only mechanism able to transfer the heat generated by the core. The process of radiative transfer within the radiative zone happens on very small scales. Photons are emitted and absorbed on very short time-scales. This means that it takes hundreds of thousands years for photons to exit this layer. The radiative zone extends to about 70% of the solar radius (Cox *et al.*, 1991).

1.2.3 The tachocline

The tachocline is the region that separates the radiative zone and the convective zone. It is very thin, its width being only 0.04% of the solar radius. It has been long hypothesised that the solar magnetic field is created within this layer via a dynamo process (Soward *et al.*, 2005; Stix, 2004).

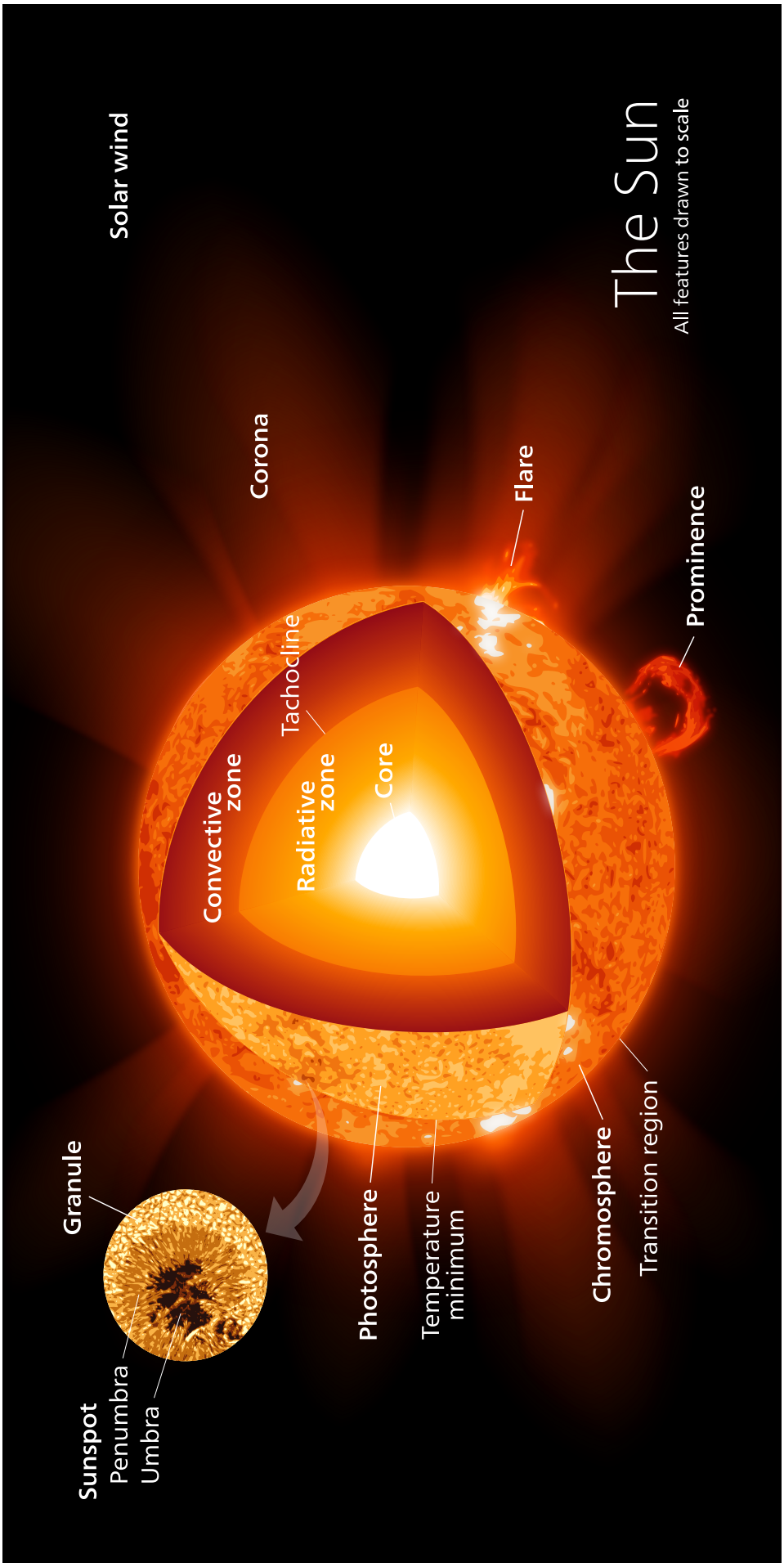

Fig. 1.2 A schematic diagram of the interior and external layers of the Sun. Also shown are several features that occur within the solar atmosphere: sunspots, granulation, flares and prominences. Image credit to Kelvinsong (2015).

1.2.4 The convection zone

From the tachocline, the temperature and pressure has decreased enough to allow the fully ionized molecules to retain some electrons and thus the opaqueness of the plasma increases. This traps part of the radiative energy from below setting up a temperature gradient sufficient enough to allow convection to take place. Thermal columns are created, which carry hot plasma to the surface of the Sun and once it cools, it sinks back to the base of the convection zone. This process is believed to cause gravity waves within the solar interior which have yet to be observed. The visible effect of convection is the solar granulation pattern that can be seen in white light images of the Sun. The pattern consists of cells that have a rough hexagonal shape. At the top of the convection zone, the temperature drops to 5700 K and the density to 0.0002 kg m^{-3} (Page and Hirsch, 2000). Within the convection zone, differential rotation is important. The Sun rotates not as a solid body as the Earth does but as a fluid as the Gas Giants do. The rotation rate decreases from the equator where it is 25 days to around 34 days at the poles (Beck, 2000). Furthermore, the rotation rate varies with depth, until the tachocline is reached, where it rotates as a solid body (Howe *et al.*, 2000).

1.3 The solar atmosphere

The solar atmosphere is quite unlike the Earth's. While they both have multiple layers, the characteristics are wildly different (as you would expect). The top of the convection zone is the start of the first layer of the solar atmosphere. The reason for this is that the optical depth becomes $\lesssim 1$. The optical depth is defined as the fraction of photons that can pass through a layer without being scattered within that layer. For a value of $\lesssim 1$, this means that approximately a third of all photons will pass through this layer unhindered. This layer is called the photosphere. There are three more layers of the solar atmosphere: the chromosphere, the transition region and the corona (see Figure 1.2). Then the solar atmosphere transitions into the solar wind which fills the interplanetary medium.

1.3.1 The photosphere

The photosphere comes from the ancient Greek word "photos" meaning "light". It is the visible surface of the Sun, that can be seen with the naked eye. The photosphere has an approximate thickness of 500 km with a starting temperature of 5700 K which drops as you move away from the surface, getting

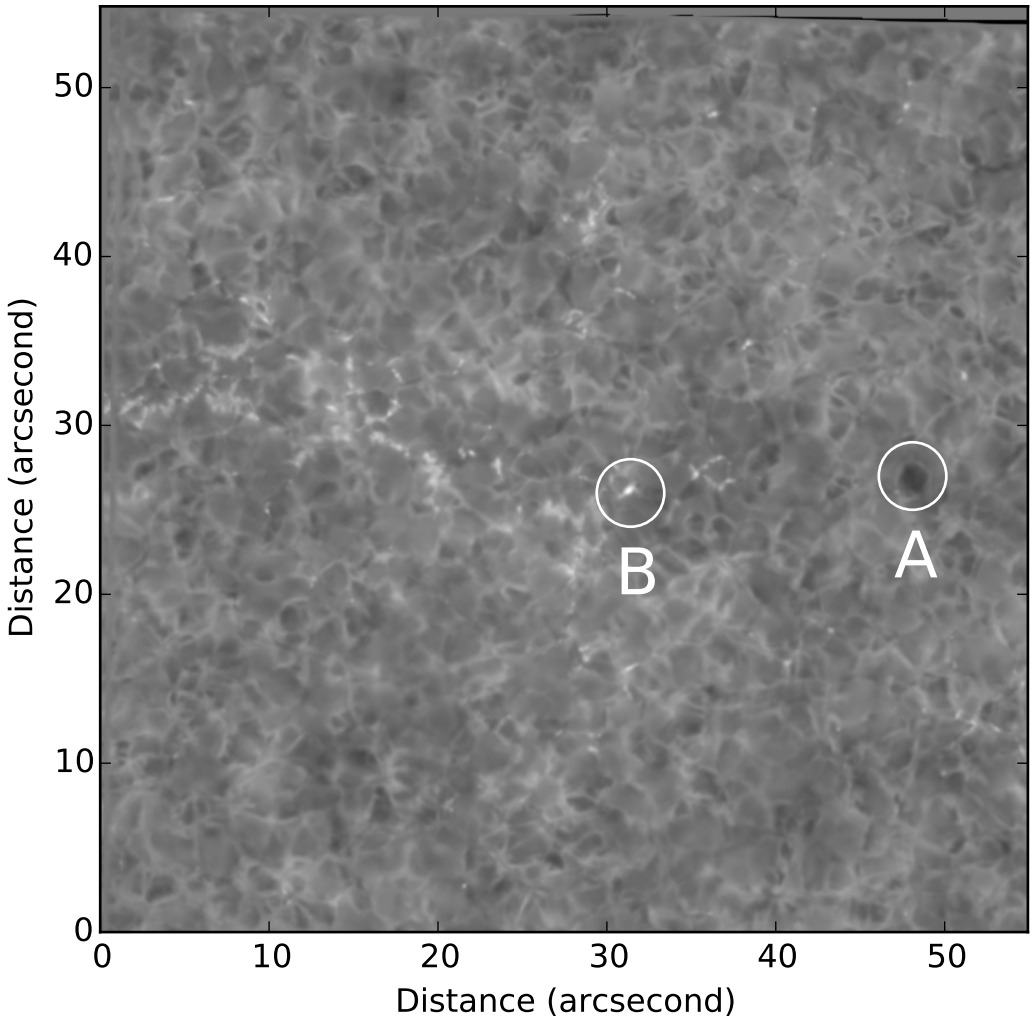

Fig. 1.3 Iron I (630.2 nm) image taken with the Swedish Solar Telescope on the 22^{nd} of July 2012. It shows some of the features that are present in the quiet Sun: a granule cell (A) and a magnetic bright point (B).

to approximately 4500 K. This part is called the temperature minimum and is generally taken to be the top of the photosphere.

The structure of the photosphere is composed of convection cells called granules, which are on average 1 Mm in diameter. Observed flows within these cells show uprising hot plasma in the centre which pushes the cooler plasma to the edges of the cell before flowing downwards. These granules are short-lived, with a lifetime less than 10 minutes, resulting in a repeating pattern at small-scales (Rutten and Severino, 2012). These can be seen in Figure 1.3, within circle A. On larger scales, super-granule structures have been observed with a 30 Mm diameter which can last for a day or longer (Rieutord and Rincon, 2010).

The convective nature of the Sun has allowed us to infer the interior structure. The reason for this is that turbulence within the convection zone creates an entire spectrum of acoustic waves, named p-modes, where p stands for pressure.

p-modes penetrate into the solar interior and at certain frequencies, the waves become standing. These can be measured on the photosphere, using line-of-sight (LOS) Doppler images. The mathematics used as a basis for this research is called spherical harmonics and allows p-modes that are observed to be understood. The mode's overall properties are affected by the physical conditions where the maximum amplitude for that mode occurs. This allows an image to be built up at every depth within the solar interior. For reviews on this topic, see Deubner and Gough (1984) and Christensen-Dalsgaard (2002).

The dynamics of the photosphere is governed by two processes, convection as discussed above, and the solar magnetic field. Thus understanding how the magnetic field is structured within the photosphere is important. The most common method employed in solar physics to measure the magnetic field, is to exploit the Zeeman effect (Phillips, 1995). When atoms are subjected to a magnetic field, their spectral lines split as a function of field strength and polarization. Unfortunately, this effect can only really be used in the photosphere, as only the photospheric magnetic field is strong enough to cause the Zeeman effect. However, many solar physicists have attempted measurements in various weak field areas (Kontar *et al.*, 2008; Lin *et al.*, 2004; Metcalf *et al.*, 1995). These images are called solar magnetograms and they have revealed the basic magnetic field structure in the photosphere. The magnetic field is very weak ($\leq$ 40 Gauss) on average and is very sparse (Domínguez Cerdeña *et al.*, 2006; Viticchié *et al.*, 2011). This is referred to as the quiet Sun and is shown in Figure 1.3. The dominating feature within this image is the granulation cells, which are the structures formed by convection, as well as several small magnetic features which are detailed further on.

Figure 1.4 demonstrates the semi-empirical model of the quiet Sun atmosphere (Vernazza *et al.*, 1981). Only shown are the density and temperature which is blue and red, respectively. The full model has extra parameters such as number density, total pressure and optical depth all as a function of height. This model is termed the "VALIIIc" model and is used as the base atmosphere for many MHD simulations (Fedun *et al.*, 2011a,b; Gent *et al.*, 2013; Mumford *et al.*, 2015; Scullion *et al.*, 2011; Shelyag *et al.*, 2011; Vigeesh *et al.*, 2012; Wedemeyer-Böhm *et al.*, 2012).

Within the photosphere are small regions of concentrated magnetic field, named Magnetic Bright Points (MBPs, Feng *et al.* 2013. They are small-scale bright dots, as can be seen in Figure 1.3, in the circle labelled B. They are formed in the gaps between granule cells since the plasma flow drags the magnetic flux to high concentrations (>1 kG). The most likely reason for the increased brightness is that the flux tube has been evacuated of plasma (Sánchez Almeida *et al.*, 2004). As such, observations of MBPs allow a glimpse into the top of

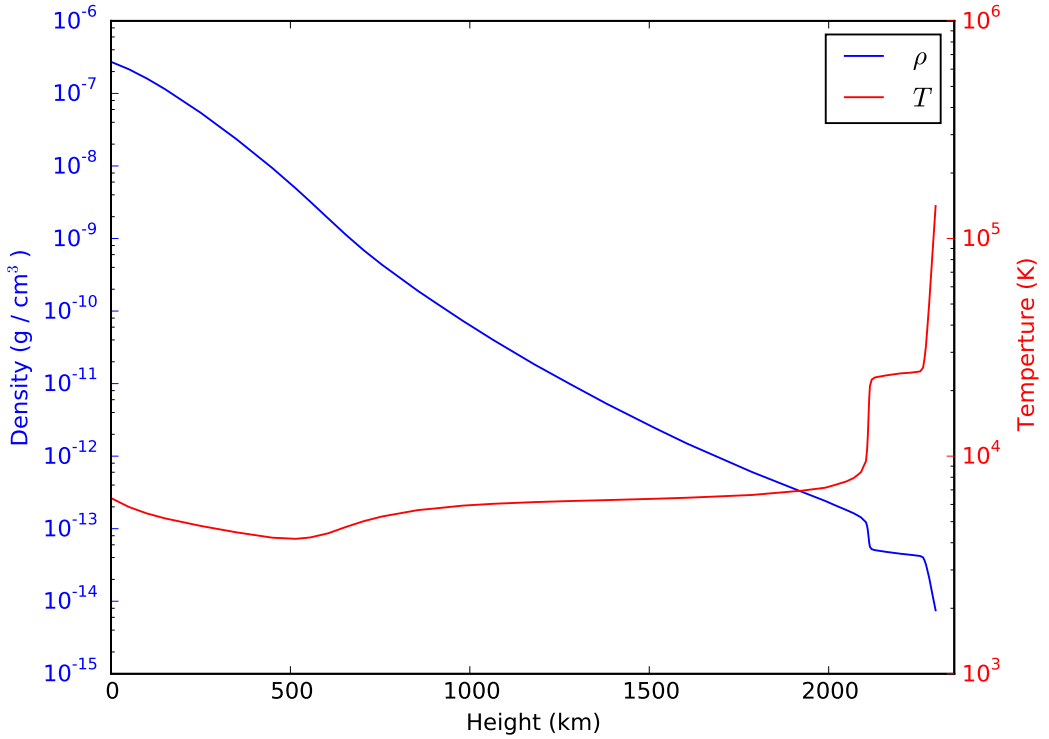

Fig. 1.4 The VALIIIc (Vernazza *et al.*, 1981) model of the quiet Sun, shown are the density in blue and temperature in red. The temperature minimum region and the transition region can be seen with these two parameters.

the convection zone, which has a higher temperature than the photosphere and is brighter. One important factor about MBPs was the observation of Alfvén waves (Jess *et al.*, 2009; Taroyan and Erdélyi, 2009). This was able to supply enough energy to the corona to overcome the "Coronal Heating problem" (detailed in Section 1.3.4).

1.3.1.1 Active regions

Active Regions (ARs) sometimes referred to as sunspot groups, are areas of intense magnetic field concentrations located on the Sun's surface. They are catalogued by the National Oceanic and Atmospheric Administration (NOAA) who assign each AR an identification number. ARs vary in scale, lifetime and what magnetic structures are present and two of most prevalent features within ARs are sunspots and pores. Furthermore, most ARs will contain magnetic features found in the quiet Sun and events that are believed to be a consequence of magnetic reconnection. This events are more likely to occur within ARs due to the more complex magnetic field geometry. Figure 1.5 displays an AR and it consists of 3 sunspots, taken as the AR is about to disappear off-limb. Circle A encloses one of the sunspots, but by use of a different wavelength filter we can observe an EB (B) and a jet event (C). The last two events are associated

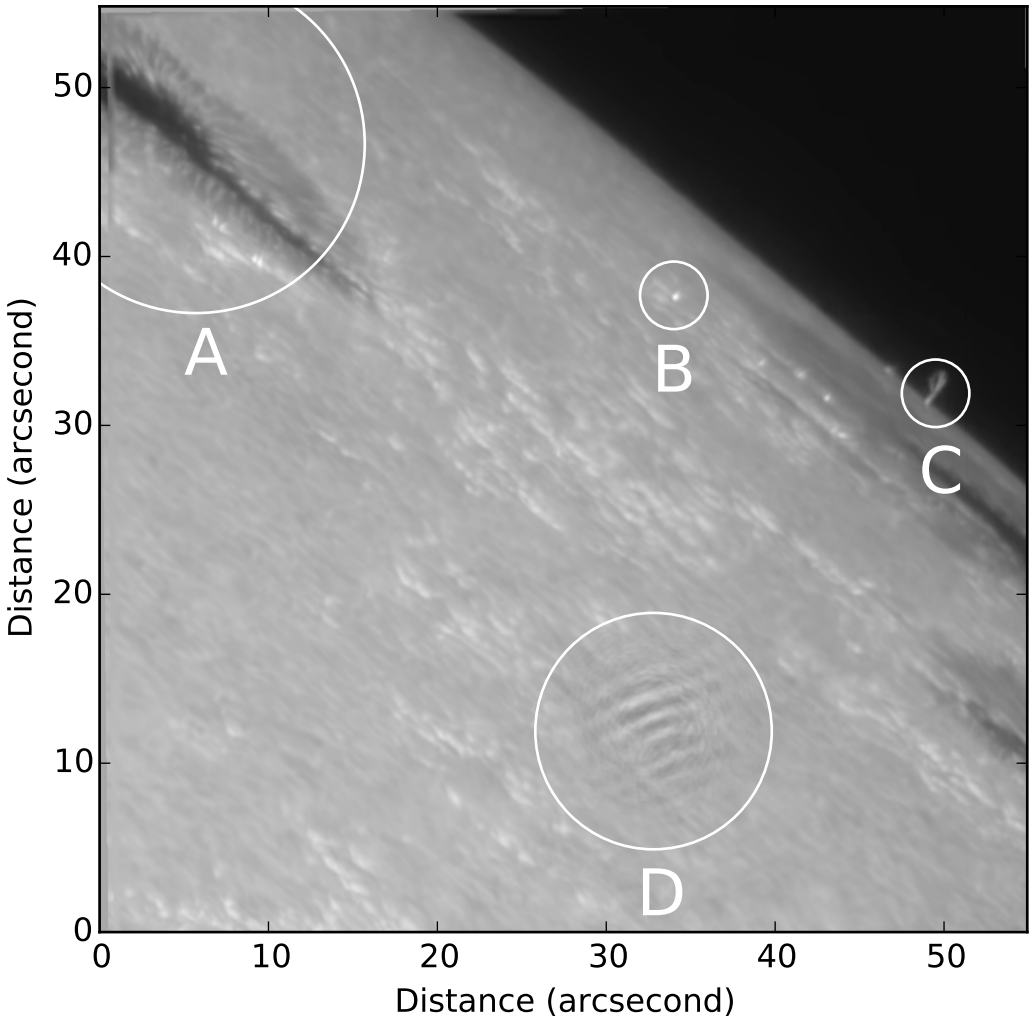

Fig. 1.5 An image of an active region (AR, NOAA 11504) taken with the Swedish Solar Telescope (SST) using the Crisp Imaging SpectroPolarimeter (CRISP) on the 21^{st} June. The Hα filter was selected but into the far wings, such that strong photospheric features can be observed. It shows some of the features that are present in Active Regions: sunspot (A), Ellerman Bomb (B) and a jet (C). Finally, a seeing effects caused by the optical setup (D).

with magnetic reconnection (Nelson and Doyle, 2013; Nelson *et al.*, 2013a,b, 2015; Reid *et al.*, 2015).

ARs will form within specific latitude from the equator, typically ±30°. They arise from a large flux bundle that is formed deep in the convective zone that rises as a Ω-shaped loop that breaks through the photosphere (Meyer *et al.*, 1974; Solanki, 2003; Toriumi *et al.*, 2014). Magnetic buoyancy is the reason this bundle rises through the convective zone. Figure 1.6 shows a schematic diagram of how magnetic flux is transported from the convective zone to the photosphere in order to form ARs. The process requires two processes: the solar dynamo to create the magnetic field and differential rotation to create the flux bundle. Typically, it can take up to a few days for an AR to fully form and

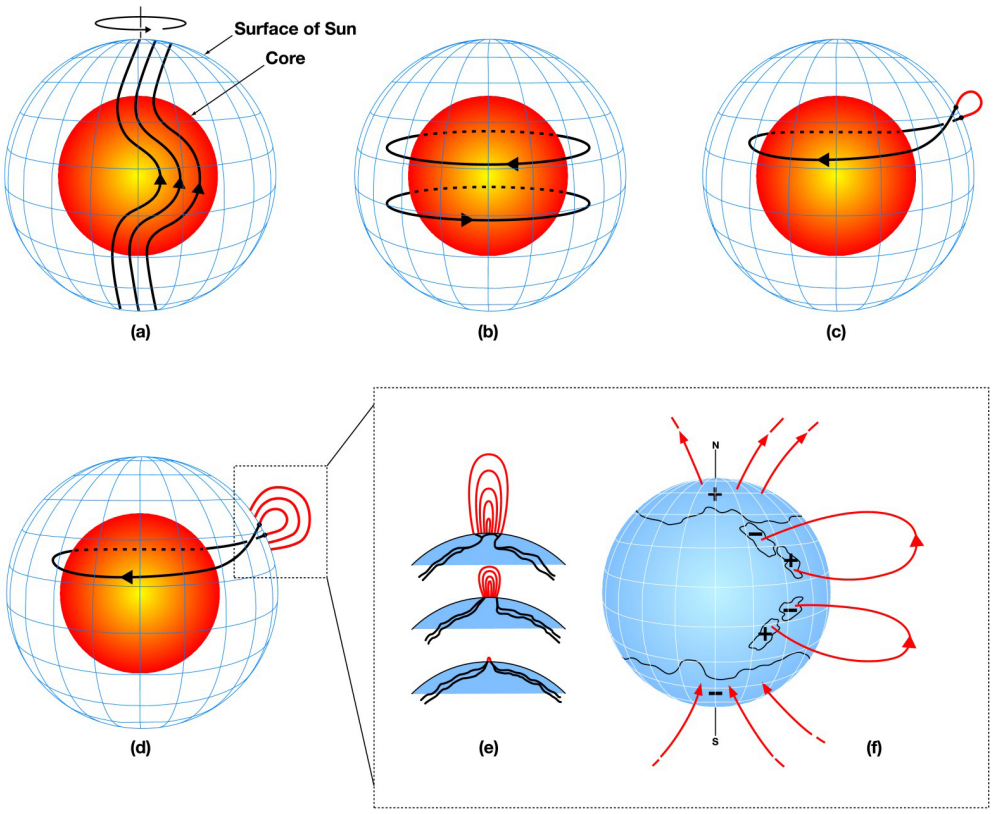

Fig. 1.6 Schematic of magnetic flux emergence. The red sphere represents the Sun's radiative zone and the blue mesh the photosphere. The solar dynamo is located between these two layers (a) The Sun's differential rotation shears the magnetic field. (b) Toroidal magnetic field is produced due to differential rotation. (c) Buoyant magnetic loops rise to the surface when the magnetic field is strong enough and they twist as they rise due to differential rotation. Sunspots are formed from these loops. (d,e) Additional magnetic flux emerges. (f) Magnetic flux spreads in latitude and longitude from decaying sunspots. Reproduced from Dikpati and Gilman (2007) and is available online from http://www.arrl.org/w1aw-bulletins-archive/ARLP018/2013.

it is common that a cluster of sunspots in an AR are surrounded by regions of enhanced brightness in the photosphere. While in the corona, EUV and X-ray loops can be seen to have footpoints that are anchored in ARs (Priest, 2014). Sunspots will keep forming as long as magnetic flux emerges but most sunspots will decay before a single rotation. The leading sunspot in an AR is called the p-spot or leader and the last sunspot in the AR is called the f-spot or follower. It is common that the leader sunspot is long-lived while the follower sunspot will short-lived, be irregular in shape and an opposite polarity magnetic field to the leader sunspot. Sunspots move faster than the surrounding local plasma and this implies that they are anchored below the surface where the rotation rate is faster. ARs tend to drift apart at a rate of 0.1° per day due to the leader sunspot being at a lower latitude.

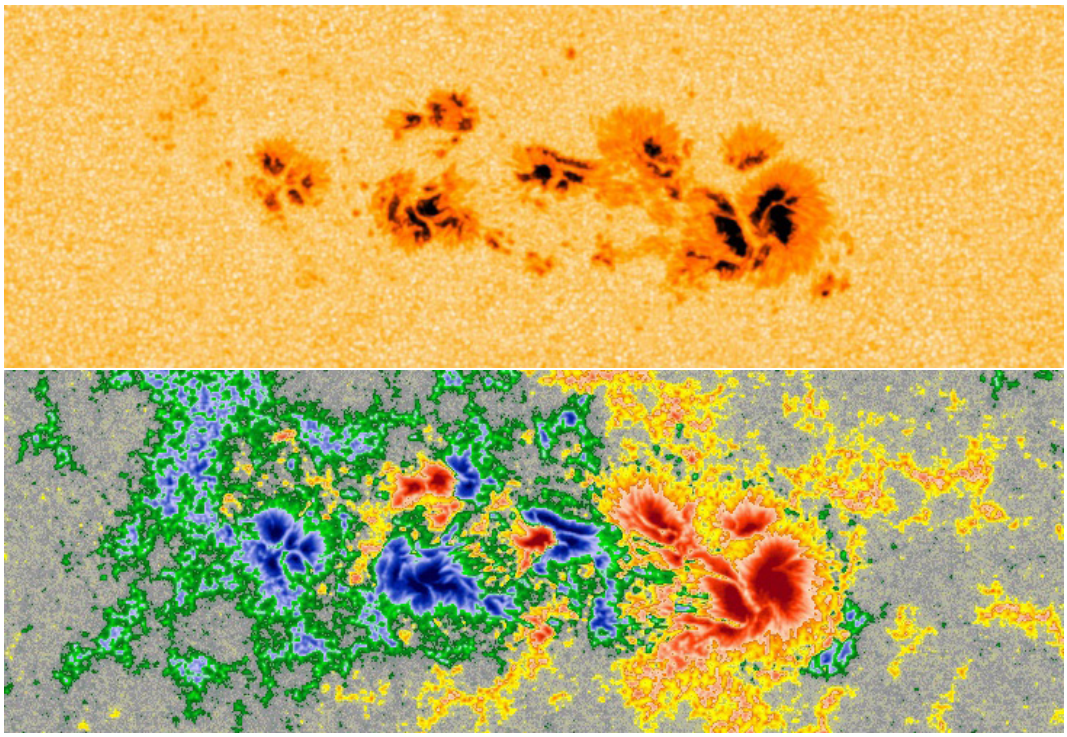

Fig. 1.7 An example of a complex AR as seen by National Aeronautics and Space Administration's (NASA) Solar Dynamics Observatory (SDO) satellite's Helioseismic and Magnetic Imager (HMI) instrument. The top image is the AR as seen in white light. The bottom image displays the line-of-sight (LOS) magnetic field of this AR, where blue indicates positive polarity and red indicates negative polarity. Taken from http://www.spaceweatherlive.com/en/help/the-magnetic-classification-of-sunspots.

ARs are classified by the magnetic field polarity of the entire region. A unipolar (α-type) AR make up 46% of all ARs while a bipolar (β-type) AR makes up 53% and the remaining ARs have a complex (γ-type) magnetic polarity (Priest, 2014). Figure 1.7 show a complex AR that was observed with the National Aeronautics and Space Administration's (NASA) Solar Dynamics Observatory (SDO) satellite's Helioseismic and Magnetic Imager (HMI) instrument. The top image is a white light view of the AR while the bottom image is a LOS magnetogram where blue is positive polarity and red is negative polarity. ARs with complex magnetic field geometries are more likely to be the source of a large solar flare. Furthermore, δ-type sunspots have an umbra that has opposite polarity inside the same penumbra.

1.3.1.2 Sunspots

The first historical account of sunspots starts in a chronicle by John of Worcester in 1128. However, as observing the Sun directly is difficult without the proper equipment, it was not until the invention of the telescope that sunspots were studied. Both Galileo and Christoph Scheiner were the first people to observe

sunspots with a telescope (see Figure 1.1). It was quickly demonstrated that sunspots had two regions (umbra and penumbra) and that they appear near the solar equator. Alexander Wilson noticed that the penumbra that is farthest from the limb is narrower and he deduced that sunspots are on the surface of a moving sphere. Furthermore, he discovered that a sunspot is a saucer-like depression (500-700 km) in the visible surface and this was named the Wilson effect. The depression is due to the colder less-dense umbra being more optically transparent. This means that the light from the umbra comes from a deeper level than the photosphere (Priest, 2014).

Sunspots are darker regions on the solar surface and the reason is due to the partial inhibition by the sunspot's magnetic field of convection, which is the dominant process that transports energy from the convection zone up to the photosphere. With a telescope, a sunspot can be divided into two regions. The first region is the called the umbra which has an almost vertical magnetic field. However, this region is surrounded by a brighter region with a weaker more horizontal inclined magnetic field. This is called the penumbra and is highly filamentary with a pattern of bright and dark radial filaments. The umbral radius can make up to 50% of the total sunspot radius.

The brightness of a sunspot is dependant on the observer's wavelength of choice. However, integrated over all wavelengths the total brightness is around 30% of the photospheric brightness. The temperature of the umbra is around 1000-2000 K less than the photosphere. In order to maintain this brightness implies that a substantial convective flux is still being transported despite the sunspot's magnetic field. The penumbra's brightness is around 75-85% of the photosphere and is only cooler by 400 K. Sunspots come in a range of shapes and sizes, with typical diameters that range from 3.5-60 Mm and it was discovered that the lifetime of a sunspot is proportional to its area.

The umbral magnetic field is almost vertically inclined and its strength is proportional while its brightness is inversely proportional with respect to the umbral size. The average umbral magnetic field strength is around 2.8 kG but it can range from 1.5-6 kG (Livingston *et al.*, 2006). As the distance from the centre increases, the magnetic field strength decreases gradually and an average magnetic field over the entire sunspot is around 1.2-1.7 kG. The inclination of the penumbral magnetic field increases with radius to a average value of 70-80° and the magnetic field strength is around 700-900 G.

The umbra of a sunspot is far from uniform. High-resolution images from telescopes have revealed a range of small-scale features in sunspot umbras. For example, umbral dots are small bright features that are found in all sunspots and pores (Danielson, 1964; Thiessen, 1950). They have diameters of 100-450 km and they are associated with upflows of $\sim$ 1 km s^{-1} and with lifetimes

of 0.2-2 hours (Sobotka *et al.*, 1997a,b). While they only cover 3-10% of the umbra, they account for 10-20% of the umbral brightness and are around 1000 K hotter than the umbra. Light-bridges are narrow features with a brightness that is similar to the penumbra which cross over the umbra of a sunspot or pore. Essentially, a light-bridge is a crevice separating two different umbral regions of a sunspot or pore and within this crevice is a a ridge that is an enhancement of density (Hirzberger *et al.*, 2002). Light-bridges are most commonly observed before the breakup of a sunspot and they can continue to grow in size during the decay of a sunspot.

The penumbra of a sunspot is intricate as it is high filamentary in nature. To start, the filaments that make up the penumbra have lengths of 3.5-7 Mm and have lifetimes of 0.5-6 hours. There are appear to be two distinct types of penumbral filaments: bright filaments and dark filaments. Bright filaments have a brightness that is around 95% of photosphere while dark filaments have a brightness around 60% of the photosphere. The width of a filament is around 150 km and they seem to posses unresolved features which are below the currently available spatial resolution (Scharmer *et al.*, 2002, 2011). However, it should be noted that within the literature, it has been argued that bright and dark filaments are not separate categories (Tiwari *et al.*, 2013).

While the geometry of the umbral magnetic field is almost vertically inclined, the penumbral magnetic field has been described as an interlocking comb (Thomas *et al.*, 2002). In general, a dark filament's magnetic field is more horizontally inclined than bright filaments (Langhans *et al.*, 2005). Some dark filaments make up a shallow canopy that is around 300 km high and extend not too far from the sunspot. As bright filaments are more vertically inclined, they form loops extending far beyond the sunspot. It have been observed that this complex geometry evolves with time and can occasionally reconnect with neighbouring magnetic field which creates fine-scale penumbral jets (Katsukawa *et al.*, 2007).

The Evershed flow is the most known flow that is associated with sunspots. It is a radial outflow observed in sunspot penumbras that is parallel to the local magnetic field (Bellot Rubio *et al.*, 2003). The average velocity is around 2 km s^{-1}, however, it has been measured as high as 6 km s^{-1}. The direction of the flow horizontal, but there is an upwards inclination and a downwards inclination in the inner and outer penumbra (Tritschler *et al.*, 2004). When observed in wavelengths that are higher than the photosphere, the flow slows and reverses direction in the chromosphere (Montesinos and Thomas, 1997). This is called the reserve Evershed effect and it extends over a large region surrounding a sunspot.

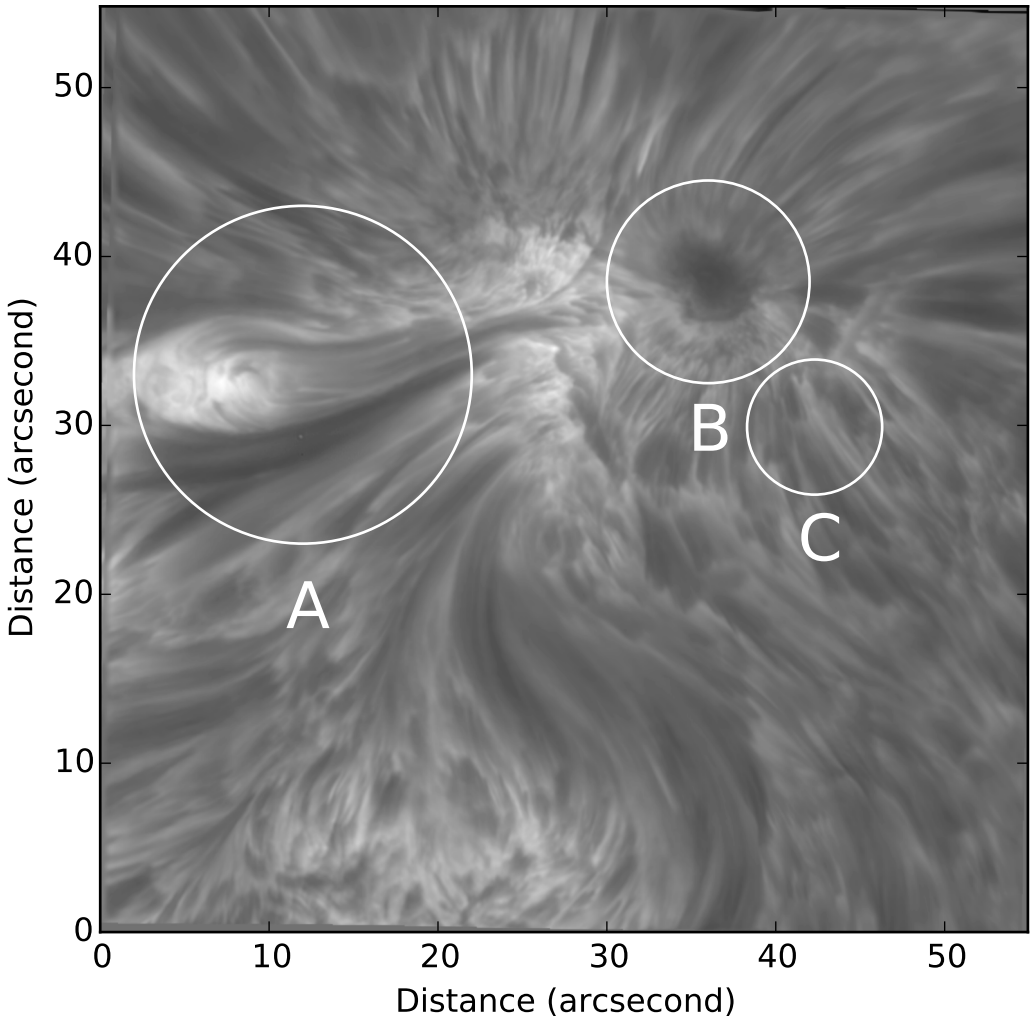

Fig. 1.8 A Hα line core image of Active Region NOAA 11510 observed on the 22^{nd} June 2012. Here, this AR has a large pore that displays Running Penumbral waves (the focus of Chapter 5). Highlighted here are fibrils (A), the pore (B) and dynamic fibrils (C). The complex nature of the chromosphere can be seen in detail.

Pores can be considered as smaller scale sunspots without a penumbra and thus are sometimes referred to as "naked umbra" sunspots. They are intermediate flux concentrations between small intense flux tubes and sunspots. Pores have diameters that range from 0.7-7 Mm and the largest pores are bigger than the smallest sunspots. When compared to sunspots, they have a brightness that is around 50% of the photosphere and a magnetic field strength that starts 1.8-2.3 kG drops to 1 kG at the edge (Priest, 2014). Due to their small size, pores have not been heavily studied as it took the newer generation of solar telescope before they could be resolved clearly. One example of a pore can be seen in Figure 1.8, labelled B, which is analysed in Chapter 5. This image is in the Hα core which samples the chromosphere which is discussed in Section 1.3.2.

Sunspot formation is a hotly debated topic (as many things are in solar physics). The current hypothesis about how they form is as follows. The magnetic field of the Sun, created by the solar dynamo, is strongly polarised and with differential rotation, these magnetic fields lines become bunched together, increasing the local magnetic field strength. This effect creates a magnetic buoyancy force which slowly makes this newly created flux region rise towards the surface until it penetrates into the photosphere. This process is summarised in Figure 1.6. The flux region that is buoyed upwards tend to be a Ω-shaped loop and has a field strength >1000 G (Stix, 2004; Toriumi *et al.*, 2014). The strong magnetic field inhibits local convection which means that the plasma in this flux region cools. The strength of the magnetic field will grow until the external gas pressure is balanced by the internal magnetic pressure (Priest, 2014). Sunspots are essentially formed by the accumulation of magnetic flux which collects at a boundary or a junction of several granule cells or by the merging of small pores (Meyer *et al.*, 1974). Furthermore, as the sunspot forms, an annular convection cell referred to as a moat is found around this sunspot and it can be considered as a super-granule cell with a sunspot in the middle. Pores generally appear if there is a region with a downflow of around 0.5 km s^{-1} and there are signs of convective collapse. These pores last for up to a day but if the pore keeps growing it can form into a small sunspot as it will have enough magnetic flux to form a penumbra (Schlichenmaier *et al.*, 2010). Smaller sunspots will fragment within a few days and the formation of a light-bridge signifies this. Light-bridges are known to also form along the boundaries between pores that have coalesced to form a sunspot. Long-lived sunspots decay very gradually as magnetic flux is stripped away by the outward flows that surround a sunspot (Kubo *et al.*, 2008; Martínez Pillet, 2002).

It should be noted however, that a complete understanding of how sunspots form has not yet been achieved and the mechanism is likely to be more complex than the one described above. A more thorough review of the formation, evolution and unanswered questions relating to sunspots can be found in these reviews, Rempel and Schlichenmaier (2011); Solanki (2003); Thomas and Weiss (2008).

While sunspots have been under near constant observation for several centuries. It was not until the mid 20^{th} century, that oscillations were observed within sunspots themselves (Bogdan and Judge, 2006). There are three main sunspot oscillations: 3-minute (5 mHz) and 5-minute (3 mHz) oscillations and running penumbral waves (RPWs). However, it should not be assumed that the period of these oscillations form one finite peak in a power spectrum; generally, the immediate spectral area around these periods has several peaks clustered tightly together. The first two are observed with a LOS analysis, i.e., frequency

filtering using the Fast Fourier Transform (FFT, which is covered in Section 2.3.1). However, there is some evidence to suggest the existence of longer period oscillations (Chorley *et al.*, 2010, 2011; Staude, 1999). The source of the 5-minute oscillation is thought to be a result of forcing by the 5-minute p-mode global solar oscillation (Christopoulou *et al.*, 2003; Georgakilas *et al.*, 2002). The 5-minute oscillation is typically seen in lines which form low in the cool umbral photosphere and are moderately suppressed not only in the penumbra, but also in the chromospheric atmosphere above the umbra (Bogdan and Judge, 2006). The 3-minute oscillation is seen in elements that form higher up, in the low chromosphere, and is also moderately suppressed in the penumbra (Bogdan and Judge, 2006). It has become clear recently that the 3-minute oscillation is they are low-β slow magneto-acoustic waves guided along the ambient magnetic field (Christopoulou *et al.*, 2000; Georgakilas *et al.*, 2002; Kobanov *et al.*, 2006). The 3-minute oscillation has been linked to sudden brightening called umbral flashes (Beckers and Tallant, 1969). These flashes are seen in chromospheric lines and have a rapid increase and decrease in brightness. They repeat with a period of 140-190 seconds, can have diameters up to 2 Mm and move rapidly towards the penumbra at speeds of 40 km s^{-1} (Rouppe van der Voort *et al.*, 2003) A review of sunspot oscillations can be found in Bogdan and Judge (2006) and a review of solar oscillations can be found in Kosovichev (2009).

The solar cycle is on average a 11-year variation that the Sun undergoes. This cycle manifests itself as a variation in the number of sunspots, the amount of solar irradiance and the levels of other solar activity (Burroughs, 2007). The polarity of the solar magnetic field inverts as well. So some suggest that the full solar cycle is 22 years, but the features that occur on the Sun seem to be independent of the current magnetic field polarity. Each cycle has a solar maximum and a solar minimum. A solar maximum and a solar minimum refer to periods of maximum and minimum sunspot counts, respectively and cycles span from one minimum to the next. As the names suggest, there is a large amount of ARs and magnetic activity at a solar maximum, while this is reduced in a solar minimum. Each solar cycle can be seen in the amount of sunspots which are visible (i.e., the amount of ARs that form). This has been counted since the 17^{th} century and it is called the sunspot number catalogue (Eddy, 1976). Figure 1.9 displays this catalogue with the raw count as the blue line and a running average in red. The main conclusion is that each cycle has a different duration and will produce a differing amount of sunspots. Since each solar cycle will differ in strength, the variation in the number of "extreme" events, such as flares and coronal mass ejections (CMEs) is observed. The reason is that these events require regions of strong magnetic field concentrations, i.e., ARs. So as the number of ARs decline, the possible regions that can cause

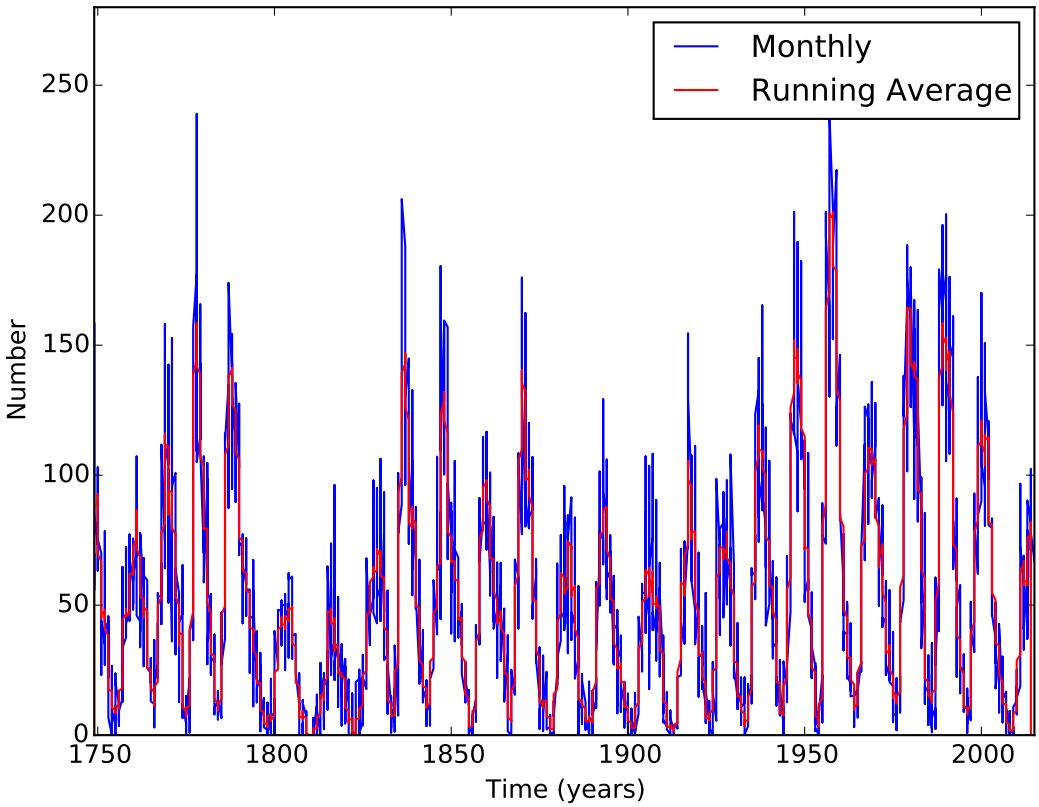

Fig. 1.9 The sunspot number record as it currently stands since continuous observations of the Sun began. The blue line is the monthly count and the red line is the running average. The eleven year solar cycle is visible within both datasets.

flares or CMEs also decreases. Finally, the structure of the solar atmosphere will vary during each solar cycle as the magnetic field has an important effect on how the solar atmosphere is structured (Wedemeyer-Böhm *et al.*, 2009).

The solar cycle can directly impact the Earth's climate, as shown by the Maunder Minimum, which was an abnormally low amount of sunspots during the late seventeenth century and was the suspected cause of the Little Ice Age (Burroughs, 2007; Friis-Christensen and Lassen, 1991). Earth over the past eight years was seeing another abnormal solar minimum, though it was not on the scale of the Maunder Minimum. During that time, there were very cold winters experienced by the northern hemisphere and it has been suggested that the solar cycle may influence the relationship between the atmospheric oscillations which affect the temperature of the northern hemisphere (de La Torre *et al.*, 2007; Gimeno *et al.*, 2003; Lockwood *et al.*, 2010).

1.3.2 The chromosphere

The next layer is visible from Earth when there is a total eclipse of the Sun. It is seen as an intense red region which was given the name, the chromosphere,

from the Greek word "chroma", meaning colour. It is roughly 2 Mm thick and is a highly complex layer. The temperature of the chromosphere increases with height and reaches around 20,000 K at the boundary where it meets the next layer, the transition region. The chromosphere is host to many small-scale structures that have been discovered due to the increasing optical resolution of solar telescopes over the past few decades. To observe the chromosphere from Earth, it is common to use either a Hα filter, or a Ca II filter. These are discussed in more detail later on in Section 2.2.1.

There are various names for these small-scale structures: spicules, fibrils, mottles and straws. The prevailing hypothesis is that there are two spicule types. Type I spicules are mainly seen in ARs but are scattered loosely elsewhere in the solar atmosphere. They can reach speeds up to 50 km s^{-1} and heights of 5 Mm before falling back down, with typical lifetimes of 3 to 10 minutes, diameters of 120 to 700 km and temperatures of 10 to 15 kK. On disc, they are called dynamic fibrils and called mottles in the quiet Sun. Fibrils tend to be more elongated than mottles which are shorter.

Type II spicules are located more often in the quiet Sun. They are faster (up to 150 km s^{-1}), longer (up to 10 Mm) and have a significantly reduced lifespan (up to 150 s) when compared to Type I spicules. On disc, they are referred to as straws or more commonly Rapid Blue-shift Events (RBEs, Zaqarashvili and Erdélyi 2009). Finally there is another fibril type that are long and mostly horizontal and longer-lived than dynamic fibrils. Some of these features are highlighted in Figure 1.8. The circle A, has a good example of fibrils, long and fairly static, while circle C, shows dynamic fibrils which continually moved and swayed during this observation.

These structures have been under investigation as a potential source of energy transport in the solar chromosphere. Morton *et al.* (2012) using ground-based observations discovered incompressible transversal motions for fibrils. These matched the ones observed for limb spicules which were interpreted as Alfvén waves (De Pontieu *et al.*, 2007). Furthermore, fast compressive MHD waves were also observed. The estimation of the energy these waves carry is quite large but explaining how they dissipate this energy is unknown at this time. A review of oscillations in spicules can be found by Zaqarashvili and Erdélyi (2009).

Running Penumbral Waves (RPWs), are a phenomenon discovered by Zirin and Stein (1972) and Giovanelli (1972). Observed in Hα in sunspot penumbrae, they are seen as a wave train of enhanced brightness that moves from the umbra to the penumbra. They tend to be concentric and cover a large azimuthal angle. On average, they have a speed of 15 to 20 km s^{-1} before slowing to 5 to 7 km s^{-1} at the end of the penumbra. They have a typical period of 200 to 300

seconds. Common interpretation is that much like the 3-minute oscillations, they are slow magneto-acoustic wave propagating upwards along the inclined magnetic field and the radial outwards movement is actually a visual pattern (Bogdan and Judge, 2006; Christopoulou *et al.*, 2000; Kobanov *et al.*, 2006). This is discussed further in Chapter 5.

Finally, we discuss the existence of a Moreton wave (Moreton, 1960). These are seen in Hα wings as a dark and then a bright front. They travel away from flaring regions and are generally confined to a specific arc. They are more of a pulse than a wave and can travel at speeds up to 2000 km s^{-1}.

1.3.3 The transition region

Above the chromosphere, is a thin ($\approx$ 100 km) layer where the temperature rises rapidly from 20,000 K to 1,000,000 K. This is called the transition region (TR). The density and temperature in this region decrease and increase exponential and Figure 1.3 demonstrates this. This means that TR is very non-uniform and Tian *et al.* (2009) suggests that the height varies depending on what magnetic features are below the TR. It cannot be observed from the surface of Earth, but can be studied by space-borne instruments sensitive to ultraviolet (UV) and extreme ultraviolet (EUV) light.

Spicules, as discussed in Section 1.3.2, rise to large heights and it had been hypothesized that the TR would be a boundary. The spicule should hit the TR and create some form of a disturbance. These were found using the Extreme-Ultraviolet Imaging Spectrometer (EIS) instrument on-board the Japan Aerospace Exploration Agency's (JAXA) satellite Hinode and named Transition Region Quakes (TRQs). Coupled with MHD simulations, the disturbance was identified as a fast magneto-acoustic-gravity wave (Scullion *et al.*, 2011). These events further cement the link between the lower solar atmosphere and the higher regions.

1.3.4 The corona

The next layer is the outer atmosphere of the Sun is called the corona. It is most easily seen during a total solar eclipse, but also observable using a coronagraph (Aschwanden, 2004). The sheer scale of the corona is impressive. It extends many solar radii away from the solar surface and it is continuously expanding into the solar system which known as the solar wind. This entire region is called the heliosphere and this extends far past the orbit of Pluto.

The average temperature of the corona is about 1-2 MK, however, it can reach temperatures as high as 8-10 MK (Aschwanden, 2004). The physical processes that account for the high temperature of the corona is still unknown,

but two main hypotheses are in contention. The first idea is called magnetic reconnection. This process is where magnetic field changes its topology and the magnetic energy stored within the field is converted to kinetic and thermal energy. Thus the plasma that is present in these reconnection regions will become heated. The second idea is MHD waves. The Sun creates a large amount of energy and the idea is that MHD waves can channel this energy from the convection zone through the various layers of the solar atmosphere and then into the solar corona. It requires that theses MHD waves are able to dissipate their energy into the plasma in order to heat this plasma. However, this has yet to be observed.

In all likelihood, a combination of these two main ideas will be the mechanism behind coronal heating. This topic has been heavily researched for many decades and you can see reviews by Erdélyi (2004) and Parnell and De Moortel (2012). The most recent development has shifted the question, from "how do you heat the corona?" to "how do you heat the chromosphere?" (Aschwanden *et al.*, 2007).

The corona is host to many structures: X-ray bright points, plumes, prominences, streamers, coronal loops and coronal holes. When using a wavelength filter that samples higher temperature plasma ($\geq$ 1 MK), loop structures can be seen that rise several mega-meters in height and these are called coronal loops. Reale (2010) offers a detailed review of coronal loops.

ARs will also be the areas where flares or coronal mass ejections will originate from, since they contain large amounts of stored magnetic energy. These are the most spectacular events produced by the Sun. The amount of mass and energetic particles ejected can be considered scary, as these events can have a direct impact on the Earth. From simply creating the aurora near the poles or in certain situations the disruption of radio transmissions, damage to satellites and electrical transmission lines. So it is important to understand the formation mechanism of these events so they can be predicted and take measures to limit their damage. This is the realm of space weather research.

For a long time, it was hypothesised that MHD waves could not propagate into the corona due to the acoustic cut-off frequency. The launch of the Transition Region And Coronal Explorer (TRACE) satellite changed this (Handy *et al.*, 1999; Strong *et al.*, 1994). Numerous MHD oscillations were observed: damped transversal oscillations (Goossens *et al.*, 2002; Ofman and Aschwanden, 2002), standing fast kink waves (Aschwanden *et al.*, 1999; Nakariakov *et al.*, 1999; Schrijver *et al.*, 1999), standing acoustic modes (Wang *et al.*, 2003), fast sausage (Katsiyannis *et al.*, 2003; Williams *et al.*, 2001, 2002), fast kink waves (Verwichte *et al.*, 2005), propagating acoustic modes (De Moortel *et al.*, 2000; Marsh *et al.*, 2002; Ofman *et al.*, 1997) and torsional modes (Erdélyi

et al., 1998). This led to a large focus on coronal seismology which allows the estimation of the background properties of coronal loops using the observed properties of these waves. Seismology of these loops has estimated the density and magnetic field strength and De Moortel (2005), Banerjee *et al.* (2007), Nakariakov and Verwichte (2005) and Nakariakov (2007) are reviews on this subject.

Finally, EIT waves were discovered using the Extreme Ultraviolet Imaging Telescope (EIT) instrument onboard the Solar and Heliospheric Observatory (SOHO) satellite (Thompson *et al.*, 1998). These are large single-pulsed propagating fronts which appear to move unhindered throughout the corona after a large-scale event (such as a flare). They are believed to be associated with Moreton waves.

Overall, this has been a brief overview of the history of the Sun, its interior and atmosphere. For a more detailed introduction to the Sun, see Priest (1984) or Priest (2014) and see Aschwanden (2004) for a detailed overview of the solar corona.

1.4 Magnetohydrodynamics

The mathematical underpinning used in solar physics is called magnetohydrodynamics (MHD). It adds the effects of a magnetic field to the governing equations of fluid mechanics. More accurately, it is the melding of Maxwell's equations to the Navier-Stokes equations. This is credited to Hannes Alfvén, who won a Nobel Prize in Physics for this major contribution to science (Alfvén, 1942; Erdélyi and Fedun, 2007).

1.4.1 MHD equations

There are several equations that form the core of MHD and are solved in many different magnetic configurations. The ultimate aim is to understand how these configurations will evolve in time or how they react to external factors. Furthermore, they are solved to find what kind of waves these configurations can support and how these waves perturb the system. The MHD equations include many physical effects, however, ideal conditions are assumed: adiabatic, inviscid, non-radiative, no thermal conduction and no resistivity. This is ideal

MHD and the resulting equations are,

$$\frac{\partial \rho}{\partial t} + \nabla \cdot (\rho \boldsymbol{v}) = 0, \qquad \text{(Mass Conservation)}$$

$$\rho \frac{D\boldsymbol{v}}{Dt} = -\nabla p + \frac{1}{\mu}(\nabla \times \boldsymbol{B}) \times \boldsymbol{B} + \rho \boldsymbol{g}, \qquad \text{(Equation of Motion)}$$

$$\frac{D}{Dt}\left(\frac{p}{\rho^{\gamma}}\right) = 0, \qquad \text{(Energy Equation)}$$

$$\frac{\partial \boldsymbol{B}}{\partial t} = \nabla \times (\boldsymbol{v} \times \boldsymbol{B}), \qquad \text{(Induction Equation)}$$

subject to,

$$\nabla \cdot \boldsymbol{B} = 0, \qquad \text{(Solenoid Equation)}$$

$$p = k_B \frac{\rho}{m} T, \qquad \text{(Ideal Gas Law)}$$

$$\boldsymbol{E} = -\boldsymbol{v} \times \boldsymbol{B}, \qquad \text{(Ohm's Law)}$$

$$\boldsymbol{j} = \nabla \times \boldsymbol{B}/\mu. \qquad \text{(Electric Current)}$$

Here ρ is the density, $\boldsymbol{v}$ is the velocity, $\frac{D}{Dt}$ is the convective derivative $\left(\frac{\partial}{\partial t} + (\boldsymbol{v} \cdot \nabla)\right)$, p is the pressure, γ is the ratio of specific heats (5/3 for an ideal mono-atomic gas), $\boldsymbol{B}$ is the magnetic field, k_B is Boltzmann's constant, m is the mass, T is the temperature, $\boldsymbol{E}$ is the electric field, $\boldsymbol{j}$ is the current density and μ is the vacuum permeability.

There are actually eight partial differential equations for eight variables. Both $\boldsymbol{v}$ and $\boldsymbol{B}$ have three components each and we have the density and temperature. From this, the typical recourse is to examine the case of small perturbations for the MHD quantities, i.e.,

$$\begin{aligned}
\boldsymbol{B} &= \boldsymbol{B}_0 + \boldsymbol{B}_1(\boldsymbol{r}, t) \\
\boldsymbol{v} &= \boldsymbol{0} + \boldsymbol{v}_1(\boldsymbol{r}, t) \\
p &= p_0 + p_1(\boldsymbol{r}, t) \\
\rho &= \rho_0 + \rho_1(\boldsymbol{r}, t).
\end{aligned}$$

Here, subscripts are used to separate out the background ($\boldsymbol{B}_0$) and perturbation ($\boldsymbol{B}_1$) quantities. There is assumed to be no background flow and that all perturbations are much smaller than the background value (e.g., $\boldsymbol{B}_0 \gg \boldsymbol{B}_1$).

This leads to the linearised ideal MHD equations,

$$\frac{\partial \rho_1}{\partial t} + (\boldsymbol{v}_1 \cdot \nabla)\rho_0 + \rho_0(\nabla \cdot \boldsymbol{v}_1) = 0, \qquad \text{(Mass Conservation)}$$

$$\rho_0 \frac{\partial \boldsymbol{v}_1}{\partial t} = -\nabla p_1 + \frac{1}{\mu}(\nabla \times \boldsymbol{B}_1) \times \boldsymbol{B}_0 + \rho_1 \boldsymbol{g}, \qquad \text{(Equation of Motion)}$$

$$\frac{\partial p_1}{\partial t} + (\boldsymbol{v}_1 \cdot \nabla)p_0 - c_s^2 \left(\frac{\partial \rho_1}{\partial t} + (\boldsymbol{v}_1 \cdot \nabla)\rho_0 \right) = 0, \qquad \text{(Energy Equation)}$$

$$\frac{\partial \boldsymbol{B}_1}{\partial t} = \nabla \times (\boldsymbol{v}_1 \times \boldsymbol{B}_0), \qquad \text{(Induction Equation)}$$

$$\nabla \cdot \boldsymbol{B}_1 = 0, \qquad \text{(Solenoid Equation)}$$

where it is possible to define the first characteristic speed in MHD, the sound speed, $c_s^2 = \gamma p_0/\rho_0$. There is another important characteristic speed and that is the Alfvén speed, $c_A^2 = B_0^2/\sqrt{\rho_0}$. These equations need to then be applied to an equilibrium and since the focus is sunspots and pores, a cylindrical flux tube is the ideal choice.

1.4.2 MHD waves in cylindrical flux tubes

To understand the observed oscillations in sunspots and pores, it is important to investigate the nature of oscillations within an idealised model of these structures. However, before this occurs, a quick comment on MHD waves in a uniform model. This model is a uniform unbounded, i.e., infinite atmosphere with a background magnetic field that is purely vertical. Table 1.1 summarises how MHD wave modes behave within this model. Three wave modes are present in this model, the Alfvén mode, the fast mode and the slow mode. To summarise, the Alfvén perturbs the velocity in a perpendicular direction to its propagation direction. It only propagates along the magnetic field and not perpendicular. For the fast and slow wave mode, the velocity perturbation is not perpendicular to the angle of propagation. The important distinction between the fast and slow mode in this model is that the slow mode does not propagate perpendicular to the background magnetic field, while the fast mode is isotropic. The effect of plasma-β in this regime is to simply change the speed at which the slow and fast mode will propagate at. This results tend to be summarised in Friedrich diagrams. In the context of a cylindrical tube, only the fast and slow modes are discussed.

The most iconic investigation into this was undertaken by Edwin and Roberts 1983. Their analysis is based on the non-slender flux tube, where the tube radius is greater or equal to the wavelength of the oscillations. Furthermore, it ignores the effects of gravity (i.e., the stratification of the atmosphere), which is important when the wavelength is comparable to the atmospheric scale

		$\beta \gg 1,\ c_A \ll c_s$	$\beta \ll 1,\ c_A \gg c_s$
$\boldsymbol{k} \cdot \boldsymbol{v}_1 = 0$	$\boldsymbol{k} \| \boldsymbol{B}_0$	Alfvén wave, $c_{ph}^2 \sim c_A^2$	Alfvén wave, $c_{ph}^2 \sim c_A^2$
	$\boldsymbol{k} \perp \boldsymbol{B}_0$	Alfvén wave – does not propagate	Alfvén wave – does not propagate
$\boldsymbol{k} \cdot \boldsymbol{v}_1 \neq 0$	$\boldsymbol{k} \| \boldsymbol{B}_0$	Fast wave, $c_{ph}^2 \sim c_s^2$ approximately isotropic magnetic and kinetic pressure in phase Slow wave, $c_{ph}^2 \sim c_A^2$ magnetic and kinetic pressure out of phase	Fast wave, $c_{ph}^2 \sim c_A^2$ approximately isotropic magnetic and kinetic pressure in phase Slow wave, $c_{ph}^2 \sim c_s^2$ magnetic and kinetic pressure out of phase
	$\boldsymbol{k} \perp \boldsymbol{B}_0$	Fast wave, $c_{ph}^2 \sim c_s^2$ approximately isotropic magnetic and kinetic pressure in phase Slow wave – does not propagate	Fast wave, $c_{ph}^2 \sim c_A^2$ approximately isotropic magnetic and kinetic pressure in phase Slow wave – does not propagate

Table 1.1 The behaviour of each MHD wave mode in a uniform unbounded magnetised plasma. It summarises the phase speeds, propagation direction and the effect of varying plasma-β on each MHD wave mode. Adapted from Jess *et al.* (2015).

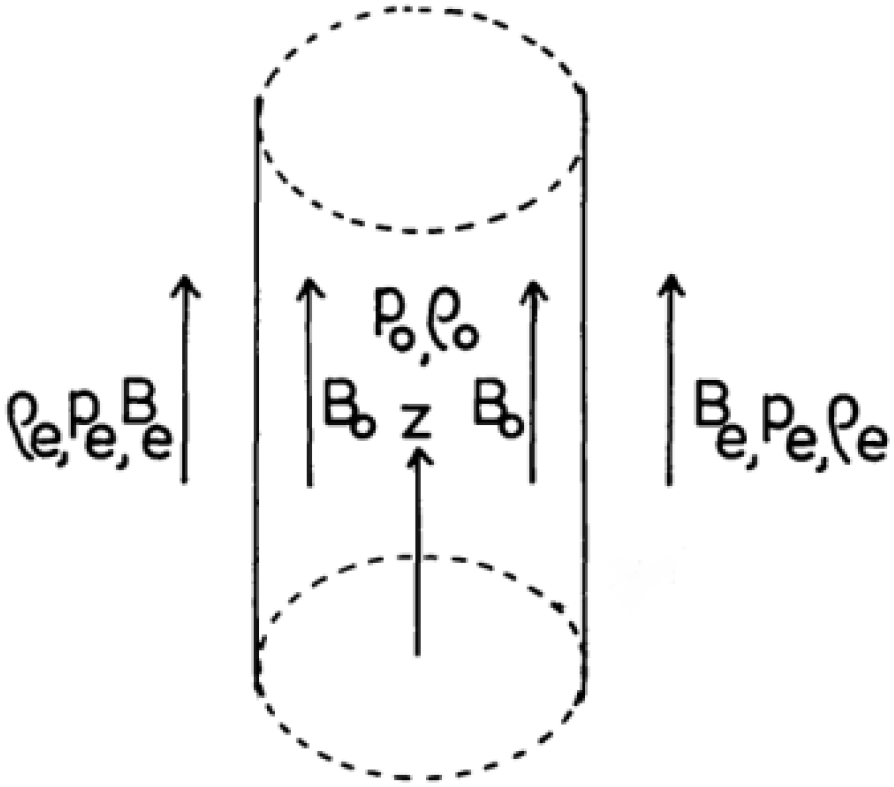

Fig. 1.10 The equilibrium conditions used to model wave behaviour in a magnetic flux tube. Image is a modified version of Figure 1 from Edwin and Roberts (1983).

height and in the photosphere this is the case (Edwin and Roberts, 1982). It is important to note that in thin flux tubes, there are two other characteristic wave speeds. One is a subsonic, sub-Alfvénic speed, c_T (defined later on), and the other is the "mean" Alfvén speed, c_k.

The model is as follows, a cylindrical magnetic flux tube of radius a with its own density (ρ_0), pressure (p_0) and magnetic field ($B_0\hat{\mathbf{z}}$) is embedded in a magnetic environment with a similar profile ($B_e\hat{\mathbf{z}}$, ρ_e and p_e). The density and pressure are uniform throughout the medium. Figure 1.10 is a schematic drawing of this model.

This is the starting point for deriving the dispersion relation for MHD waves in a magnetic flux tube. It is assumed that this system is in equilibrium. Perturbations to the equilibrium conditions then add extra terms to the ideal MHD equations (the equations in Section 1.4.1). By introducing the Fourier decomposition of the perturbations, they show that the amplitude term is the Bessel equation. When bound on the axis of the cylinder ($r = 0$), two solutions exist for either the body or surface wave. In the external atmosphere, the assumption of no propagation of energy away from or towards the cylinder allows the solution for the amplitude to be found for the external atmosphere.

Furthermore, the kinetic and magnetic energy density tend to zero as $r \to \infty$. Continuity at the boundary ($r = a$) has to be kept (radial velocity component v_r, and the total pressure) which yields the dispersion relations for surface waves and body waves (Edwin and Roberts, 1983). These are,

$$\rho_0(k^2c_A^2 - \omega)m_e\frac{K_n'(m_e a)}{K_n(m_e a)} = \rho_e(k^2c_{Ae}^2 - \omega)m_0\frac{I_n'(m_0 a)}{I_n(m_0 a)} \qquad \text{(Surface, } \mathrm{m}_0^2 > 0\text{)}$$

$$\rho_0(k^2c_A^2 - \omega)m_e\frac{K_n'(m_e a)}{K_n(m_e a)} = \rho_e(k^2c_{Ae}^2 - \omega)n_0\frac{I_n'(n_0 a)}{I_n(n_0 a)} \qquad \text{(Body, } \mathrm{m}_0^2 = -n_0 < 0\text{)}$$

where, K_n and I_n are Bessel functions of order n, K_n' and I_n' are the derivatives of the Bessel functions, m_0 and m_e are the internal and external wavenumber, defined as,

$$\frac{(k^2c_s^2 - \omega^2)(k^2c_A^2 - \omega^2)}{(c_s^2 + c_A^2)(k^2c_T^2 - \omega^2)},$$

and c_T is the tube speed,

$$c_T = \frac{c_s^2 c_A^2}{c_s^2 + c_A^2}.$$

Finally, these dispersion relations are solved under photospheric conditions (plasma-β << 1, such that, $c_A > c_{se} > c_k > c_{Ae}$) and the solutions are plotted in Figure 1.11.

These dispersion relations are important as they detail the way in which waves propagate through numerous flux tube sizes. It shows the limits of the wave solutions indicating in what regimes they cannot exist. Surface waves are dispersive as their phase speed depends on the wavenumber. There are slow body waves which are both sausage, kink, and fluting modes and these modes have a phase speed between the tube and sound speeds. Slow surface waves have phase speeds close to the tube speed. There is also a surface wave with a phase speed close to the kink speed and another surface wave near the sound speed. If one can measure the phase speed of an observed wave and the ka of the flux tube, one can also likely identify the observed waves. This has been attempted by Moreels *et al.* (2015a).

One factor that has been neglected is the mode number (n), its value governs the way in which the wave perturbs the flux tube. This gives us the name: sausage ($n = 0$), kink ($n = 1$) and fluting ($n > 1$). These different wave modes cause characteristic physical effects which can be used to identify each different wave mode.

Figure 1.12 shows the physical changes to the flux tube, caused by each different wave mode. Below, when a quantity is talked about, the focus is on the perturbation of that quantity. The first diagram (labelled a), shows how the slow MHD sausage mode affects the flux tube. The velocity is primarily

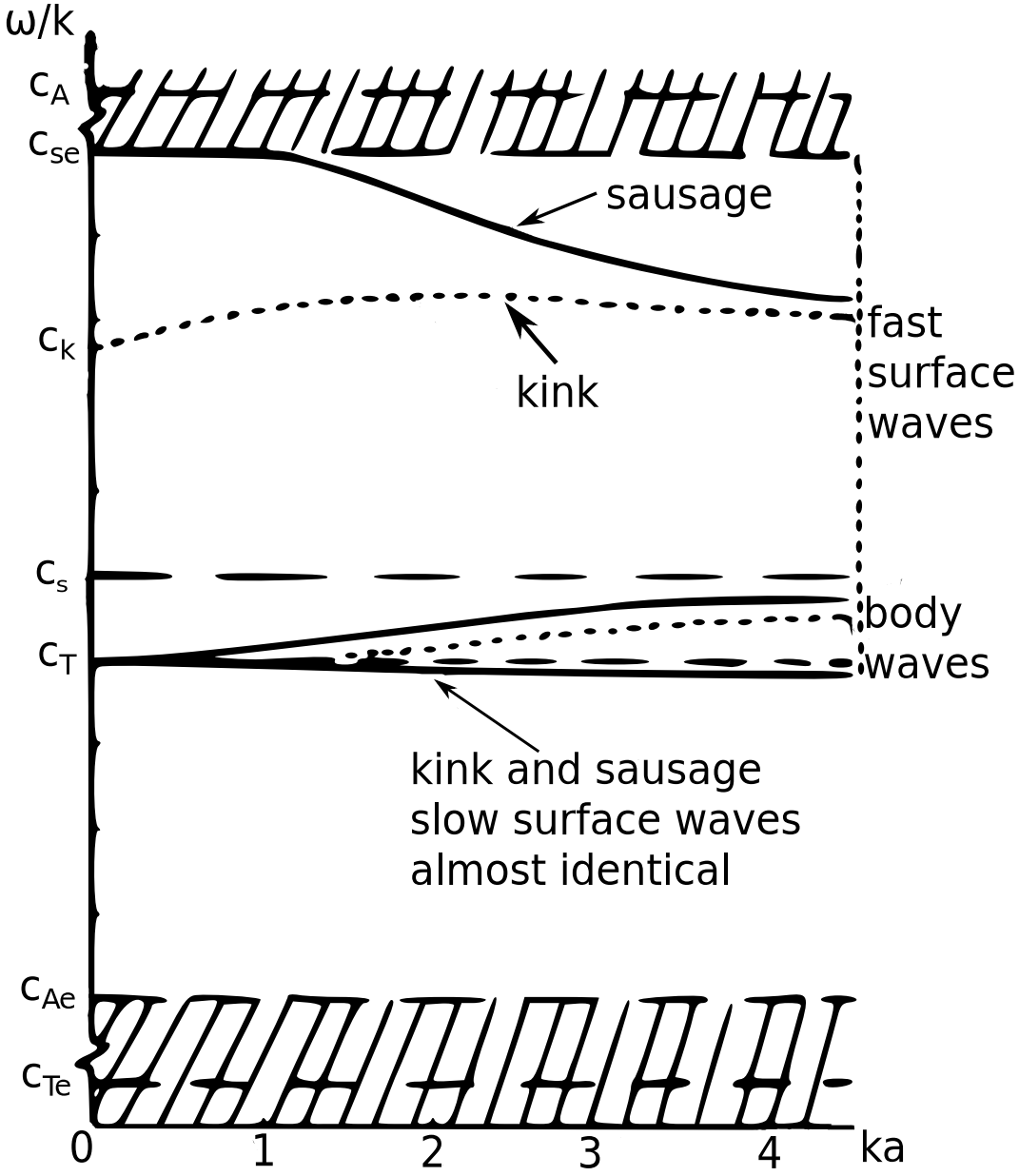

Fig. 1.11 The dispersion relationship derived from the MHD equations under photospheric conditions ($c_A > c_{se} > c_k > c_{Ae}$). The hatched areas are the excluded values of ω and ka. Image is a modified version of Figure 2 from Edwin and Roberts (1983).

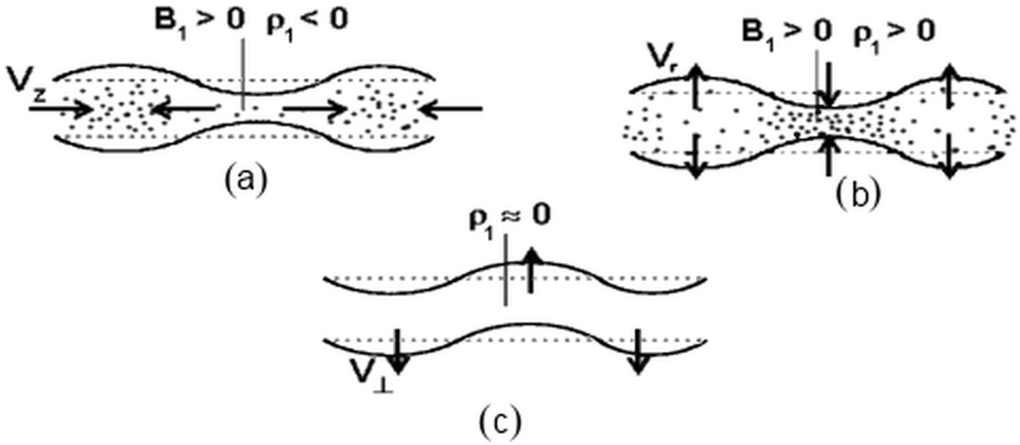

Fig. 1.12 The physical effects that each MHD mode has on a cylindrical flux tube. (a) The slow magnetoacoustic waves (slow sausage mode) which cause anti-phase behaviour between the intensity and the magnetic field. (b) The fast magnetoacoustic waves (fast sausage mode) which cause in phase behaviour between the intensity and the magnetic field. (c) The fast magnetoacoustic waves (fast kink mode) which cause no magnetic field perturbations but cause $\pi/2$ phase behaviour between the intensity and velocity perturbation. Image is a modified version of Figure 1 from Wang (2004).

longitudinal. Furthermore, when the flux tube contracts the density decreases in that region indicating a phase difference of π, but this is also the same phase difference for the cross-sectional area and total intensity. The second diagram (labelled b), shows the fast MHD sausage mode. The velocity is primarily radial and when the flux tube contracts the density in that region increases unlike the slow MHD sausage mode. This means that the cross-sectional area and total intensity are in phase, as well as the magnetic field. These diagrams have been improved over time and movies have been created which can be found within several papers (Jess *et al.*, 2015; Morton *et al.*, 2012) and online sources (http://www2.warwick.ac.uk/fac/sci/physics/research/cfsa/research/wpc/vis/ or http://swat.group.shef.ac.uk/fluxtube.html). Finally, the last diagram (labelled c) shows the MHD kink mode. It is non-compressible (to the first order linear limit, long wavelength approximation) and perturbs the flux tube axis. This makes it very difficult to identify unless it is possible to isolate the central axis of the flux tube. This is quite difficult for a sunspot or pore, but it has been done for spicules and fibrils and kink and Alfvén waves have been observed (see Section 1.3.2 for more details).

While these are toy arguments and descriptions, these phase relations have been derived by several authors (Fujimura and Tsuneta, 2009; Moreels and Van Doorsselaere, 2013; Moreels *et al.*, 2013, 2015a). They have taken complex models of embedded flux tubes to derive an almost full set of phase relations for many of the MHD wave modes and whether they are standing

	$\phi_B - \phi_v$	$\phi_v - \phi_I$	$\phi_I - \phi_B$	$\phi_S - \phi_I$
Slow sausage propagating	π	0	π	0
Slow sausage standing	$\pm\pi/2$	$\pm\pi/2$	π	0
Fast sausage propagating[6]	$[0,\pi]$	$[-\pi/2,0]$	$[-\pi/2,0]$	π
Fast sausage standing[6]	$\pm\pi/2$	$\pm\pi/2$	$[0,\pi]$	π
Fast kink propagating	$\pm\pi/2^3$	N/A^4	N/A^4	N/A^4
Fast kink standing	$[\pi/2^1, \pi^2]$	N/A^4	N/A^4	N/A^4

Table 1.2 Shows the phase differences between three observables: the intensity, Doppler velocity and the magnetic field for each type of MHD wave and whether the wave is standing (S) or propagating (P). 1 - Wave propagating anti-parallel to the magnetic field. 2 - Wave propagating parallel to the magnetic field. 3 - Depending on the distance to the reflection boundary. 4 - Kink modes are incompressible and thus have zero intensity fluctuations. 5 - Fast sausage mode has zero LOS velocity fluctuations. 6 - Surface mode only. Collated from these authors, Fujimura and Tsuneta (2009); Moreels and Van Doorsselaere (2013); Moreels *et al.* (2013, 2015a); Wang (2004)

or propagating. The main conclusions from Moreels and Van Doorsselaere (2013) and Moreels *et al.* (2013) is that fast and slow sausage modes have a different phase behaviour; namely that slow modes have an in phase behaviour (i.e., 0° phase difference between the cross-sectional area and the Lagrangian intensity oscillations), while fast modes have an anti-phase behaviour (i.e., 180° phase difference between the cross-sectional area and the Lagrangian intensity oscillations). Throughout this thesis, the Lagrangian intensity variations, i.e., the intensity variations when following the motion of the plasma, is used.

Table 1.2 summarises the phase relations between the intensity, Doppler velocity, magnetic field and for the cross-sectional area and intensity for each wave mode and whether it is a standing or propagating wave. This table contains the information that will be in this thesis, in order to identify the observed oscillations which occur within the numerous magnetic structures analysed. Since the focus has been on compressive perturbations, kink waves are neglected from this point onwards as are Alfvén waves. However, see these recent reviews for kink and Alfvén waves with regards to theory and observations Mathioudakis *et al.* (2013) and Jess *et al.* (2015). It is important to note that the focus has been exclusively on the MHD sausage mode within this thesis.

The previously derived theory (Jess *et al.*, 2015; Moreels and Van Doorsselaere, 2013; Moreels *et al.*, 2013, 2015a) gives an insight into the observational signatures that MHD sausage modes will exhibit within a magnetic waveguide. While the base signature will be the change of the cross-sectional area with respect to time and that this signal will be either in phase or out of phase with the total intensity signal. What is missing from this, is whether the two MHD

sausage modes (slow and fast) have characteristics that will make it possible or difficult to observe. Moreels and Van Doorsselaere (2013) suggest that the fast MHD sausage mode, in photospheric conditions, should be able to perturb the radius up to 20%. For the slow MHD sausage mode, the type of wave becomes important. For the slow MHD sausage surface mode, the perturbation amplitude is very small, below the resolution of current telescopes. However, the slow MHD sausage body mode, should be able to perturb the radius up to 10%. The reason for this difference between the slow and fast mode is that the dominant velocity perturbation is longitudinal for the slow mode while it is radial for the fast mode. Jess *et al.* (2015) suggest that the fast MHD sausage mode has a larger cross-sectional area perturbation as well as stronger density perturbations compared to the MHD slow sausage mode. Overall, the current research suggests that the effect of MHD sausage modes is observable with the current generation of ground-based telescopes.

Chapter 2

Data collection and analysis overview

2.1 Introduction

The current state of solar observations has never been more ideal. There is currently constant space-based monitoring of the Sun but also a myriad of high-quality ground-based solar telescopes in existence. This is coupled with a few small space-based telescopes and sounding rocket experiments. Furthermore, within the next decade, the largest ground-based solar telescope will open called the Daniel K. Inouye Solar Telescope (DKIST, formerly the Advanced Technology Solar Telescope, ATST) and several highly-advanced satellites will be launched (two of which will move in to very close orbit to the Sun). This will be an important era for solar physics.

Numerous sources of solar data were used in the analyses presented here. Two telescopes will be the primary focus of this chapter: the Swedish Solar Telescope (SST) and Solar Dynamics Observatory (SDO). While data from other ground-based telescopes are used, having spent 10 days at the SST it receives a larger focus. These two telescopes offer some of the highest quality data available to a solar physicist.

Data that is taken directly from any telescope will need to be corrected for any artefacts and this process is called data reduction. Data reduction requires the creation of specific files called darks, flats and pinhole images. Darks are the images when there is no incoming light and displays the background noise of the camera. Flats are the images when the incoming light is uniform and this displays the imaging artefacts that come from the optics. Pinhole are images used to align the cameras along the optical path of the telescope. These images are applied onto the original data to reduce any imaging artefacts that are present within the original data. The final step is to remove the effects of the Earth's atmosphere and these methods are detailed later on. It should be noted that all data used had been reduced to a science ready level.

Once the data is reduced, the method of analysis will need to be considered and it will vary depending on the scientific aims. Here, the aim was to measure the cross-sectional area and total intensity through time of sunspots and pores. Once these two properties have been measured, deducing any periods within these signals and calculating the phase difference between them is required and numerous signal analysis methods exist that aim to do just that. Three methods are employed which are the fast Fourier transform (FFT), Wavelet Transform (WT) and Empirical Mode Decomposition (EMD).

In this chapter, the telescopes and instruments will be details then the signal analysis methods are covered and the chapter ends on a brief analysis into the method used to measure the cross-sectional area for two example magnetic flux tubes.

2.2 Sources of solar data

The work detailed within this thesis uses data from five telescopes: Swedish Solar Telescope (SST), Solar Dynamics Observatory (SDO), Dunn Solar Telescope (DST), Dutch Open Telescope (DOT) and the Swedish Solar Telescope (SVST). They are outlined below.

2.2.1 Swedish solar telescope

The Swedish Solar Telescope is a one metre vacuum solar telescope located at the Roque de los Muchachos Observatory on La Palma in the Canary Islands. The SST was the replacement for the Swedish Vacuum Solar Telescope which used to occupy the same site and will be talked about later in this chapter. The SST has a 1.1 m lens, of which only 1 m is usable, which is connected to a several storey vacuum tower. The light collected travels down the vacuum tower into a corrector system and then to the optics bench. The usage of a vacuum tower means that the collected light does not pass through any air. This reduces any distortion that comes from the air being heated by the beam of light and improves the overall image quality. The scale of the SST can be seen in Figure 2.1. It shows the building that houses the SST and the tower that contains the vacuum tower can be seen.

Further to this, the SST is equipped with an adaptive optics (AO) system. AO is a term used for a process that will adjust the optics of the instrument in order to reduce the effects of turbulence from the Earth's atmosphere. At a basic level, the AO at the SST has a sensor that monitors the wavefront of the incoming light wave and analyses how the wavefront is distorted. This distortion is counteracted by deforming a lens, made of a piezoelectric material, with a specific set of voltages to restore the wavefront. This is not the same method used by larger and newer optical telescopes used for astrophysics that have a deformable primary mirror in conjugation with a powerful laser.

The SST has two instruments, the *CRisp Imaging SpectroPolarimeter* (CRISP) and the *TRI-Port Polarimetric Echelle-Littrow* (TRIPPEL). TRIPPEL is a spectrograph with a constant diffraction grating spacing but has a shape that is similar to a sawtooth-shaped step function. See Kiselman *et al.* (2011) for a full overview of this instrument.

CRISP is a tunable dual Fabry-Perot filter system. The wavelength range is in the red wing (510-860 nm) and the light firstly goes through a selectable pre-filter dependent on the goals of the current observational sequence. This allows many wavelengths to be chosen with one instrument, which is required in order to observe the height variation of the solar atmosphere. The Fabry-Perot

Fig. 2.1 An image of the Swedish Solar Telescope taken from a ledge near the caldera on the island of La Palma that is part of the Canary Islands. The primary mirror housing can be seen at the top of the image, while the tower that conceals the vacuum tower can be seen beneath it. Copyright goes to the author.

Pre-filter	Wavelength (nm)	FWHM (nm)	Line Core Height (km)
Mg b	517.33	.3	≤ 1000
Na D	589.7	.38	≤ 500
Fe I	630.26	.44	≤ 250
Ca II k	854.16	.93	≤ 1300
H α	656.2	.49	≤ 1500

Table 2.1 Summary of the more common wavelengths that are selectable with CRISP. Each filter has a name, wavelength at the line-core and the Full Width at Half Maximum (FWHM) and an average formation height of the line-core, which come from Jess *et al.* (2010).

is made from a pair of partly reflective mirrors that are separated by a small distance. By varying the distance between the two mirrors, a specific wavelength can escape the mirror system and go to the cameras. With the ability to vary the distance between the mirrors, the Fabry-Perot system is able to investigate the line profile of many elements. Table 2.1 has approximately a fourth of the wavelengths available with CRISP. The selection of wavelengths here are the commonly used filters that appear in published papers. For example, the Fe I 630.26 nm line is used to observe the photosphere and clear granulation can be seen. More importantly, this wavelength is used to measure the photospheric magnetic field.

An important wavelength is 656.3nm and is commonly referred to as Hα. It is when an electron drops one energy level from the third shell to the second in a Hydrogen atom. This transition is the easiest method to observe the chromosphere and forms approximately 1.5 Mm from the base of the photosphere. Understanding the chromosphere has become a topic of heavy interest as the "Coronal Heating Problem" shifted from the corona to the chromosphere over the past decade (Aschwanden *et al.*, 2007). Since the line core of Hα samples the chromosphere, understanding how this line is formed within the solar atmosphere has become a very important topic.

However, Hα line formation is a difficult topic. The line is highly complex, most likely it is dependant on numerous physical effects such as ionization or non-LTE effects. Currently, the standard understanding of Hα comes from radiative MHD simulations done, for example by Leenaarts *et al.* (2007) and Leenaarts *et al.* (2012). From these two sources, a few properties and observations of the Hα line core can be summarised.

Current research suggests that structures that appear darker, such as fibrils, in the line-core are formed higher compared to other features. Further, the opacity of Hα that is formed in the upper chromosphere is temperature insensitive. This means that the opacity of the line is mainly determined

by the mass density at these regions. The results suggest that fibrils are mainly located within magnetically dominated (i.e., low plasma-β) regions between photospheric field concentrations of opposite polarity. These fibrils are aligned with the local magnetic field direction are located in regions where the local density is larger compared to the background chromosphere. This effects the average formation height for Hα by making it higher and thus the intensity is lower. Therefore, fibrils can be used to trace out regions of enhanced chromospheric mass density.

Finally, the light beam at the SST is spilt into two parts when CRISP is in use. The red wing goes to CRISP, while the blue part goes to a series of broadband cameras. These wavelengths are G-band and Ca K which sample the photosphere. These offer some of the highest resolution images of the solar photosphere to date and are only used when the seeing is excellent. Examples of the data from these cameras can be seen on the SST website (http://www.solarphysics.kva.se/)

To reduce SST data, the steps detailed at the start of this chapter will occur. However, the method used to remove the effects of the Earth's atmosphere from SST data is called Multi-Object Multi-Frame Blind Deconvolution (MOMFBD). This is a complex and computationally demanding method to improve the quality of the data without affecting the cadence of the observation data. See van Noort *et al.* (2005) for a full breakdown of this reduction method.

2.2.2 Solar dynamics observatory

Solar Dynamics Observatory is one of the latest space-based telescopes launched by National Aeronautics and Space Administration (NASA Pesnell *et al.* 2012). It can be considered as the replacement for the Solar and Heliospheric Observatory (SOHO Domingo *et al.* 1995) and the Transition Region and Coronal Explorer (TRACE Strong *et al.* 1994). Since 2010, it has been observing the Sun constantly beaming large quantities of data back to Earth. Without Earth's atmosphere in the way, it offers some of the clearest observations of the entire Sun to date. The spacecraft houses three instruments: the *Extreme Ultraviolet Variability Experiment* (EVE Woods *et al.* 2012), the *Helioseismic and Magnetic Imager* (HMI Schou *et al.* 2012) and the *Atmospheric Imaging Assembly* (AIA Lemen *et al.* 2012).

HMI measures LOS velocities as well as the LOS and vector magnetic field of the photosphere. AIA is a multi-wavelength instrument and is able to take images of the solar surface to the outer reaches of the solar atmosphere. This has offered an unprecedented view of the many layers of the solar atmosphere at the same time. This view can be seen in Figure 2.2, which shows the full

temperature range of AIA as well as an HMI image. The figure showcases almost every wavelength that is available on AIA, from the low temperature lines such as 170 nm that sample the photosphere, to the hotter lines that display the complex structure within the corona such as 13.1 nm. From HMI, there is a LOS magnetogram that showcases the magnetic field within the photosphere.

2.2.3 Other ground telescopes

Datasets from three other ground-based telescopes are used within this thesis. What follows is a brief summary of each one and more details are given within the chapters where the data from these telescopes is used.

First, the Swedish Vacuum Solar Telescope which was the predecessor to the current SST. It had a 47.5 cm mirror with several wavelength narrowband filters with no AO. The narrowband filters were not too dissimilar to the wavelengths in Table. 2.1. See Scharmer and Lofdahl (1991) for a full overview of the SVST.

Second, the Dutch Open Telescope is an open-air solar telescope that is now retired. The DOT is located next to the SST on La Palma and it has a very compact design that is quite different to the SST. It has a mirror that is slightly smaller than the previous SVST, at only 45 cm. The full instrumental setup consisted of 6 cameras each with a different narrow band filter. With no AO it used a more unconventional method to lessen seeing effects. The telescope was on a mount several meters high which was open to the atmosphere. As such, the strong winds blew across the mirror reducing seeing effects from temperature gradients that are caused by the ground which reduced image distortion. Furthermore, it used high frequency cameras that allowed speckle reconstruction. Speckle reconstruction is a method to reducing the effect of Earth's atmosphere on the images obtained. By using high-speed camera able to capture many frames in one second, these frames are combined in order to form a model of the distortion from the atmosphere. This effect however, increases the cadence of the observation. See Keller and von der Luehe (1992) or Wöger *et al.* (2008) for a full analysis of speckle reconstruction and Rutten *et al.* (2004) for a full overview of the DOT.

Finally, the Richard B. Dunn Solar Telescope, located at Sacramento Peak in New Mexico and is run by the National Solar Observatory (NSO). It has a 76 cm mirror and is a vacuum telescope similar to the SST but its design is unique. The tower itself moves, unlike the SST where it is just the telescope mount, it seated on a ring of liquid mercury and it allows it to rotate to track the Sun throughout the day. It has many instruments but the focus here is on two of them: *Rapid Oscillations in the Solar Atmosphere* (ROSA) and

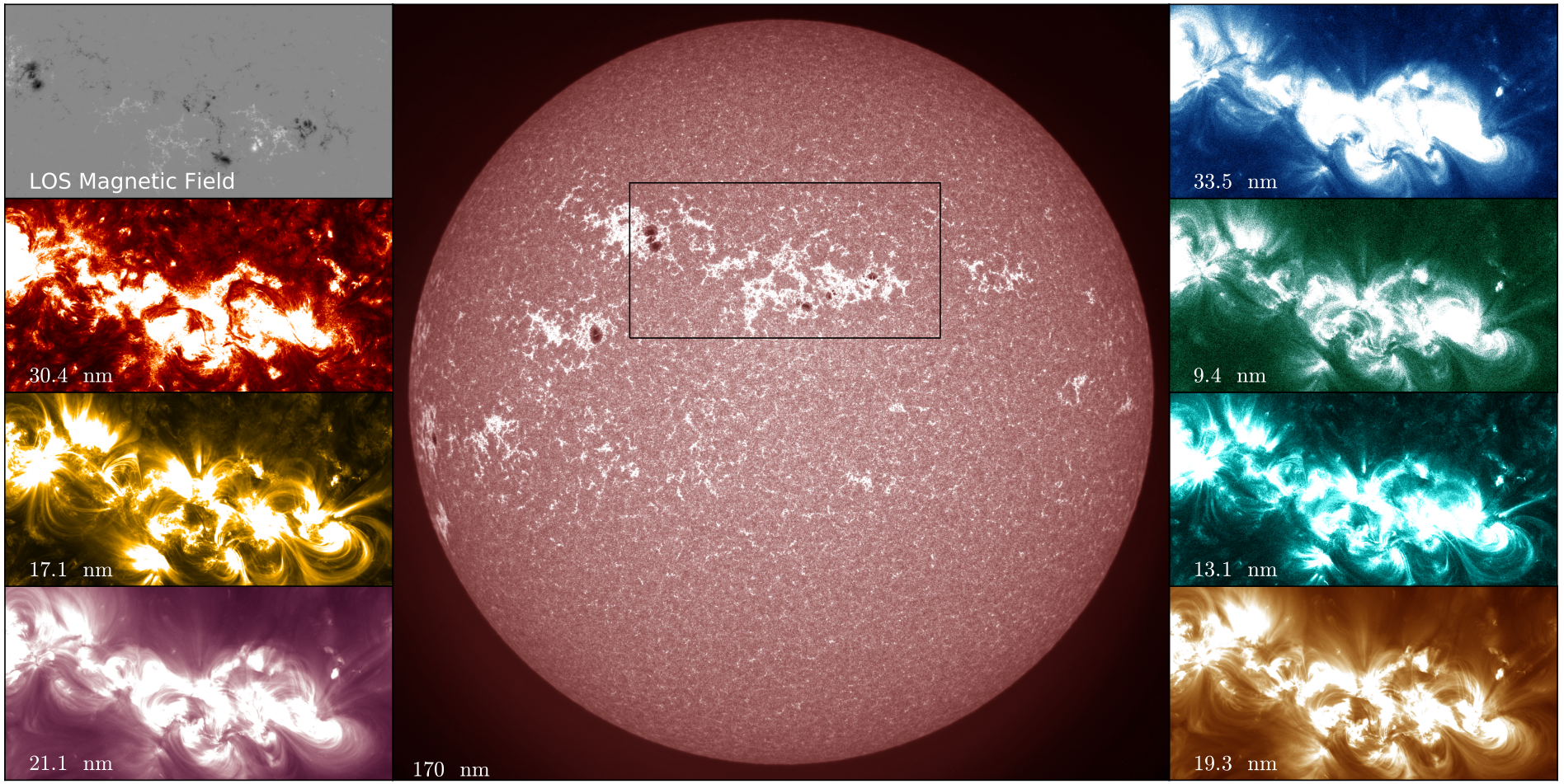

Fig. 2.2 The field of view of the Solar Dynamics Observatory (SDO) satellite. Each image shows a different wavelength that is captured by two of the instruments on SDO, the Atmospheric Imaging Assembly (AIA) and Helioseismic and Magnetic Imager (HMI). The images are taken on the 17$^{\text{th}}$ of April 2015 focusing on AR 12326. The columns on the side go downwards in increasing temperature response. The 160 nm and 450 nm filter of AIA is missing from the image.

Interferometric Bidimensional Spectrometer (IBIS). ROSA is a synchronised 6 camera system similar in principle to the system on the DOT. It captures images at high frequency rates and uses narrowband wavelength filters that sample the photosphere and chromosphere. Much like the DOT, it uses speckle reconstruction to improve the quality of the images, while IBIS is similar to CRISP at the SST. It consists of two Fabry-Perot interferometers that operates in the red wing (550-860 nm) and allows in-depth line scans for specific wavelengths as well as measuring polarized light in spectropolarimetric mode. See Jess *et al.* (2010) and Cavallini (2006) for a full overview of ROSA and IBIS respectively.

2.3 Signal analysis

Once the process of data acquisition is finished and the data has been reduced using methods that are specific for that telescope or instrument, analysis of the data can begin. The method used will vary depending on the overall science goal or aim. For example, statistical studies require crunching through large quantities of data in order to categorise the general properties of the phenomenon that is under investigation. Other studies will focus on single events, either due to the lack of a large selection of data or if the event under investigation is rare. The analysis undertaken within this thesis is focused on measuring the properties of MHD waves in several sunspots and pores and later a single dataset studying RPWs.

From Chapter 1, it is clear that to observe MHD sausage waves in cylindrical structures, the phase relations between specific observational quantities such as the cross-sectional area and total intensity are required. While further phase relations are available, the two quantities used were the ones only possible with the ground-based data available at the time. As a result, the focus has been on the cross-sectional area and total intensity perturbations. Once these signals have been measured from the datasets used, the periods and phase difference of these signals must be found. The methods used are the Fast Fourier Transform (FFT), wavelets and Empirical Mode Decomposition (EMD) and are discussed below.

2.3.1 Fast Fourier transform

The first method is the Fast Fourier Transform (FFT). Its name is a reference to the fact that the FFT is very fast computational algorithm of the Discrete Fourier Transform (DFT). It was first introduced by Cooley and Tukey (1965). The Fourier Transform is a mathematical method to decompose a signal which

is assumed to be periodic into its constituent frequencies. Generally, it is common to have a real-valued signal input into the FFT and the resulting output is a complex number. This complex number contains both the amplitude and phase of the sinusoidal component. The absolute value of this output is the amount (or power if squared) of each frequency in the original signal, while the phase is the arctan of the complex and real parts.

An example of this can be seen in Figure 2.3. The top left image is of an artificial signal, of the form,

$$\sin\left(2\pi\frac{x}{5}\right) + \cos\left(2\pi\frac{x}{10}\right) + 5 \times \text{random noise},$$

where the noise is random samples from a uniform distribution over the range 0-1. This means that the mean is 0.5 and the standard deviation is 0.3. This signal can represent a signal at one pixel or a cross-sectional area signal. The top right image is the output after this signal is passed into the FFT. It is a power spectrum, where power is a function of frequency. The two peaks that can be seen correspond to the two frequencies of the artificial signal. The small peaks that are littered in the power spectrum correspond to the uniform noise that was added to the signal.

The nature of signal analysis means that each individual method has both positives and negatives. Generally, the type of signal or the overall aim will determine the method used. To start, input signals have a finite length and many signal analysis methods assume infinite length, which is the case for the Fourier Transform. This fact means that artefacts are introduced as a result, however, this is not unique to the FFT and most signal analysis algorithms suffer from this issue. The FFT has an effect known as frequency leakage. It is where, if the input signal is non-periodic or the input signal has no closed form transform, there is smearing in the power spectrum. This means that the power is not confined to the correct frequency and spreads, so if there is an other frequency close to a strong frequency, it will be masked. This can be overcome by using a window function, through a process called windowing. These window functions are non-zero in a chosen interval and are then multiplied to the original signal before it is then put through the FFT. The shape of these window functions varies and numerous windows have been created. This alters the outcome of the FFT in order to reduce the effects of spectral leakage. Furthermore, another important part of the FFT is the output can be reversed. It is possible to recover the original signal using the Inverse FFT (IFFT). This fact means that one can create a bandpass filter and apply it to the Fourier space. This is done in order to remove parts of the Fourier space that contains information that is unnecessary and thus return a

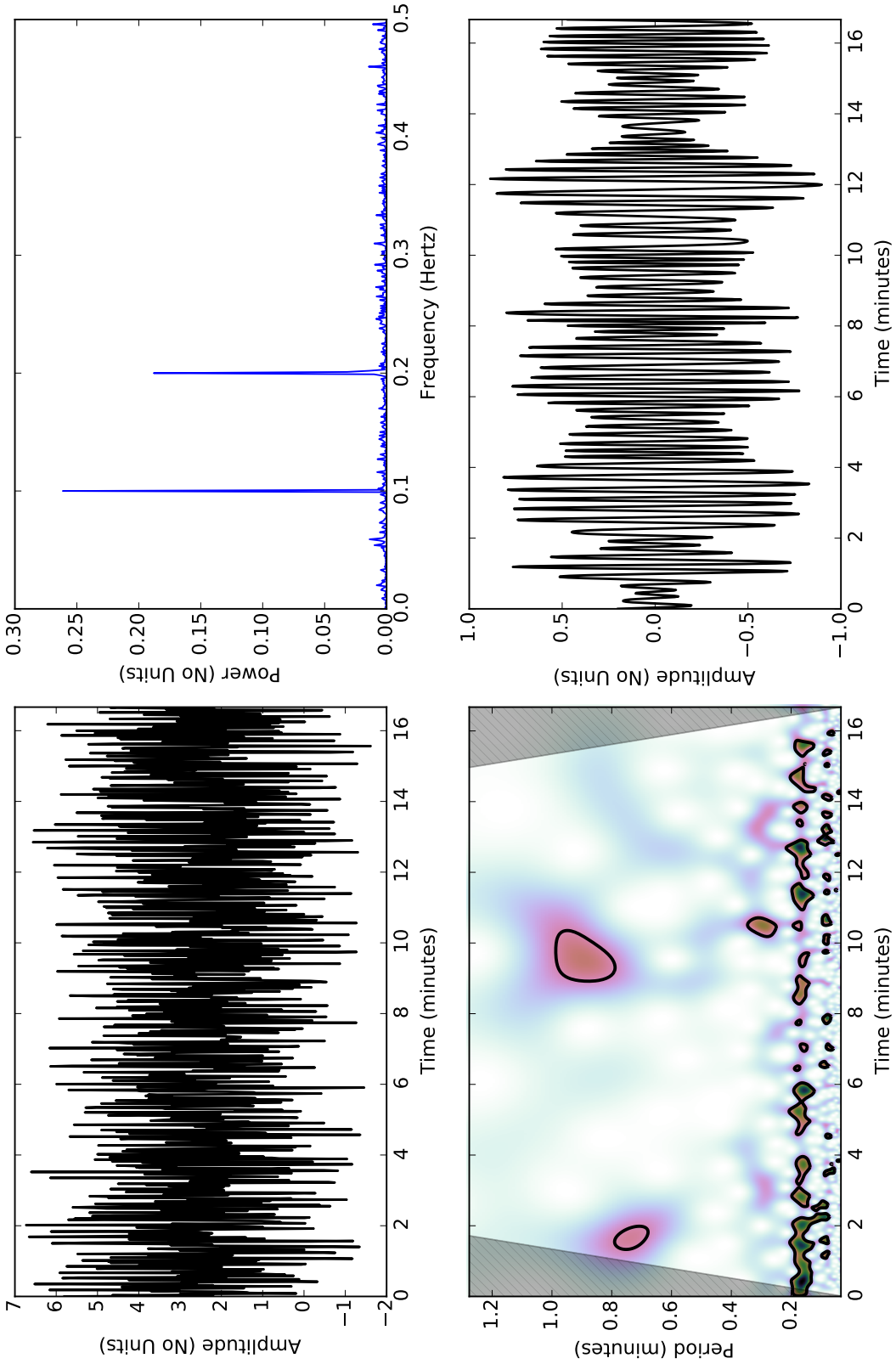

Fig. 2.3 An example of the signal analysis methods. The upper left plot is of an artificial signal with noise. The upper right plot is a power spectrum from the FFT. The largest two peaks shows the frequencies within the artificial signal. The bottom left plot is a wavelet power spectrum. It expands on the FFT by offering a 2D view of the frequency spectrum with time. The bottom right plot shows an IMF output from a EMD algorithm. The IMF contains one of the periods from the artificial signal used and this corresponds to the smaller frequency within the artificial signal.

new signal to see the behaviour at specific frequencies. It is a commonly used method in signal analysis and is used within Chapter 5.

Finally, the significance of the FFT power spectrum is an important factor, since it is vital to establish if the periods are above noise level. While there are numerous methods to achieve this, here is a brief overview of just two. The first method is described by Scargle (1982) and Horne and Baliunas (1986). It relies on normalising the power spectrum and assumes that the noise in the data is truly random. This means that the probability of the noise at any given frequency being above a power value, z, is exponentially distributed, scaling as $\exp(-z)$. This defines the "false-alarm probability" at which a given power is equal to, $1-(1-\exp(-z))^{N_i}$, where N_i is the number of frequencies contributing to the power spectrum. The second method is a Monte-Carlo method known as Fisher Randomization. Given a signal, the FFT of the data is calculated and the power of the highest peak is determined. Then the original signal is then randomly permuted and the FFT is re-calculated. If the highest peak in the new FFT is higher than that of the original, '1' is added to the count. The process is repeated the desired number of times and the false alarm probability is returned at the end and it is simply the count divided by the number of permutations (Linnell Nemec and Nemec, 1985).

2.3.2 Wavelet transform

The second method employed is called the Wavelet Transform. A wavelet is a zero mean function that is constrained in time and frequency space i.e., localised within these specific domains (Farge, 1992). The base function used is called the mother wavelet and variations of this function are called daughters. This factor is important, as the FFT will, when given a 1D signal, output a 1D power spectrum. The wavelet algorithm will return a 2D spectrum where the extra dimension is time. This means you can also know what frequency is within the signal but also at what time in the signal that frequency exists and its duration. This is a more powerful method due to this fact, but also, each mother wavelet have different properties so depending on the goal of the signal analysis, by changing the mother wavelet different information can be extracted. For example, the wavelet chosen here is the Morlet Wavelet. It is defined as,

$$\Psi_0(\eta) = \pi^{-1/4} \exp(iw_0\eta) \exp(-\eta^2/2), \tag{2.1}$$

where η is a non-dimensional time, w_0 is the non-dimensional frequency. This can be summarized as a plane wave modulated by a Gaussian. It has good frequency resolution but it comes at a cost of its time resolution, while another wavelet called the Paul wavelet has a poorer frequency resolution but it has an

increased time resolution. This allows the wavelet transform to be manipulable to the users' goal.

From this step, the continuous wavelet transform can be defined as the convolution of each data point with the scaled version of $\Psi_0(\eta)$,

$$W_n(n,s) = \sum_{n'}^{N-1} x_{n'} \Psi_0^* \left[\frac{(n'-n)\delta t}{s} \right], \tag{2.2}$$

where s is the wavelet scale, x_n is the data point at time index n, where δt is the time step and where $*$ means the complex conjugate. Thus by varying the wavelet scale and moving along the time index, it becomes possible to construct an image showing both the amplitude of any features versus the wavelet scale and how this amplitude varies with time. It should be noted that the wavelet scale will need to be transformed into frequency, but for the Morlet wavelet the wavelet scale is proportional to the frequency.

The bottom left image of Figure 2.3 shows the output of a wavelet algorithm on the artificial signal. The dark regions show an increase in the power, which shows where the periods of the signal are. The wavelet algorithm has the ability to calculate the significance of any regions of power and the black contour lines show this. The contour lines shown are for 95% significance. Further, much like the FFT, the finite length of a signal creates edge effects for the wavelet. This can be seen as the cross-hatched regions, these mark the region where the finite length of the signal affects the wavelet transform. This is called the cone of influence (COI) and it is different for each mother wavelet.

Finally, the wavelet transform allows for direct comparison of two signals. It is possible to calculate the cross-wavelet of two signals as well as the correlation and the phase difference using the wavelet transform. This fact allows the wavelet transform to be used to measure the phase difference of the cross-sectional area and total intensity signals, which is the main method used to find the phase difference. This is possible with the FFT. However, due to the localised nature of the wavelet transform, the phase difference can found as a function of frequency and time. Thus it is possible to see if the phase difference varies for that frequency which could indicate an underlying physical mechanism such as mode conversion for the observed waves. See Torrence and Compo (1998) for an overview of the wavelet transform and its applications. Further, see De Moortel *et al.* (2004) and Christopoulou *et al.* (2003) for an overview of wavelets in a solar physics context.

2.3.3 Empirical mode decomposition

Finally, we have the Empirical Mode Decomposition (EMD). As the name suggests, this method is not based off a mathematical theorem or transformation in the way that the FFT or wavelets. The algorithm will output several signals, called the residual and Intrinsic Mode Functions (IMFs). The residual is the left over signal from the algorithm and tends to contain any slow varying background trend. An IMF will generally be a simple oscillatory mode, ideally it should contain one of the frequencies within the original signal. There are two requirements in order to be considered as an IMF. Firstly, the number of extrema and zero crossings must either be equal or differ by one. Secondly, the mean value of the envelope defined by the local maxima and the envelope defined by the local minima equals zero. This means that the output from the EMD is constrained, which results in non-arbitrary signals.

The steps of the algorithm are as follows,

1. The local minima and local maxima of the input signal are found.
2. A spline fit of the minima and maxima points is computed.
3. The resulting minima and maxima curves create an envelope that encompass the signal.
4. The mean of the envelope is subtracted from the input signal and this process is repeated again. This is termed sifting.
5. The sifting stops once the stopping criterion is satisfied.
6. The resulting signal is called an IMF and is subtracted from the original signal. The leftover signal is termed the residual.
7. This process repeats itself again on the residual signal until a set number of IMFs are obtained or the residual signal contains too few extrema to spline fit.

These steps are shown in Figure 2.4. There are three comments to be made here about the algorithm. First, a local minima (maxima) point is defined if that point is smaller (larger) than its two neighbouring points. Second, are two commonly used definitions for the stopping criterion. The first one is, if the standard deviation of the sifted signals is lower than a given limit, which is typically less than 0.3, the process stops. The second one is called the S number which is, if the same signal is returned by the sifting process more than S times, this causes the process to stop. Thirdly, the overall algorithm has no method of deciding when enough IMFs have been found, so the number picked

is arbitrary, but generally the algorithm will stop before this limit is reached. This is because as the residual becomes linear with each IMF removal, the fitting algorithm will stop naturally since there is not enough extrema points to spline fit.

The resulting set of IMFs, contain the periods within the original signal, while the residual should contain any background trend. Much like the FFT, you can reverse the method as the sum of all of the IMFs and residual will return the original input signal. The EMD allows much like the cross-wavelet, the ability to find the phase difference between two signals containing the same periods. With a direct comparison of the IMFs of one signal to another, you can measure the phase difference between them and was carried out by Morton *et al.* (2011). The EMD algorithm is also very good at separating noise from a signal, which is what the first IMF generally contains.

The drawbacks for the EMD are most focused on the method, since it has no mathematical foundation like the FFT or wavelet. The most important issue for the EMD is the spline fit that creates the envelopes. The envelope fit with each iteration, starts to become very large at the edges since there is nothing to constrain it. As such, when these are subtracted from the signal, the resulting IMFs display large swings at the start and end, so these edge effects will easily affect the output. To counter-act this effect, several methods have been suggested to lessen this issue and it will generally involve adding extra extrema points on both sides to constrict the spline fit (Zeng and He, 2004). See Huang *et al.* (1998) for an detailed overview of the EMD and Terradas *et al.* (2004) for a solar physics context.

2.3.4 Multiple methods

Within this thesis, three different signal analysis methods are utilised. Overall, the main idea was to confirm the results of each analysis method. While each individual method offers the ability to find a periodicity within a signal and to compare the phase of two signals. On their own, they offer no independent verification that the found periodicity and phase is correct. But using the other methods it allows each method to be verified before any conclusions can be made. Each method has its own strengths and flaws and by using all three, it is possible to take account of any flaws. The FFT offers a snapshot interpretation of a signal, as the output is only a function of frequency. However, the wavelet and EMD offer the ability to examine how a periodic changes as a function of time as well. This allows for a more detailed interoperation than the FFT. Furthermore, the wavelet transform does not cope well with noise in the high frequency part of the spectrum and this can be seen clearly in bottom left

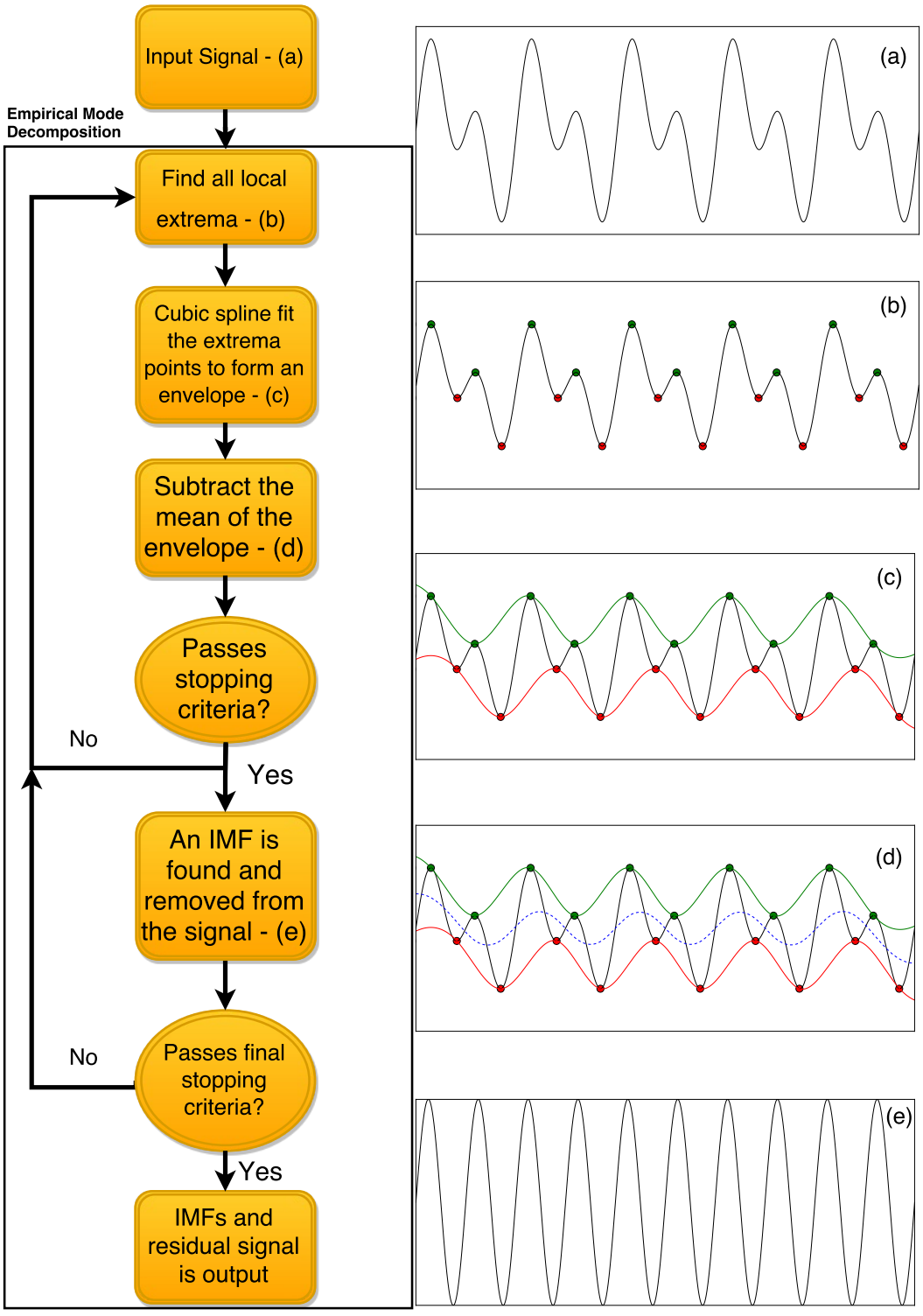

Fig. 2.4 An overview of the steps that form the Empirical Mode Decomposition (EMD) algorithm. On the left is a flow chart that summarises each step of the EMD algorithm. On the right is a graphical explanation of certain steps in the flow chart.

image in Figure 2.3. The smaller frequency component have been found by the wavelet but it is not continuous through time, while the higher frequency component has been detected less. Without the noise in the signal, or a higher signal to noise ratio, the wavelet gives a much better representation of the input signal. The output of the EMD detects both periods without an issue but it has not returned the correct amplitude due to the noise in the original signal. Thus the EMD excels for detected high frequency components over the wavelet, especially for noisy signals. The main issue with the EMD algorithm is the detection of low frequency components, as the algorithm iterates further, the edge effects can become a problem. As a result, the low frequency components in a signal can become washed out from an IMF. The wavelet does not have a problem with low frequency components, even for noisy signals. In conclusion, the combination of these three signal analysis methods allows the weakness of one method to be overcome with another and allows each result to be checked.

2.4 Area analysis

The core idea behind the work presented in this thesis is analysing the cross-sectional area of pores and sunspots. So it is vital to be able to confidently measure the cross-sectional area. The base idea is to threshold the structure and use that as a measure of its cross-sectional area. The issue is that various methods have been used in published research. While many never state exactly how they contoured a sunspot or a pore, partially due to not caring explicitly about the cross-sectional area. Previously, Morton *et al.* (2011) used a 2.5σ threshold of the mean background intensity for G-band data, here, sigma (σ) refers to the standard deviation of the background intensity. The number before sigma will be called the sigma multiplier throughout this section. More recently, Grant *et al.* (2015) used 2.2σ of the mean background intensity for their data. This was to account for the change in contrast between several different wavelength filters as this was the first multi-height analysis. Their aim was to measure the cross-sectional area of a pore from the photosphere to the lower chromosphere which is challenging topic.

What will occur in this section is an analysis on the effect of changing the sigma multiplier on the returned cross-sectional area signal. The value of sigma can appear to be arbitrary and there is an assumption that the intensity of the background photosphere has a normal distribution and as such, sigma can be used to contour these magnetic structures. To be more precise, whether different sigma values will give different periods after signal analysis or if the value of sigma once set within a certain range does not change the output is of interest. This will be discussed in this section. Furthermore, since the current

selection of ground-based solar telescopes have resolutions similar to each other and this could be the limiting factor in detecting these oscillations. As the slow MHD sausage mode affects the cross-sectional area much less than the fast MHD sausage mode, it is most likely mode to be detected in observations.

This analysis is only for ground-based data and for ion lines that sample the photosphere directly. The chromosphere lines used traditionally (Ca II and Hα line core) make resolving the fine boundaries of a sunspot or a pore very difficult. The cross-sectional area and total intensity are inherently linked on a conceptual level. Thus, it might be possible that if the intensity changes, a fake period could be introduced into the cross-sectional area. Furthermore, during ground observations the light level will change or the seeing conditions will vary, this could introduce an artificial period into the cross-sectional area and total intensity signals. Figuring out how to account for these effects will be important, however these are areas for future investigation.

2.4.1 Data

The data for this investigation comes from two instruments on the DST: IBIS and ROSA. The IBIS dataset consists of an image series of a Hα line scan. The DST was centred on a sunspot in AR 11579. The observation run was on the 30$^{\text{th}}$ of September 2012 at 15:00 UT until 15:16 UT with a cadence of 6.8 seconds. The full field of view (FOV) was 96″by 96″with a pixel size of 0.097″. The part of the line scan used here is -0.7 nm, which falls into the blue wing of the Hα line profile. This part of the line profile samples the photosphere strongly and will show Ellerman Bombs as well as Type II spicules. See Nelson and Doyle (2013) on the reduction methods for this IBIS dataset.

The ROSA dataset consists of an image series of G-band narrowband filter images. The DST was centred on a small pore cluster in AR 11683. The observation run was on the 6$^{\text{th}}$ of March 2013 at 19:27 UT till 20:02 UT with a cadence of 2.11 seconds. The full FOV was 115″by 115″with a pixel size of 0.12″. The narrowband filter means that only the line core was sampled and for G-band (430.5 nm) this corresponds to the low photosphere. See Grant *et al.* (2015) for the reduction methods for this ROSA dataset.

Both magnetic structures can be seen in Figure 2.5. The image on the left showcases the IBIS sunspot while on the right, the ROSA pore is displayed. Both images are context images and do not show the full FOV of each instrument during that observation run. Both structures are stable throughout their respective observation run.

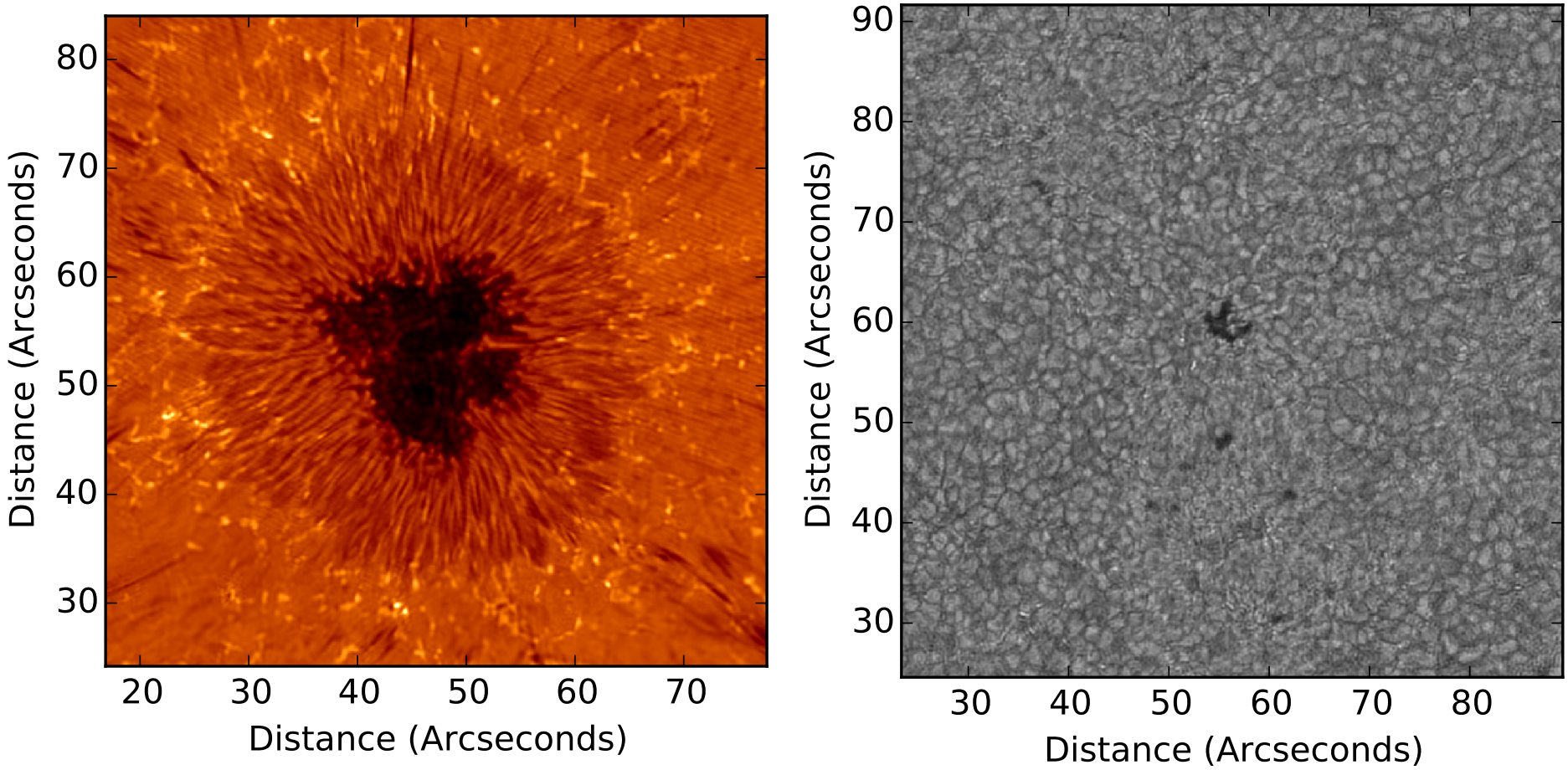

Fig. 2.5 The left figure is the cropped field of view (FOV) for IBIS. It is in the blue wing of the Hα line profile which samples the photosphere and not the chromosphere that the line core samples. The sunspot is in AR 11579 and was taken on the 30$^{\text{th}}$ of September 2012 at 15:00 UT until 15:16 UT. The right figure is of a cropped FOV for ROSA. It is the G-band narrowband filter which samples the lower photosphere. The focus is on a small pore cluster, in AR 11683 and was taken on the 6$^{\text{th}}$ of March 2013 at 19:27 UT till 20:02 UT. The pore investigated is the larger one in the middle.

2.4.2 Method

The method used to contour these structures is as follows. The starting point is to find a large region of the quiet Sun photosphere, where there is no strong magnetic features. This area is used to calculate the mean intensity and a histogram of this area should form an approximate normal distribution. The normal distribution means that the standard deviation can be used to select specific pixels within the image. As the number of standard deviations is increased, more of the data will be covered by the distribution. By limiting the pixels of interest by having a limit that is lower than say two standard deviations or higher, the pixels left over will be the darkest 5% of pixels, or the other way round would return the brightest 5% of pixels. Theoretically, the lower limit should return the pixels for sunspots and pores which are substantially darker than other features in the photosphere. By counting these pixels, this should correspond to the cross-sectional area of these magnetic structures.

Figure 2.6 shows this method applied to these datasets. The left column shows the context images of each dataset shown in Figure 2.5. However, added to these images are four contours coloured as follows: blue, green, purple and orange. Each colour represents a different sigma multiplier for the standard deviation. The sunspot and pore do not share the same range of sigma multipliers. For the sunspot the sigma multipliers are 3, 3.5, 4, 4.5 and for the pore they are 2, 2.5, 3, 3.5.

2.4.3 IBIS sunspot

The contouring for the sunspot at the lower sigma multipliers does capture small parts of the penumbra. For example at 2.5σ (which is not shown), the contour was the entire sunspot, i.e., the umbra and penumbra. The jump to 3σ (blue) curtails most of the penumbra. Once sigma is at 3.5 and 4, which correspond to the green and purple contours, the penumbra that is contoured has shrunk nearly to zero. However, it is not until we reach the largest sigma value, 4.5 which is the orange contour, that the penumbral area disappears completely. The reason for this can be seen in the right column of Figure 2.6. The top figure is of a histogram of both the background which is in yellow and the context image on the left which is in red. The background here is not a normal distribution and the reason for this is that the full FOV does not have a good area of quiet Sun photosphere. The wings of Hα show a variety of features, including Ellerman Bombs and Type II spicules, so finding an isolated region becomes harder. Furthermore, the full FOV is more limited in IBIS than ROSA or CRISP. This means that the sigma value is skewed and thus

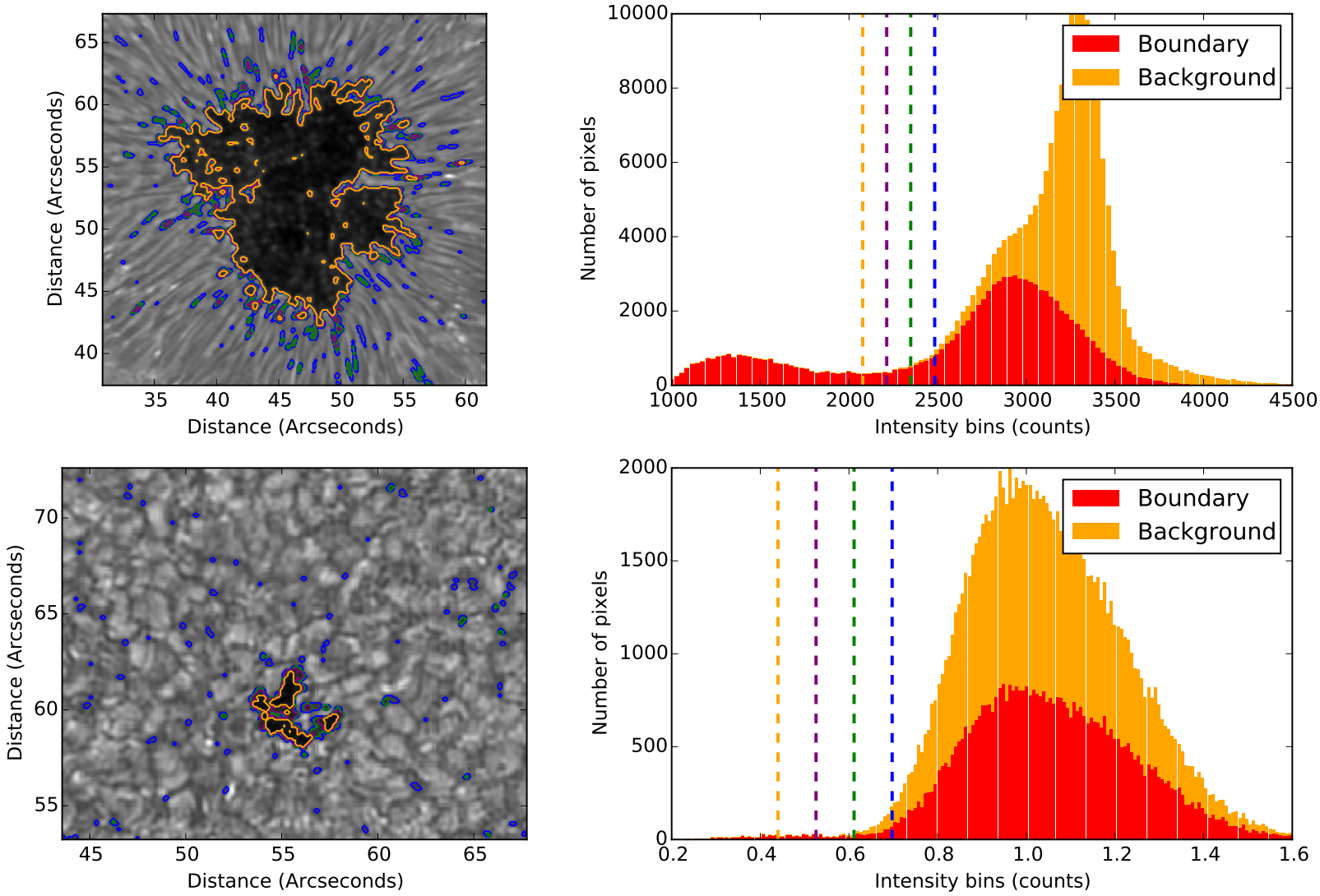

Fig. 2.6 An overview of the method used to contour magnetic structures. The left column shows context images of the datasets shown in Figure 2.5. They have the contours of the various sigma multipliers shown. The contour colours of blue, green, purple and orange correspond to 3, 3.5, 4 and 4.5 and 2, 2.5, 3 and 3.5 for the sunspot and pore respectively. The right column shows histograms of the background photosphere in yellow and of the context image shown on the left in red. The vertical lines shown display where the sigma multipliers end up on the histogram.

the sigma multiplier will have to be higher to counter act this. Finally, the sunspot histogram shows a clear difference between the penumbra and umbra. The histogram can be split into two parts, the left part contains the umbra and the right part contains the penumbra. The penumbra for this sunspot occupies a larger portion of the context image which explains why the right part of the histogram is taller, i.e., a higher count. At the intensity values between 1800 to 2300, the histogram plateaus and within this region is where the range of sigma multipliers lie. The vertical coloured lines correspond to the same colour contour lines in the context image. It is possible to claim that, as long as the sigma multiplier is in between this range, we have isolated the penumbra from the umbra. Using this as guide, it makes it easy to show that the sigma multiplier of 4.5 (orange) would be an ideal value since it gives a value in the middle of the plateau.

2.4.4 ROSA pore

The overall picture is quite different and the main reason for this is the lack of a penumbra. While there was a plateau that separated the penumbra and umbra for the sunspot, this is missing for the pore and the sigma multiplier is harder to choose directly. The sigma multipliers are lower for the pore and are 2, 2.5, 3 and 3.5. Each of these are shown on the bottom left image of Figure 2.6. These values again correspond to blue, green, purple and orange contours. The lowest multiplier contours large amounts of the background photosphere. However, all the larger multipliers contour only the pore. There are clear parts of the pore that are ignored with these higher multipliers. By looking at the histogram, a different picture emerges when compared to the sunspot. Since the pore is very small, the behaviour of the previous histogram for the sunspot does not emerge. There is no clear separation between the background and the pore, so picking a direct sigma value is more difficult when using the histogram. The background histogram also has a normal distribution unlike the IBIS sunspot. The lower limit (the blue vertical line) shows that at this value, there is still large amounts of the background quiet Sun. But, as the limit is increased, that amount drops to near zero and as such, we have very little quiet Sun within the cross-sectional area contour. Here, instead of a plateau, the histogram reveals that there is a tail. This tail corresponds to the pixel values that correspond to the pore and it can be used to pick a sigma multiplier since it tails off to much lower values than the quiet Sun histogram. The start of this tail is around 2.5σ and this gives a very good contour of the pore. That is why taking values of the threshold above 2.5σ cuts off pixels that are clearly part of the pore. The different sigma multipliers used for the

sunspot and pore are most likely due to the lack of a good background region for the sunspot in IBIS. A direct comparison of intensity counts for a sunspot and pore is difficult since the ROSA pipeline normalizes the intensity counts.

2.4.5 Discussion

Finally, it is important to see whether these different sigma multipliers give different periods within the resultant cross-sectional area signals. Figures 2.7 and 2.8 show the wavelet transform of the signals that correspond to the smallest and largest sigma multipliers used for the sunspot (3, blue and 4.5, orange) and pore (2, blue and 3.5, orange). The top row show the cross-sectional signals of these sigma multipliers and the bottom row is the resultant wavelet transforms.

The IBIS sunspot shows little change between the sigma multipliers. Since the range of sigma multipliers correspond to the plateau region, the returned cross-sectional area does not catch the penumbra, so the signal that corresponds to either one is focused heavily on the umbra and detects the periods found in the umbra. Thus, for this range of sigma multipliers, the same periods are found within this dataset. The short length of this data series means that it is impossible to find larger period oscillations, so the only periods found in this sunspot are 1 and 2 minute oscillations. This is interesting, since it should be possible to observe 3 and 5 minute oscillations but they are absent within this particular dataset.

Now, for the pore observed in ROSA. To start, it is important to note that it is a longer observation sequence. The most obvious difference here is the variation of wavelet power at periods less than 4 minutes between the two sigma multipliers. For the lowest sigma multiplier (2, blue), there is a large amount of wavelet power and most of that region is above the significance level. This image is the opposite for the largest sigma multiplier (3.5, orange). There are only two small regions of wavelet power that are within the significance level. Otherwise, the difference between these sigma multipliers is minor. These are for the larger periods that can be seen at 5 and 9 minutes. While they are under the cone of influence, they are more obvious and their associated wavelet power is larger for the smaller sigma multiplier. However it important to note that both sigma multipliers still have the same oscillation periods. The cause of this difference is that the larger sigma multiplier undersamples the pore and this has caused the large difference observed in the wavelet figure, as one might expect. However, this reveals that the difference here is still minor, it would matter most if the wavelet power was used to measure the amplitude of these oscillations.

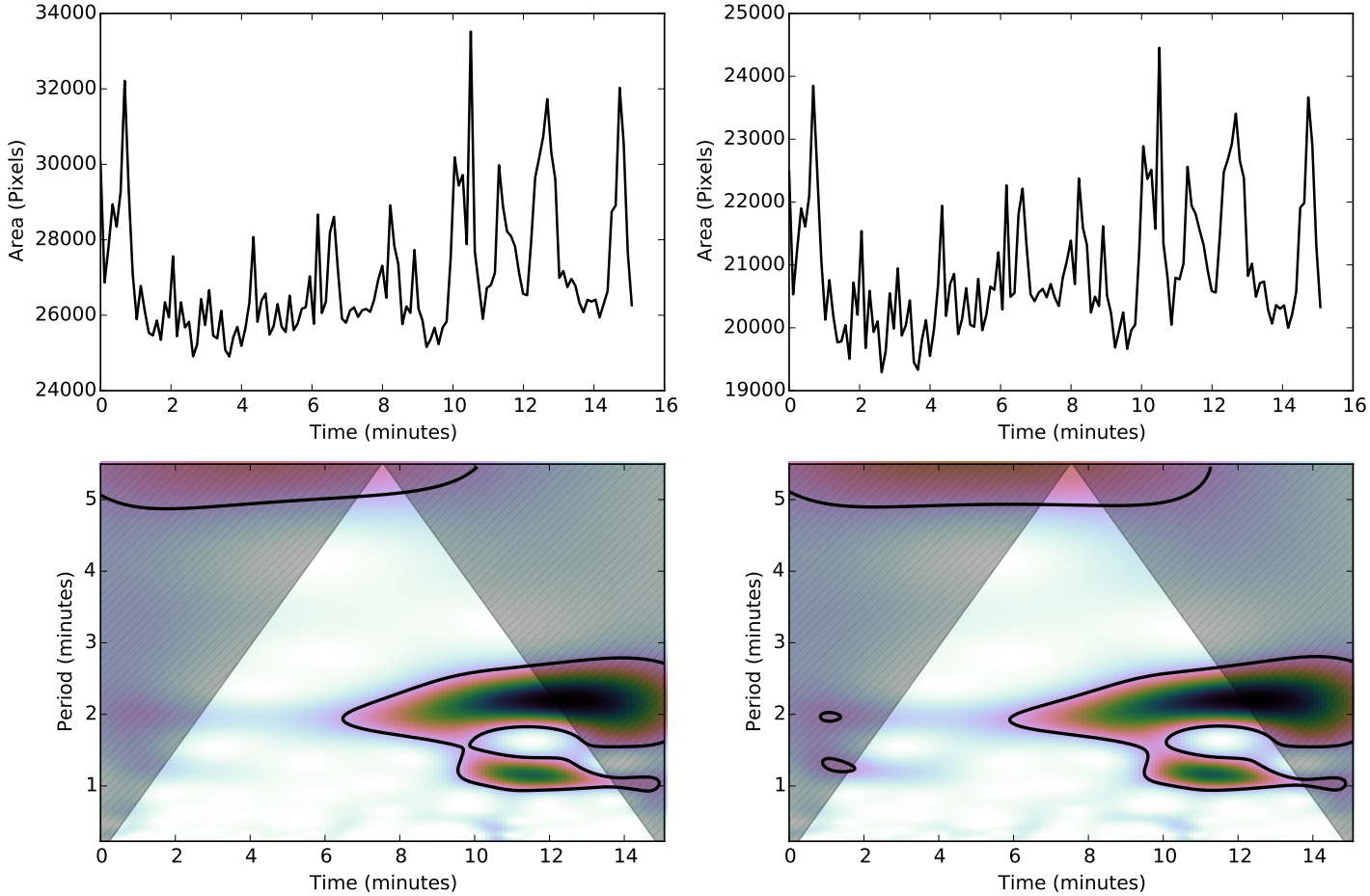

Fig. 2.7 The top row shows the cross-sectional area signals returned from a sigma multiplier of 3 and 4.5 for the IBIS sunspot. These correspond to the blue and orange contours in Figure 2.6. The bottom row shows the resultant wavelet transform of these two signals. The cross-hatch region is the cone of influence, while the black contour line is the 95% significance level. The returned wavelet transforms images show that for the IBIS sunspot, the difference in sigma multipliers cause no variation in the detected area oscillations.

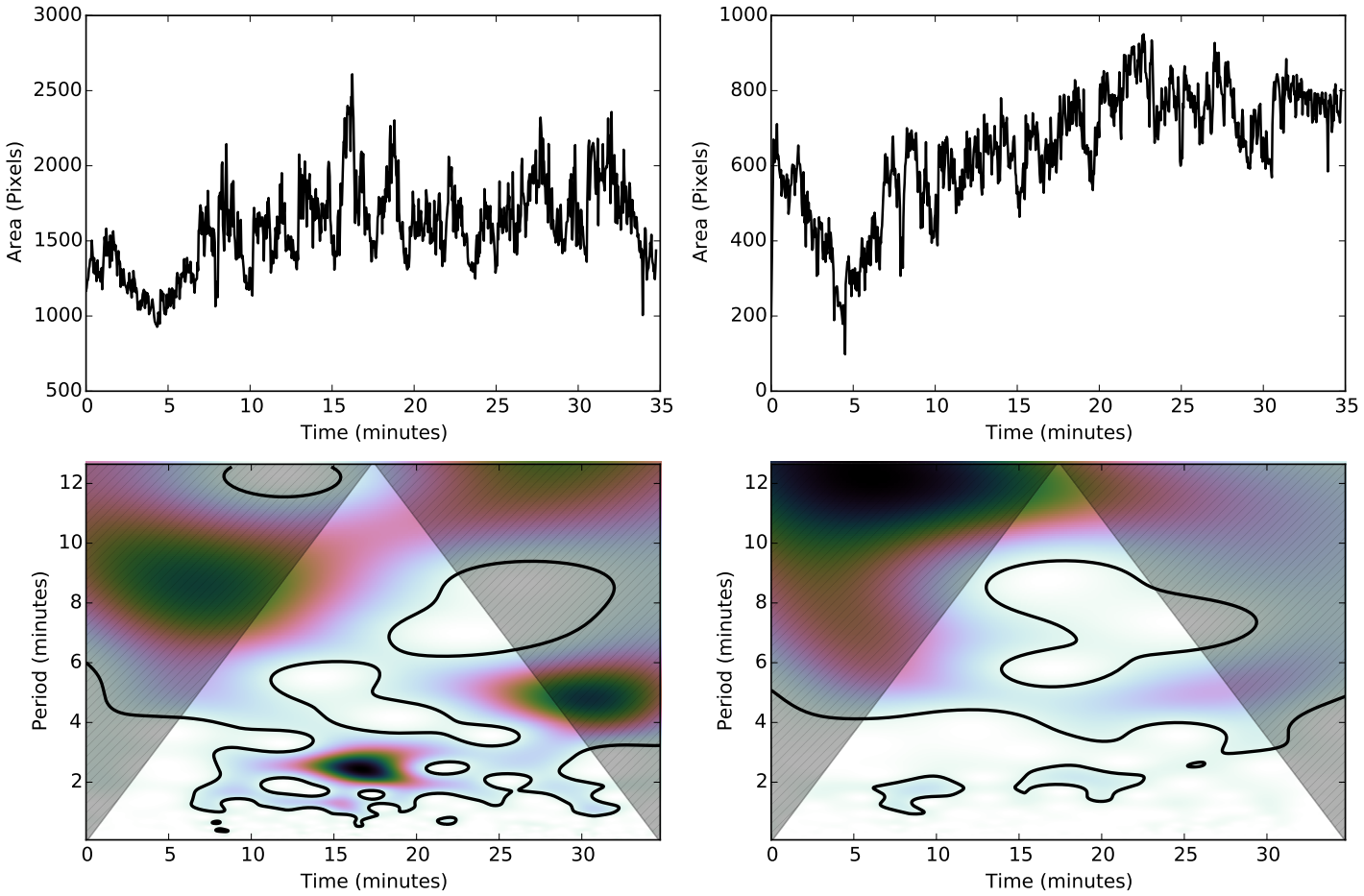

Fig. 2.8 Same as Figure 2.7 but for the ROSA pore. The lowest sigma multiplier is 2 and the largest is 3.5. These correspond to the blue and orange contours in Figure 2.6. Unlike the sunspot, there is a clear difference between the different sigma multipliers. The periods at 2 and 3 minutes are not shown in the largest case and this showcases that for pores, the sigma multiplier is very important.

Finally, ending on mode identification. Figures 2.9 and 2.10 show the cross-wavelet phase diagram between the cross-sectional and total intensity signals for the IBIS sunspot and ROSA pore, respectively. The output is in the same style as the normal wavelet, however, the colour indicates the phase difference in degrees, where blue is positive and red is negative degrees. By checking the regions where the cross-sectional and total intensity wavelets overlap, it is possible to see what the phase difference is. In this case, for both magnetic structures the phase difference is strongly in phase. The ROSA pore demonstrates a more complex image, there are more regions of out of phase behaviour that seems to change from positive to negative. However, the regions with this behaviour are smaller than one wave period and are ignored as a result. This behaviour is more common in pores than sunspots. Overall, within both these structures the oscillations can be classified as slow MHD sausage modes. It should be noted that this study does not fully cover every nuance regrading this method, it is something that is covered in Section 6.3. In conclusion, as long as the value of sigma multiplier is sound, the sigma multiplier will not vary the result.

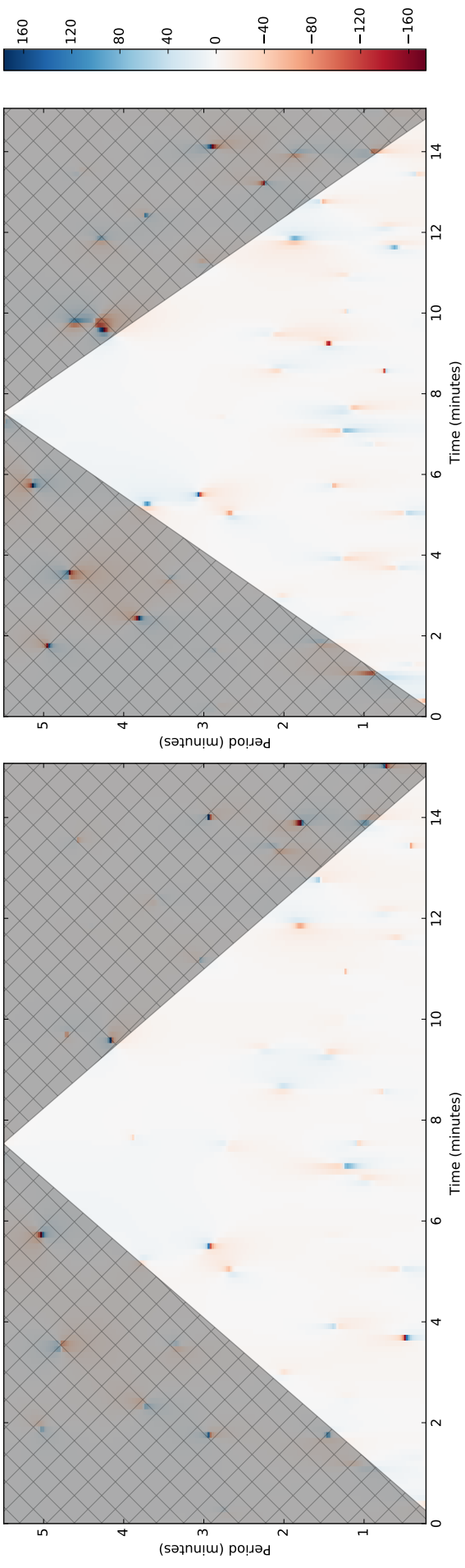

Fig. 2.9 The wavelet phase difference between the cross-sectional area and total intensity for the IBIS sunspot. The lowest sigma multiplier is 3 (left) and the largest is 4.5 (right) which correspond to the blue and orange contours in Figure 2.6. The cross-hatch region is the cone of influence. The returned phase spectrum reveals that the two signals are in phase which indicate slow MHD sausage waves. The sigma multiplier has had little effect on the output.

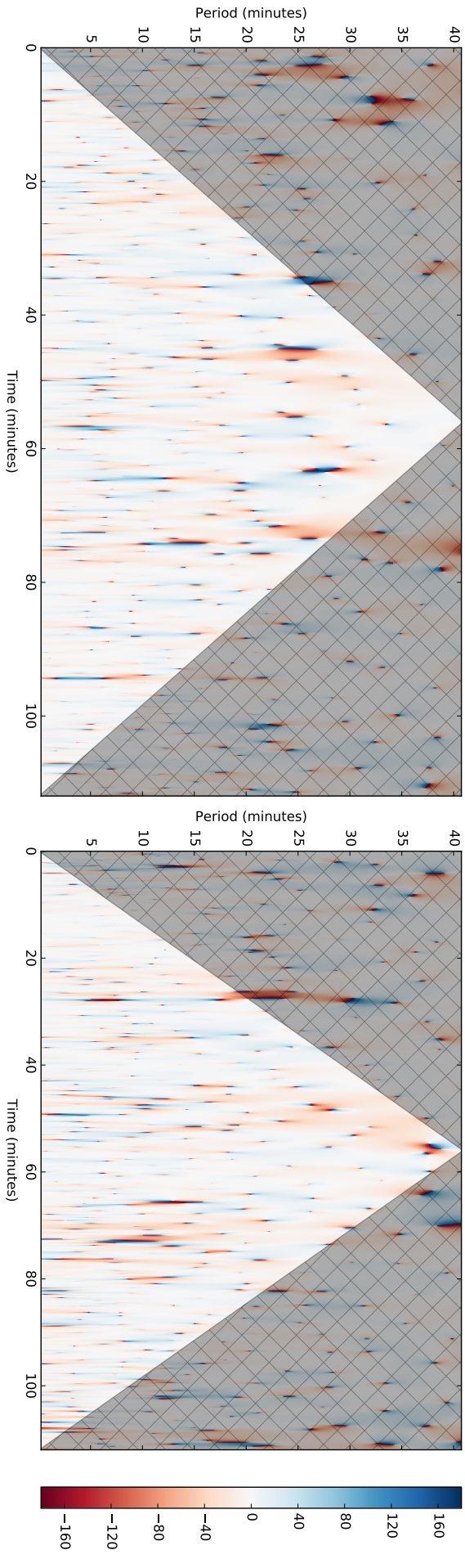

Fig. 2.10 Same as Figure 2.9 but for the ROSA pore. The lowest sigma multiplier is 2 (left) and the largest is 3.5 (right). The results here show the same behaviour as the IBIS sunspot.

Chapter 3

Analysis of Area Oscillations[1]

[1]This chapter is based on Dorotovič, I., Erdélyi, R., Freij, N., Karlovský, V. and Márquez, I., 2014, "Standing sausage waves in photospheric magnetic waveguides", *Astronomy & Astrophysics*, **563**, A12. [DOI], [ADS]. Reproduced with permission from Astronomy & Astrophysics, ESO.

3.1 Introduction

Section 1.4.2 details the background magnetohydrodynamics (MHD) theory and how to observe MHD sausage modes within magnetic flux tubes. MHD theory has been developed since the early 1970's and as such, sunspots have been intensively studied for oscillations. The commonly studied oscillatory periods in sunspots are the 3-minute and 5-minute which are seen in intensity, line-of-sight (LOS) velocity, and LOS magnetic field which were detailed in Chapter 1. Moving away from LOS oscillations required more understanding of MHD wave theory in cylindrical flux tubes. It was not until recently that MHD theory had been extended to understand axisymmetric.

The MHD sausage mode is of interest here, because the sausage mode is a compressible, symmetric perturbation around the axis of a flux tube that causes density perturbations that can be identified in intensity images (Fujimura and Tsuneta, 2009). Furthermore, because the wave will either compress or expand the flux tube, the magnetic field will also show signs of oscillations. This mode may come in two forms in terms of phase speed classification: the slow mode (often also called the longitudinal mode), which generally has a phase speed close to the characteristic tube speed and, the fast mode which has a phase speed close to the external sound speed. One of the main differences between the two modes is the phase relationship between appropriate MHD quantities which allows them to be differentiated. In this case, the fast sausage mode has an out of phase relationship between the cross-sectional area and total intensity, while the slow sausage mode has an in phase relationship. The technique that was applied to obtain these phase relationships are covered by, Fujimura and Tsuneta (2009), Moreels and Van Doorsselaere (2013), and Moreels *et al.* (2013).

Sausage modes have been observed in pores before. Dorotovič *et al.* (2008) observed a pore for 11 hours and reported periodicities in the range of 20-70 minutes. These oscillations were consequently interpreted as linear low-frequency slow sausage waves. Morton *et al.* (2011) used the Rapid Oscillations in the Solar Atmosphere (ROSA) instrument to also identify linear sausage oscillations in a pore. However, determining whether the oscillations were slow or fast proved to be difficult.

The source and driving mechanism(s) of these MHD sausage modes have been very difficult to identify. Numerical simulations of a flux tube rooted in the photosphere, which is buffeted by a wide range of coherent sub-photospheric drivers, is one method for identifying the potential source of MHD sausage waves. These drivers can either be horizontal or vertical, single, or paired or else a power spectrum, with varying phase differences (see e.g. Fedun *et al.*,

2011a,b; Khomenko *et al.*, 2008; Malins and Erdélyi, 2007; Vigeesh *et al.*, 2012). To understand these MHD sausage oscillations, it is necessary to firstly see if it is possible to identify the signature within solar magnetic waveguides situated in the lower solar atmosphere.

3.2 Data collection and method of analysis

Three time series of images with high angular resolution have been chosen here in order to demonstrate the identification of MHD sausage waves. The images were taken in the G-band (430.5 nm), which samples the low photosphere. This line forms deep in the photosphere and is optically thick which means that the intensity is a function of density and temperature and other factors.

The images were acquired using:

1. The Swedish Vacuum Solar Telescope (SVST) situated on La Palma in the Canary Islands. Scharmer *et al.* (1985) provides a detailed description of the features of the SVST. The images were taken on 7 July 1999. The sunspot is in Active Region (AR) NOAA 8620. The observing duration is 133 minutes with a cadence time of 25 seconds. The field of view (FOV) covers an area of 33, 600 km by 54, 600 km (1 pixel $\approx$ 60 km). Bonet *et al.* (2005) gives a detailed analysis of this sunspot. A context image is the left-handed image of Figure 3.1.

2. The Dutch Open Telescope (DOT) is also situated on La Palma in the Canary Islands. Two series of imaging data sequences were taken using this telescope. A detailed guide of the features of the DOT is provided by Rutten *et al.* (2004). The first series of data were taken on 13 July 2005, and the sunspot is in the AR NOAA 10789. The region slowly decayed, and this sunspot led a small group of other magnetic structures. The observing length is 165 minutes and has a cadence time of 30 seconds. The second set of data taken on 15 October 2008 is of a large pore with a light-bridge which is about 15 pixels (750 km) wide in AR NOAA 11005. The duration of the observing run is 66 minutes and has a cadence time of 20 seconds. Both DOT image sequences cover an area of 50, 000 km by 45, 000 km, where the maximum spatial resolution is 0.2" ($\approx$ 140 km). Typical context images are the middle and right-handed panels of Figure 3.1.

To obtain information relating to the cross-sectional area of these waveguides, a strict and consistent definition of the cross-sectional area is required. The definition is that each pixel with a value of less than 3σ of the median

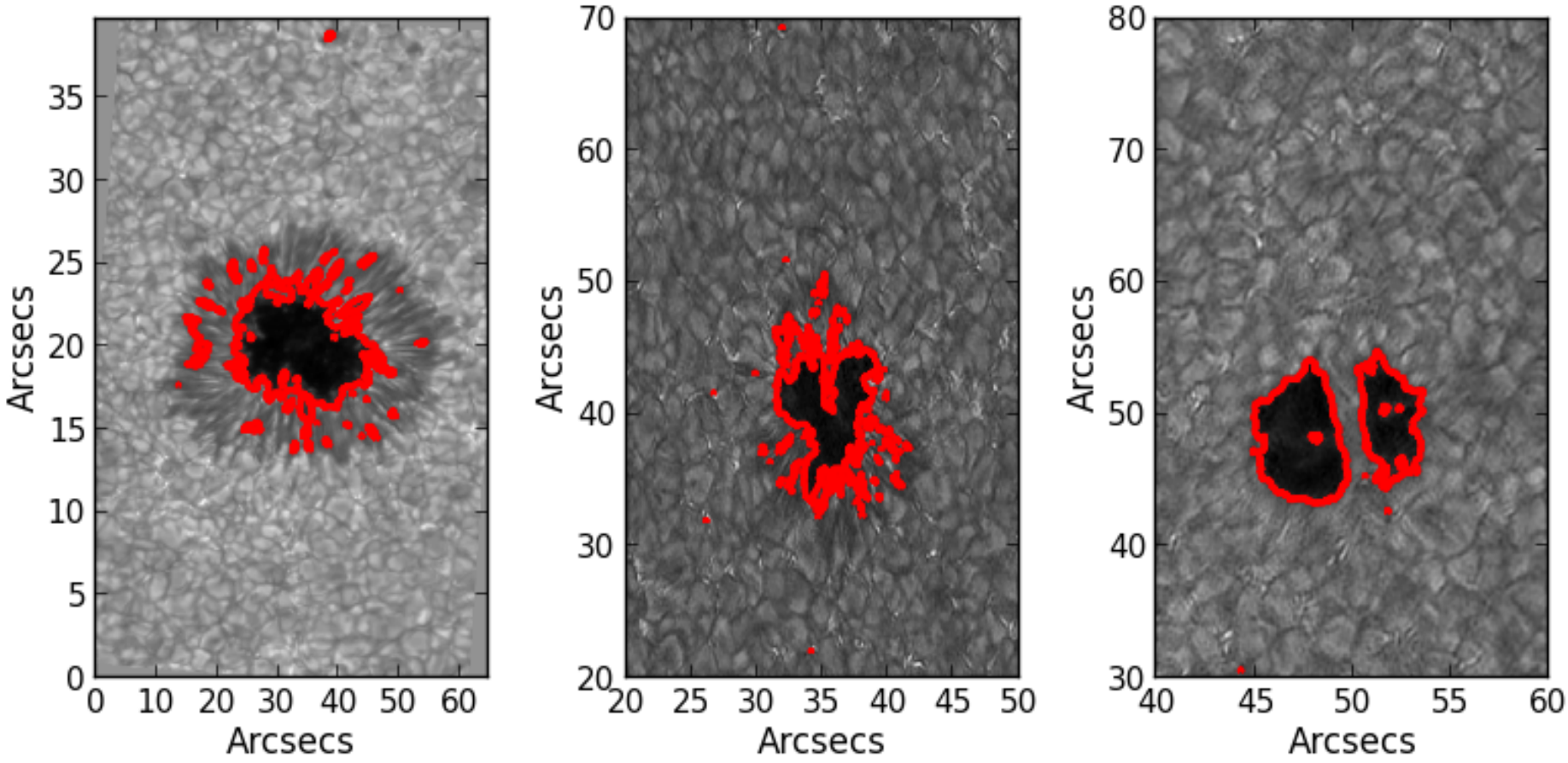

Fig. 3.1 An overview of the magnetic waveguides used for this analysis. *(left)* The 1999 sunspot observed with the SVST with an average umbral area of 19,650 pixels (50 M km^2). *(middle)* The 2005 sunspot observed with the DOT with an average umbral area of 12,943 pixels (32 M km^2). *(right)* The 2008 pore observed with the DOT with an average area of 10971 pixels (27 M km ^{2}), the light-bridge that separates the pore can be seen. Furthermore, these structures were seen near the disk centre, so there is little to no LOS effect. The red line shows the thresholding technique applied to each waveguide at the start of each data series.

background intensity is counted as part of the waveguide. The background is defined as an area of the image where there are no magnetic features. This may appear to be an arbitrary definition; however, a histogram of the background intensity reveals a Gaussian distribution, and when adding the area around and including the waveguide, there is significant peak on the lower end of the Gaussian distribution curve around 3σ or higher. Thus, we have a 99% confidence that the area is of the structure and not of the background.

Figure 3.1 shows each waveguide at the start of the time series, where the red contour line represents the regions of cross-sectional area found. The definition is accurate, but, it does include some non-waveguide pixels. In order to reduce this factor, a bounding box is taken as close to the magnetic waveguides as possible without covering up umbral pixels. The total intensity was determined by summing over the intensity of each pixel found in the waveguide. These waveguides are not static structures as they slowly changed in size during the observing period. This background trend has to be removed for it not to mask any weak oscillatory signatures. The main reason for detrending the signal is that wavelet is computed using the Fast Fourier Transform (FFT), the signal has to have a zero mean, otherwise artefacts are introduced into the output. The detrending was accomplished by a non-linear regression fit and the consistency of the results was compared to subtracting the residue from an Empirical Mode Decomposition (EMD) analysis (which is explained in Chapter 2 and below). The residue is the data that remains after the EMD procedure has extracted as many signals as possible and it provides a very good approximation of the background trend.

The resulting reduced data series were then analysed with a wavelet tool in order to extract any periods of oscillation present within these signals. The algorithm used is an adapted version of the IDL wavelet routine developed by Torrence and Compo (1998). The standard Morlet wavelet, which is a plane sine wave with an amplitude modulated by a Gaussian function, was chosen for its suitable frequency resolution. The white cross-hatched area marks the cone of influence (COI), where edge effects of the wavelet structure affect the wavelet transform, and anything inside the COI is discarded. The white dashed line contour shows the confidence level of 95%. The wavelet method is very susceptible to noise at short periods and at times may not identify the true power of short periods.

Beyond this, the data representing the size and intensity has also been analysed using EMD, which decomposes the time series into a finite number of intrinsic mode functions (IMFs). IMFs are essentially narrowband-filtered time series, with each IMF containing one or two periods that exist in the original signal. The EMD technique was first proposed by Huang *et al.* (1998) and

offers some benefits over more traditional methods of analysis, such as wavelets or Fourier transforms (see Chapter 2). However, one drawback is that it is very prone to error with regards to long periods. The problems described above regarding the wavelet and EMD mean that the two complement each other. Furthermore, periods that appear in the wavelet *just* below the confidence level, but appear strongly in the EMD process, is a good indication that a period is not spurious. At this stage, we rely on wavelet and EMD analyses, as is customary in solar physics. For more detail on the signal analysis, see Chapter 2.

3.3 Results and discussion

3.3.1 LOS, circularity, and evolution of the waveguide

Several points need to be clarified for the data presented here before the full analysis. Firstly, there are LOS issues, Cooper *et al.* (2003a,b) have investigated how the LOS angle affects various aspects of observing coronal loops in a 2D model. Overall they found that for the slow sausage MHD wave, for a range of angles from $\pi/6$ to $\pi/3$, the observed intensity decreases as the LOS angle increases. Secondly, the larger angles lengthened the *observed period* of the wave. While the objects here are not coronal loops, the LOS angle still matters and should behave similarly. The LOS angles in all three cases were less than 30° thereby limiting any relevant effects of LOS.

Sunspots or pores are not fully circular and can have arbitrary shapes. The effects of a non-circular shape have been studied by, for example, Ruderman (2003), Morton and Erdélyi (2009), and Morton and Ruderman (2011). While they do not account for the very complicated and real structure of the sunspots and pores observed here, they still offer an adequate insight. Current theory suggests the shape will have a minor effect on the oscillations unless it has a significant deviation from circularity. Likewise, the structure of each waveguide undergoes a minor change during the observation campaign, limiting any effects from large-scale structural change, as can be seen in Figure 3.2.

3.3.2 MHD theory for phase relations

Treatment of the MHD equations makes it possible to determine phase relations between various physical quantities for propagating and standing MHD waves. This has been summarised briefly by Goedbloed and Poedts (2004) and also applied by Fujimura and Tsuneta (2009). The latter find that the phase relation for the slow MHD wave with regards to cross-sectional area and density is in

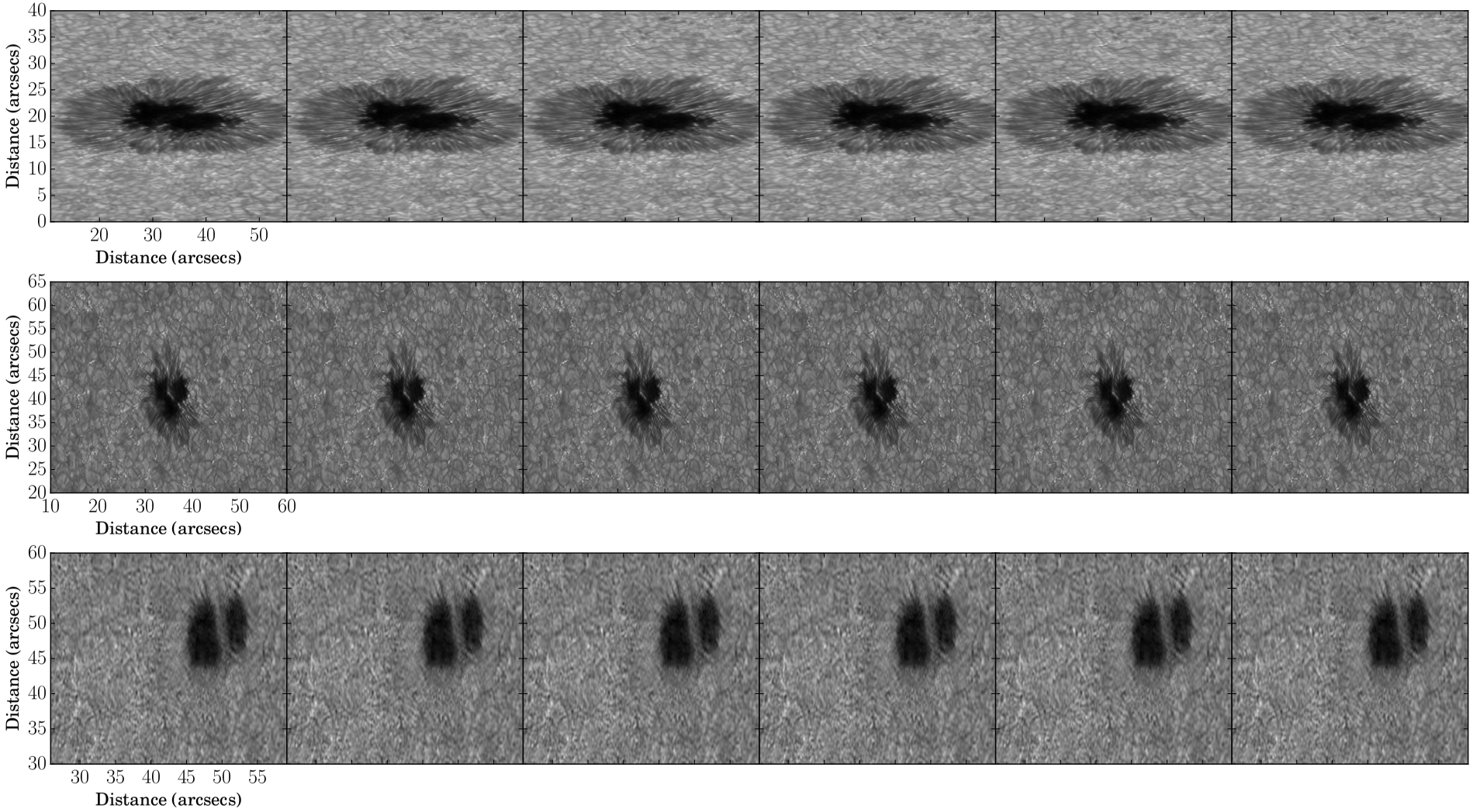

Fig. 3.2 The three waveguides seen through six different parts of their corresponding observation sequence. The image sequence has time increasing from left to right. The first row is the 1999 sunspot, the middle row the 2005 sunspot, and the last row the 2008 pore.

phase regardless of whether the wave is propagating or standing. More recently, Moreels and Van Doorsselaere (2013) have expanded on this idea, taking factors into account such as LOS, which were neglected earlier, but also expanding the theory to cover fast MHD sausage waves. The phase relation for the magnetic field to the cross-sectional area is in phase when assuming that the magnetic field is frozen into the plasma.

Supplementary information from other perturbation phase relations, such as the LOS velocity and the LOS magnetic field, allows one to determine whether the observed MHD wave is slow or fast. In summary, the slow MHD sausage mode shows in phase behaviour between intensity and area perturbations, while the fast sausage mode shows out of phase behaviour. Before progressing, we need to address the opacity effect on MHD wave perturbations. This is relevant, since intensity fluctuations can be due to the change of the optical depth along the LOS, which has the same phase difference as the fast MHD sausage wave and as a result is indistinguishable without further information (Fujimura and Tsuneta, 2009).

Recently, Moreels *et al.* (2013) have analytically determined the phase difference between the cross-sectional area and the total intensity perturbations for both the slow and fast MHD sausage modes. Note that any mention of the area means the cross-sectional area from here on in and the intensity means the total intensity. They find that, for both the slow body and surface MHD wave, the behaviour is in phase, while for the fast surface wave, the behaviour is out of phase. This result means that it is possible to approximately separate slow and fast sausage waves without the use of other observable variables. Their results will be used here to distinguish between slow and fast MHD sausage modes.

3.3.3 Sunspot, 7 July 1999 , AR 8620

Figure 3.3 shows the wavelet analysis of the 1999 sunspot's area and intensity data. There are four confidently identified periods that exist in the area wavelet with 95% certainty; 4, 7, 16, and 32 minutes. The 32-minute period is found over a wide range of the time series, with some of its power inside the COI. However, most is outside the COI. The 16-minute period is strongly localised at 50 to 120 minutes of the data series, starts at 18 minutes, and slowly increases and stabilises at 14 minutes. There is a third and fourth period at four and seven minutes that just reach the significance level and appear sporadically during the time series.

The intensity wavelet shows three distinct periods of oscillations above the confidence level: 4, 16, and 36.5 minutes. The 36.5-minute period has a corre-

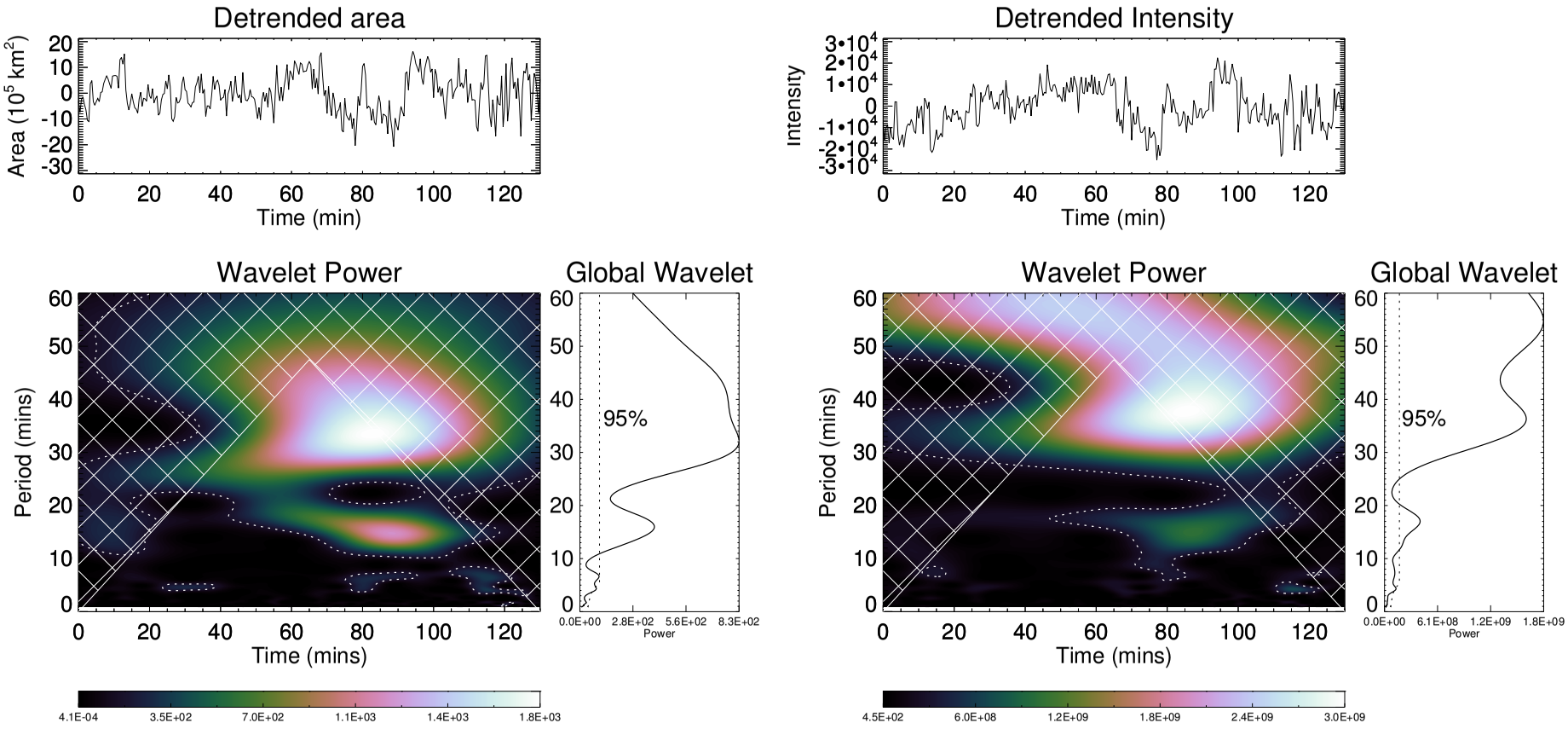

Fig. 3.3 *(left image)* Evolution of the area of the 1999 sunspot. *(right image)* The same as the left image but for the total intensity of the 1999 sunspot. *(upper panel)* The signal that is analysed. *(lower panel)* The wavelet power spectrum for a white noise background, the cone of influence is marked as a cross-hatched area where edge effects become important and the contour lines show the 95% confidence level. *(lower right panel)* Global (integrated in time) wavelet power spectrum, where the dashed line shows the 95% confidence limit.

sponding area wavelet oscillation at 32 minutes. While the 16-minute oscillation corresponds to the 16-minute oscillation found in the area. Furthermore, the 16-minute period starts with very concentrated power and does not display the same period change as the area oscillation does. Finally, the four-minute period also corresponds to an oscillation found in the area but is also sporadic in its appearance.

It is safe to say that these oscillations are caused by sausage waves. The reason is that in linear ideal MHD theory, the sausage wave is the only MHD wave capable of changing the area of the flux tube that is observed on disk (see e.g. Cooper *et al.*, 2003a; Wang, 2004). Without the ability to directly compare the phase difference of the area to the intensity, great caution needs to be exercised to determine with confidence whether the perturbations are fast or slow. A wavelet phase diagram reveals regions (where the wavelet coherence is high and the period is ≤ 20 minutes) to be either out of phase or in phase, but a clear image of constant phase difference does not appear. This might be due to mode conversion occurring in the sunspot, since the G-band samples a region where the plasma-$\beta \approx 1$ in a magnetic structure (Gary, 2001). When the period is ≥ 20 minutes, the only area of high coherence is located around 30 minutes and found to be nearly out of phase, which hints that there might be a fast surface sausage wave. However, only two full wave periods are outside the COI, which is due to the total length of the data series. This behaviour indicates that for short periods, a mixture of fast surface and slow MHD sausage waves are present while for the long period, it is purely a fast surface MHD sausage wave.

Figure 3.4 shows the computed IMFs for the 1999 sunspot dataset. The IMFs show the periods of oscillations identified using the EMD algorithm. IMFs which show irrelevant periods, or the residual signal which are ignored. In general, the higher order IMFs tend to show longer periods and, as such, contain fewer wave periods, which makes phase identification less reliable. Four IMF overlays are shown, and IMFs with similar periods to the wavelet plots have been overlaid in order to aid comparison for each dataset.

Four IMFs directly coincide with the wavelet period that reveal both area and intensity perturbations. IMF c_3 displays the four-minute period where major regions of in phase behaviour can be seen; however, both side shows one or two wave periods of out of phase behaviour. IMF c_4 exhibits a period of seven minutes. The picture here is more muddled as an extra period is present in the intensity, namely 11 minutes, making phase identification harder for the seven-minute period. Where the IMFs coincide with the same period, namely at the start of the time series, the phase difference is approximately 45 degrees, which the author have no theoretical explanation for. IMF c_5 displays

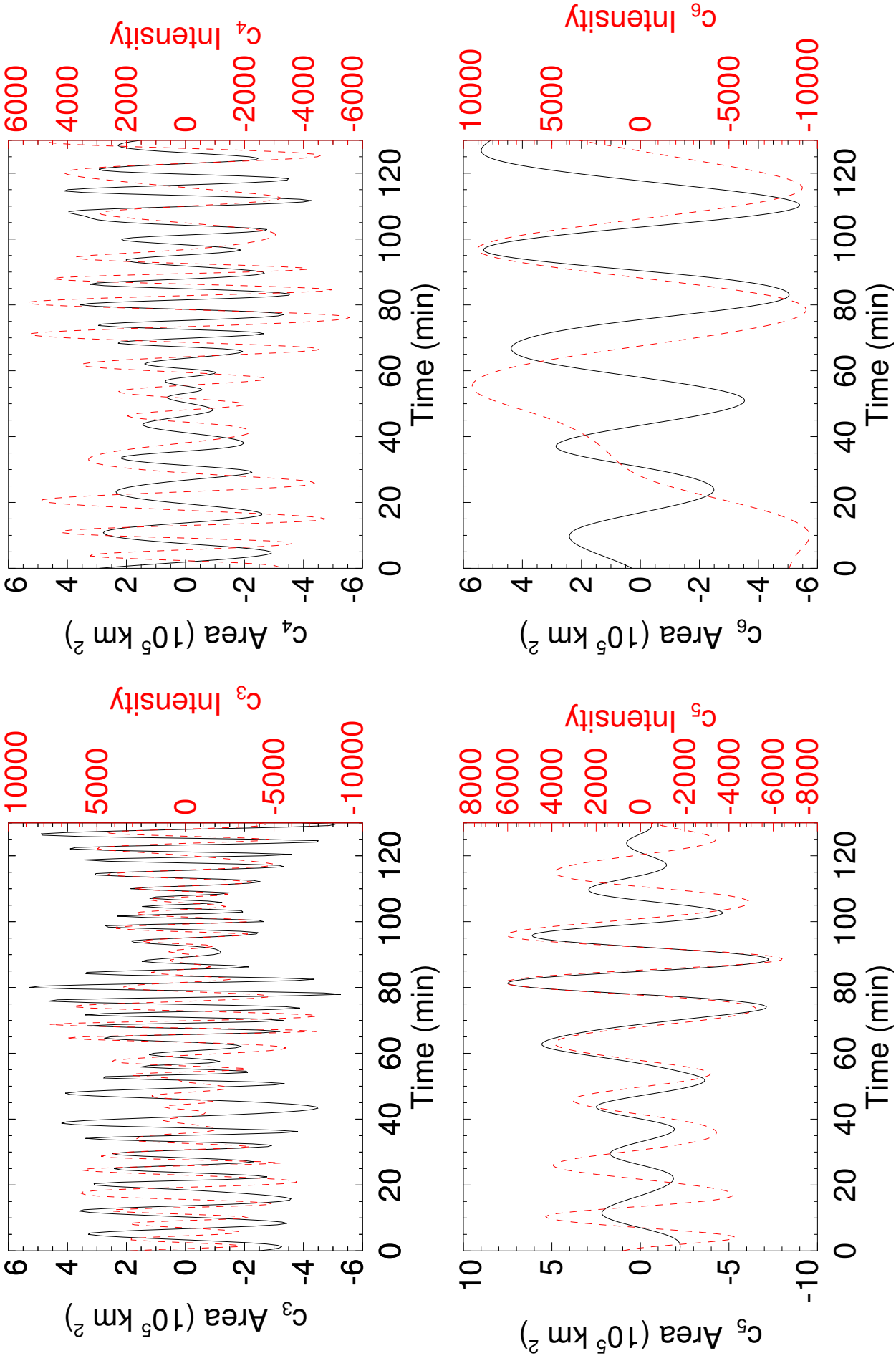

Fig. 3.4 The IMFs of the evolution of the area (red) and intensity (black) for the 1999 sunspot, over-plotted to aid comparison. Generally after the 6th IMF, higher IMFs lack a sufficient number of wave periods, which makes it difficult and less reliable to obtain an accurate period.

a 16-minute period, with in phase behaviour. Finally, IMF c_6 contains the 32-minute period. This period does not fully match the period seen in the intensity, but also one of the edge effects of the EMD process can be seen in the intensity signal. Near the end of the time series, the two IMFs overlap with the same period with an in phase behaviour. In summary, the EMD process shows that the major behaviour is in phase, indicating the existence of a slow sausage mode. Also the regions of changing phase difference at lower periods indicates the potential existence of a fast surface mode as the phase difference matches. The reason for the wave being restricted as only a surface mode is due to current theory that suggests that the fast body mode is not supported in photospheric flux tubes (Moreels and Van Doorsselaere, 2013; Moreels *et al.*, 2013). However, the last IMF does not agree with the wavelet phase due to the artefact from the EMD process.

It was possible to approximately separate the penumbra from the umbra and investigate its area for oscillations. However, the penumbra is a highly dynamic object and this makes the area estimation reasonably uncertain. There seem to be four periods that exist at 95 % certainty: 5, 9, 15, and 25. The three shorter periods (5, 9, and 15 minutes) closely correspond to the 4, 7, and 16-minute oscillations in the umbra; they could be a continuation of these umbral periods that became up-shifted as they enter the less compact structure of the penumbra. While the 25-minute period does not directly correspond to an observed area oscillation. The wavelet phase analysis shows large regions of out of phase behaviour where the period is either below ten minutes or above 20 minutes. This behaviour is a mixed collection of fast surface and slow sausage modes, with regions moving from one phase difference to another after three or more wave periods.

3.3.4 Sunspot, 13 July 2005, AR 10789

Figure 3.5 shows the wavelet analysis of the 2005 sunspot area and intensity in AR 10789. There are four periods that exist at 95% confidence level: 4, 7.5, 11, and 16.5 minutes. Each period has a region of high power in the wavelet, with the lower periods appearing nearer the end of the time series. The corresponding intensity wavelet reveals that there are three periods of 4, 7.5, and 10.5 minute oscillations; however, the 16.5-minute oscillation is present but is a very weak signal. The cross-wavelet phase indicates that these oscillations are in phase. There are no major regions of out of phase behaviour.

Figure 3.6 shows the IMFs for the area and the intensity of the sunspot data in AR 10789. In this case, each period is found by the EMD process. IMF c_2, IMF c_3, IMF c_4, and IMF c_5 correspond to the 4, 7.5, 11, and 16.5-minute

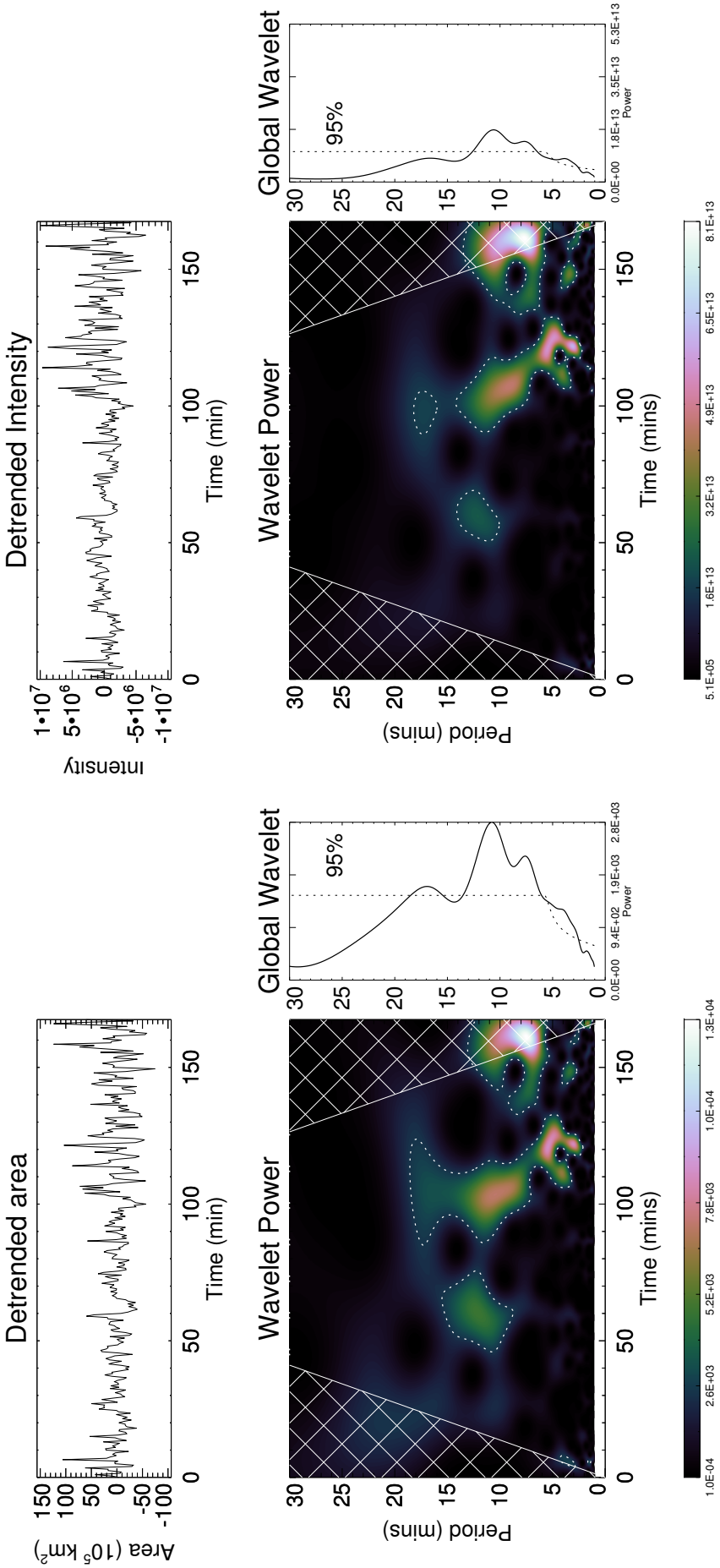

Fig. 3.5 Same as Figure 3.3 but for the sunspot in AR 10789 observed in 2005.

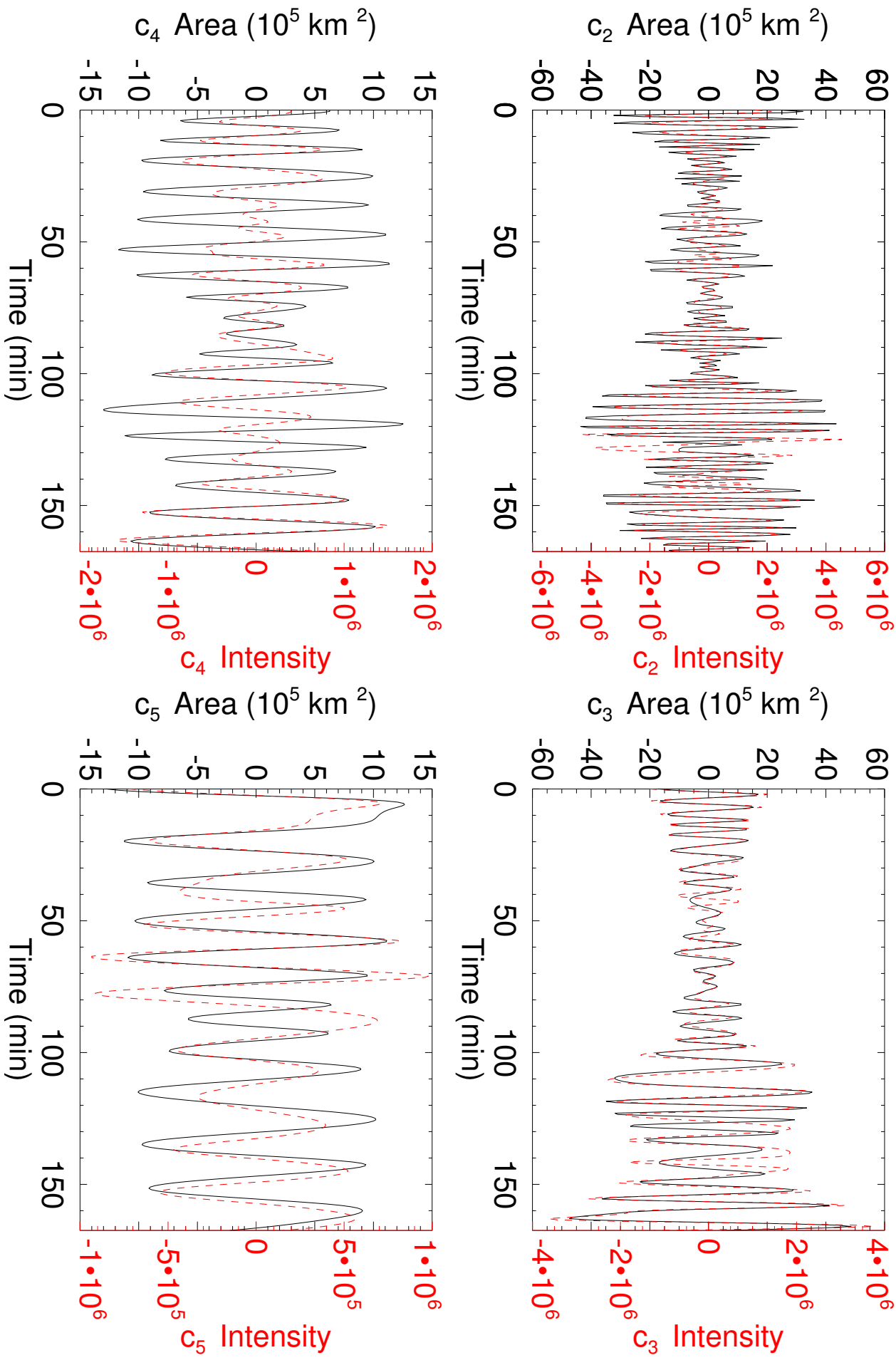

Fig. 3.6 Same as Figure 3.4 but for the sunspot in AR 10789 observed in 2005.

oscillation periods, respectively. IMF c_2 displays extensive in phase behaviour throughout the time series, which is a strong indication of the slow sausage MHD wave at a period not too dissimilar to the global p-mode oscillation. The region of interest is within the time interval of 90 to 130 minutes for IMF c_4, where the wavelet has these oscillations. The IMF shows clear in phase behaviour in this time interval. The overall phase relation between the area and intensity indicates the presence of slow sausage waves.

3.3.5 Pore, 15 October 2008

Figure 3.7 shows the wavelet analysis of the pore with a light-bridge. There are three periods that exist at 95 % confidence level: 4.5, 8.5, and 14.5 minutes. The large part of the power of the period of 14-15 minutes is inside the COI; however, the period appears in the EMD analysis and has a large portion of power outside the COI and thus has not been ignored for this analysis. The three periods are seen in both area and intensity data when the wavelet analyses are cross-correlated. The power for these two periods is concentrated in the time interval of 20 to 60 minutes. The cross-wavelet analysis shows that the overlapping time span is somewhat smaller, at about 30 to 50 minutes. Furthermore, the wavelet power for each period runs parallel to each other throughout the time series, and they appear at the same time and seem to fade away at a similar time as well.

Figure 3.8 shows the IMFs for the area with intensity over-plotted. In this case, IMF c_3 indicates a period of 4.5 minutes and IMF c_4 has a characteristic period of 8.5 minutes, and this applies to both the area and intensity IMFs. IMF c_3 reveals that the phase relation is in phase for the majority of the time series. IMF c_4 reveals large regions of roughly in phase behaviour but with, again, a 45-degree phase difference. Not shown is the comparison of IMF c_4 and IMF c_5 for the area and intensity, respectively. At the end of the time series for both, there is a mixture of in phase behaviour but also with the intensity signal leading the area signal for the 8.5 minute oscillation. IMF c_5 and IMF c_6 for the area and intensity, respectively, show a period of 14.5 minutes. There is a region of near out of phase behaviour before this then turns into 45-degree phase difference with the area leading the intensity perturbations. Consistently, there are occurrences of unexplainable phase differences that require new MHD theory in order to explain.

The easiest way to confirm the linearity of waves is to compare the amplitude of the oscillations to the characteristic scale of the structure. In all three cases studied here, the oscillation amplitudes are around 10% or less of the total area, which indicates that these oscillations are linear. Furthermore, the amplitude of

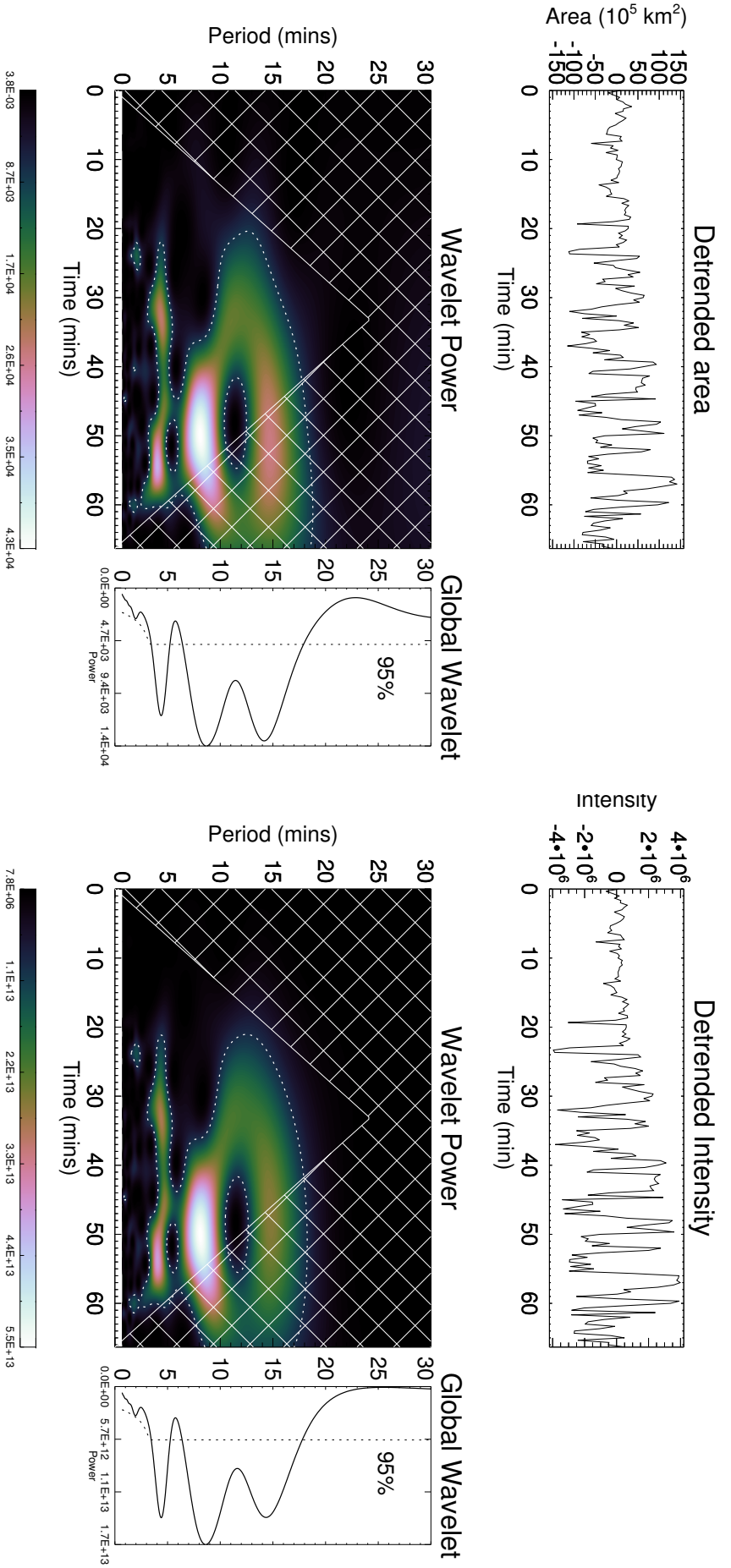

Fig. 3.7 Same as Figure 3.3 but for the pore in AR 11005 observed in 2008.

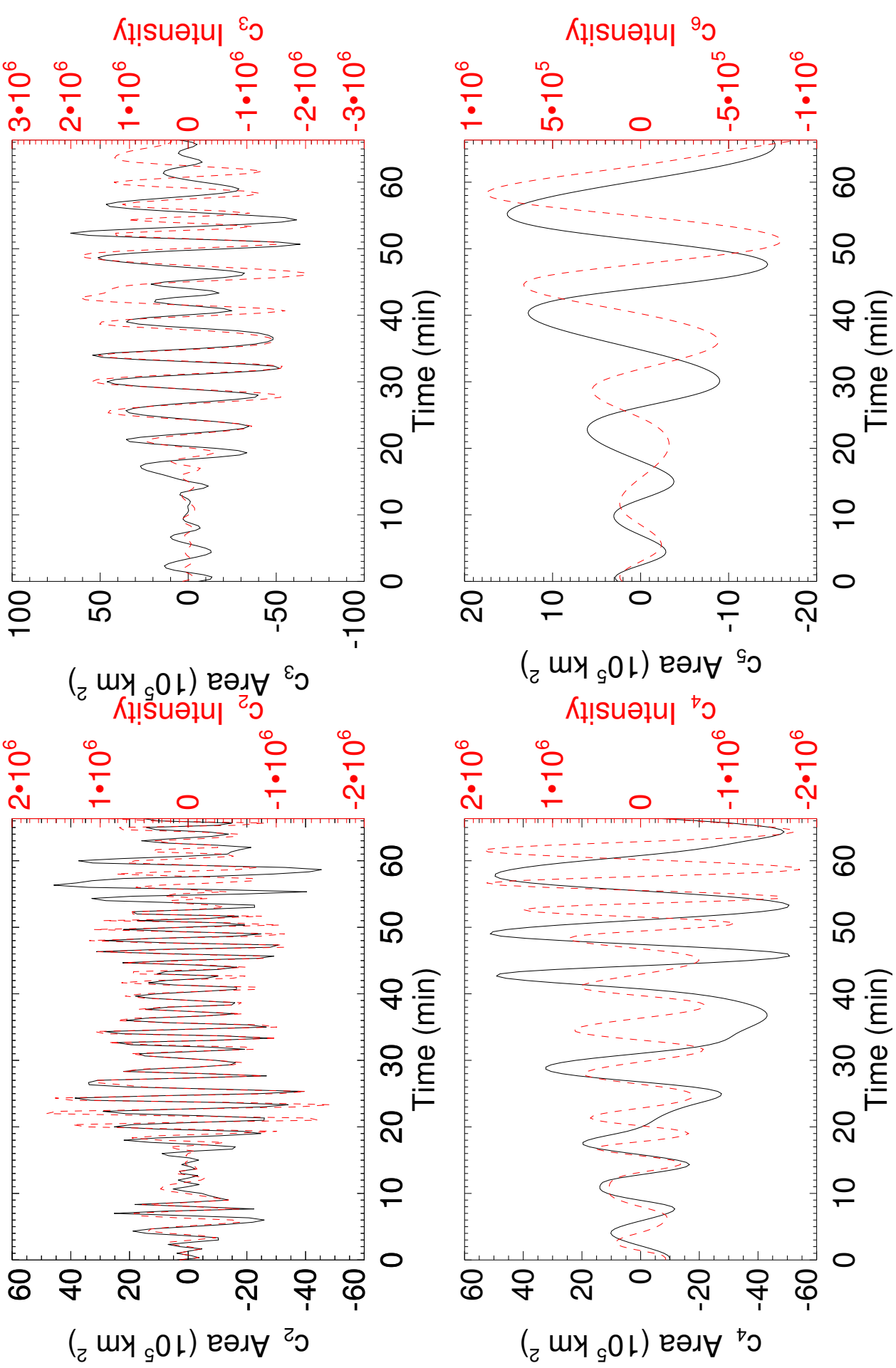

Fig. 3.8 Same as Figure 3.4 but for the pore in AR 11005 observed in 2008.

Dataset		Period (Mins)	Ratio (P_1/P_i)	Expected Ratio
Sunspot 1999	P_1	32 ± 2.5	-	-
	P_2	16 ± 1.5	2 ± 0.2	2
	P_3	7 ± 0.5	4.6 ± 0.3	3
	P_4	4 ± 0.5	8 ± 0.5	4
Sunspot 2005	P_1	16.5 ± 1.5	-	-
	P_2	11 ± 0.5	1.5 ± 0.2	2
	P_3	7.5 ± 0.5	2.2 ± 0.2	3
	P_4	4 ± 0.5	4.2 ± 0.6	4
Pore 2008	P_1	14.5 ± 0.5	-	-
	P_2	8.5 ± 0.5	1.7 ± 0.1	2
	P_3	4.5 ± 0.5	3.2 ± 0.2	3

Table 3.1 The periods of oscillations that are found in the area of the waveguides that exist at 95% confidence level.

the oscillation in the last two cases is by and large the same, so the amplitude has scaled with the size of the structure. However, for the 1999 sunspot, the amplitude of the oscillation is an order of a magnitude less. Whether this is due to the large size of the sunspot or the very stable nature during the observation window needs to be investigated in future work.

3.3.6 Standing harmonics

Basic MHD theory interpretation allows sunspots and pores to be described as vertical cylindrical flux tubes, with the base bounded in the photosphere and the top bounded at the transition region due to the sharp gradients in the plasma properties at these locations. Taking this further, an ideal flux tube is assumed here. The plasma density and magnetic field are homogeneous within the flux tube. This means that the standing harmonics of such flux tubes are the MHD equivalent to the harmonics in an closed-ended compressible air pipe, where the ratio of the harmonic periods is given by $P_1/P_2 = 2$, $P_1/P_3 = 3$, and so forth. This only applies in the long-wavelength or thin-tube approximation. Using harmonic ratios to carry out magneto-seismology has been used, for example, by Andries *et al.* (2005a,b) who researched the effects of longitudinal density stratification on kink oscillations and resonantly damped kink oscillations, while Luna-Cardozo *et al.* (2012) studied longitudinal density effects and loop expansion on the slow sausage MHD wave. Luna-Cardozo *et al.* (2012) found that specific density profiles in lower atmospheric flux tubes could increase or decrease the value of the period ratio. The author is unaware of any work that gives the changes to further harmonic ratios, so the assumption that the amount of deviation from the canonical value for the period ratio (P_1/P_2) is the same for other period ratios; e.g., P_1/P_3 or higher is used.

We now summarise the observed findings. Table 3.1 contains the periods of oscillations found in all three magnetic waveguides. There are four periods found for the 1999 sunspot. The second period of 16 minutes gives a period ratio (P_1/P_2) of 2 ± 0.2, which is exactly the same as the expected value of a uniform waveguide with a canonical value of 2. The next period ratio is 4.6 ± 0.3. Here, the change from canonical value is substantial if this is indeed the third period, which should be around 10.6 minutes, unless the effect on the harmonic ratio increases with each successive ratio. The last period is difficult to incorporate into the harmonic standpoint, and it is most likely that the four-minute period is due the global p-mode.

For the 2005 sunspot in AR 10789, there is a clearer picture of potential harmonics. The first period is 16.5 minutes and the second period is 11 minutes, which gives a ratio of 1.5 ± 0.2, and the third period of 7.5 minutes gives a ratio of 2.2 ± 0.3. The period ratio is modified downwards in a consistent manner as the harmonic number increases and give a strong indication of of standing waves in this magnetic waveguide. As was the case for the 1999 sunspot, the period at four minutes has a period ratio that does not fit into this harmonic viewpoint and is most likely due to the global p-mode instead. The ideal theory can not accommodate this period ratio, improved theory will be required.

For the 2008 pore of AR 11005, the picture is more muddled by the shorter time series. Taking the 15-minute period to be the first harmonic, the ratio is 1.7 ± 0.1 for the 8.5-minute period, very similar to both first-period ratios of the previous sunspots. The third period is again very close to the period of the global p-mode and does not fit into the harmonic viewpoint.

The main conclusion to take away from this data analysis at this point is that the simple homogeneous flux tube model cannot fully account for these ratios. However, this simple model seems to be robust enough to give a good first insight. The most likely reasons for deviation from the canonical period ratio value are, firstly, that sunspots and pores (just like most lower atmospheric magnetic structures) expand with height, causing magnetic stratification (Luna-Cardozo *et al.*, 2012; Verth and Erdélyi, 2008), and secondly, that the Sun's gravity causes density stratification (Andries *et al.*, 2009). These two effects will either increase or decrease the period ratio of the harmonics depending on the chosen density or magnetic profile (see Luna-Cardozo *et al.* (2012) for a detailed analysis in the context of slow sausage oscillations or see Erdélyi *et al.* (2013) for kink modes). In addition, these magnetic structures are rarely purely cylindrical, but can be elliptical (or arbitrary) in shape (see Morton and Erdélyi, 2009; Ruderman and Erdélyi, 2009) and in most cases are non-axially symmetric. Also, in some cases the flux tube is more suitably described as

closed-ended at the photosphere and open-ended at the transition region, which would remove the even harmonics.

3.4 Conclusions

In this chapter we have investigated three magnetic waveguides with the objective of detecting MHD sausage waves and determining whether they are slow or fast, propagating or standing. Based on the results presented here, we confidently interpreted the observed periodic changes in the cross-sectional area of these flux tubes, which are manifested as a pore and two sunspot waveguide structures, as strong indication of the existence of linear slow and fast surface sausage MHD oscillations. Using wavelet analysis, we found several oscillations and interpreted them as MHD waves in the photosphere with periods ranging from 4 to 32 minutes. Employing complementary EMD analysis has allowed the detected MHD modes to be identified as a combination of *fast surface sausage* and *slow sausage* modes, thanks to the phase difference of the area and intensity. It is very likely that these oscillations are *standing harmonics* supported in a flux tube. The period ratio ($P_1/P_{i=2,3}$) of these oscillations indicates strongly that they are part of a group of standing harmonics in a flux tube that is non-homogeneous and bound by the photosphere and the transition region.

Chapter 4

Slow MHD sausage waves within small-scale photospheric magnetic structures.[1]

[1]This chapter is based on Freij, N., Dorotovič, I., Morton, R. J., Ruderman, M. S., Karlovský, V. and Erdélyi, R., 2016, "On the Properties of Slow MHD Sausage Waves within Small-scale Photospheric Magnetic Structures", *The Astrophysical Journal*, **817**, 44. [DOI], [ADS], [arXiv:1509.08680 [astro-ph.SR]]. Reproduced with permission from AAS

4.1 Introduction

Improvements in space- and ground-based solar observations have permitted the detection and analysis of small-scale magnetic waveguide structures in the Sun's lower atmosphere. One such structure is a pore; a magnetic concentration with a diameter that ranges from 0.5 to 6 Mm with magnetic fields of 1-3 kG that typically last for less than a day (Simon and Weiss, 1970). pores are highly dynamic objects due to the constant buffeting from the surrounding granulation in the photosphere. A collection of flows and oscillations have been observed within and around pores (Balthasar, 1999; Dorotovič *et al.*, 2002, 2014; Freij *et al.*, 2014; Hirzberger *et al.*, 2002; Jess *et al.*, 2015; Moreels *et al.*, 2015a; Roudier *et al.*, 2002; Solanki, 2003). The major apparent difference between a sunspot and a pore is the lack of a penumbra which is a region of strong and often very inclined magnetic field that surrounds the umbra.

It is important to understand which magnetohydrodynamic (MHD) waves or oscillatory modes can be supported in magnetic flux tubes in the present context. The reason for this is two-fold: it clarifies the observational signatures of each mode, and clarifies whether or not that mode will manifest given the conditions of the local plasma. Furthermore, absorption of the global acoustic p-mode, and flux tube expansion will induce a myriad of MHD waves. Roberts (2006) investigated how the slow mode may be extracted elegantly from the governing MHD equations, considering the special case of a vertical uniform magnetic field in a vertically stratified medium. The approach may, in principle, be generalized with non-uniform magnetic fields (Luna-Cardozo *et al.*, 2012) and, by taking into account non-linearity, background flows and dissipative effects. However, as we will show below, a first useful insight still can be made within the framework of ideal linear MHD applied to a static background.

It is very difficult to directly (or often even indirectly) measure the background physical parameters (plasma-β or density, for example) of localised solar structures. For the magnetic field, the most common method is to measure the Stokes profiles of element lines in the lower solar atmosphere and then perform Stokes inversion in order to determine the magnetic field vectors. More recently, the development of solar magneto-seismology (SMS) has allowed the estimation of the local plasma properties which are generally impossible to measure directly (Andries *et al.*, 2009; Ruderman and Erdélyi, 2009). While, this technique has been used for many years in the solar corona, only recently has it been applied to the lower solar atmosphere. For example, Fujimura and Tsuneta (2009) accomplished this by observing and identifying wave behaviour in lower solar structures and interpreting the observed waves as standing MHD waves. A recent review of the lower solar atmospheric application of MHD

waves is given by, e.g. Banerjee *et al.* (2007) and Jess *et al.* (2015) and partially by Mathioudakis *et al.* (2013) in the context of Alfvén waves.

Extensive numerical modelling of wave propagation in small-scale flux tubes has been undertaken by Fedun *et al.* (2011a,b); Hasan and van Ballegooijen (2008); Kato *et al.* (2011); Khomenko *et al.* (2008); Mumford *et al.* (2015); Shelyag *et al.* (2011); Vigeesh *et al.* (2012); Wedemeyer-Böhm *et al.* (2012). These models are of localised magnetic flux tubes and the effect of vertical, horizontal or torsional coherent (sub) photospheric drivers mimicking plasma motion at (beneath) the solar surface on these flux tubes. It was found that the generation of slow and fast MHD modes or the Alfvén mode depended on the exact driver used, as well as the fact that extensive mode conversion take place within these flux tubes.

Vögler *et al.* (2005) and Cameron *et al.* (2007), using the MURaM code, simulated larger scale magnetic structures, including pores, to build up a detailed picture of the physical parameters (density, pressure and temperature) as well as flows in and around these structures, which has good observational agreement.

Dorotovič *et al.* (2008) observed the evolution of a pore's area for 11 hours in the sunspot group NOAA 7519 (see Dorotovič *et al.*, 2002; Sobotka *et al.*, 1997a). They reported that the periodicities of the detected perturbations were in the range of 12-97 minutes and were interpreted as slow magnetoacoustic-gravity sausage MHD waves. Morton *et al.* (2011), using the Rapid Oscillations in the Solar Atmosphere (ROSA) instrument installed on the Dunn Solar Telecope (DST), also detected sausage oscillations in a solar pore. The lack of Doppler velocity data made it difficult to conclude whether the waves were propagating or standing. The oscillatory phenomena were identified using a relatively new technique (at least to the solar community) known as Empirical Mode Decomposition (EMD). The EMD process decomposes a time series into Intrinsic Mode Functions (IMFs) that contain the intrinsic periods of the time series. Each IMF contains a different timescale that exist in the original time series (see Terradas *et al.*, 2004). This technique was first proposed by Huang *et al.* (1998) and offers certain benefits over more traditional methods of period analysis, such as wavelets or Fourier transforms.

Dorotovič *et al.* (2014) observed several large magnetic structures and analysed the change in time of the cross-sectional area and total intensity of these structures. Phase relations between the cross-sectional area and total intensity have been investigated by e.g., Moreels and Van Doorsselaere (2013) and Moreels *et al.* (2013). The phase difference that was observed is 0°, i.e., in phase, which matches the phase relation for slow MHD sausage waves. Furthermore, these magnetic structures were able to support several oscillations

with periods that were not to dissimilar to standing mode harmonics in an ideal case. Grant *et al.* (2015) observed a pore within Active Region NOAA 11683, using high-resolution scans of multiple heights of the solar atmosphere using ROSA and the Interferometric Bidimensional Spectrometer (IBIS) on the DST. They showed that sausage modes were present in all the observed layers that were damped whilst they propagated into the higher levels of solar atmosphere. The estimated energy flux suggests that sausage modes could contribute to the heating of the chromosphere.

Standing waves are expected to exist in the lower solar atmosphere that is bounded by the photosphere and transition region (Leibacher *et al.*, 1982; Mein and Mein, 1976). Numerical models also predict this behaviour (Erdélyi *et al.*, 2007; Malins and Erdélyi, 2007; Zhugzhda and Dzhalilov, 1982). Standing waves have been potentially seen in the lower solar atmosphere; using the Hinode space-borne instrument suite, Fujimura and Tsuneta (2009) observed pores and inter-granular magnetic structures, finding perturbations in the magnetic field, velocity and intensity. The phase difference between these quantities gave an unclear picture as to what form of standing waves these oscillations were. Standing slow MHD waves have been detected in coronal loops with NASA's Solar and Heliospheric Observatory (SOHO) and Transition Region and Coronal Explorer (TRACE, for reviews see, e.g., De Moortel and Nakariakov, 2012; Wang, 2011) and transverse (kink) oscillations have been detected in coronal loops (e.g Aschwanden *et al.*, 1999; O'Shea *et al.*, 2007; Taroyan *et al.*, 2005; Verth *et al.*, 2008, for a review see Andries *et al.*, 2009; Ruderman and Erdélyi, 2009). The harmonics of a standing wave have potentially been seen in flare loops using ULTRACAM (e.g., Mathioudakis *et al.*, 2006). Fleck and Deubner (1989) also reported the observation of standing waves in the lower solar chromosphere by measuring the brightness and velocity oscillations in Ca II lines.

In this article, we exploit phase relations between the area and intensity of two pores in order to identify the wave mode of the observed oscillations. This information, combined with the methods of SMS allows us to determine several key properties of these oscillations and of the magnetic structures themselves. Section 4.2 details the observational data, its reduction and the analysis method. Section 4.3 discusses the theory of the applicable MHD wave identification as well as the SMS equations used to estimate the properties of the observed oscillations. Section 4.4 contains the results of the data analysis while Sect. 4.5 summarises.

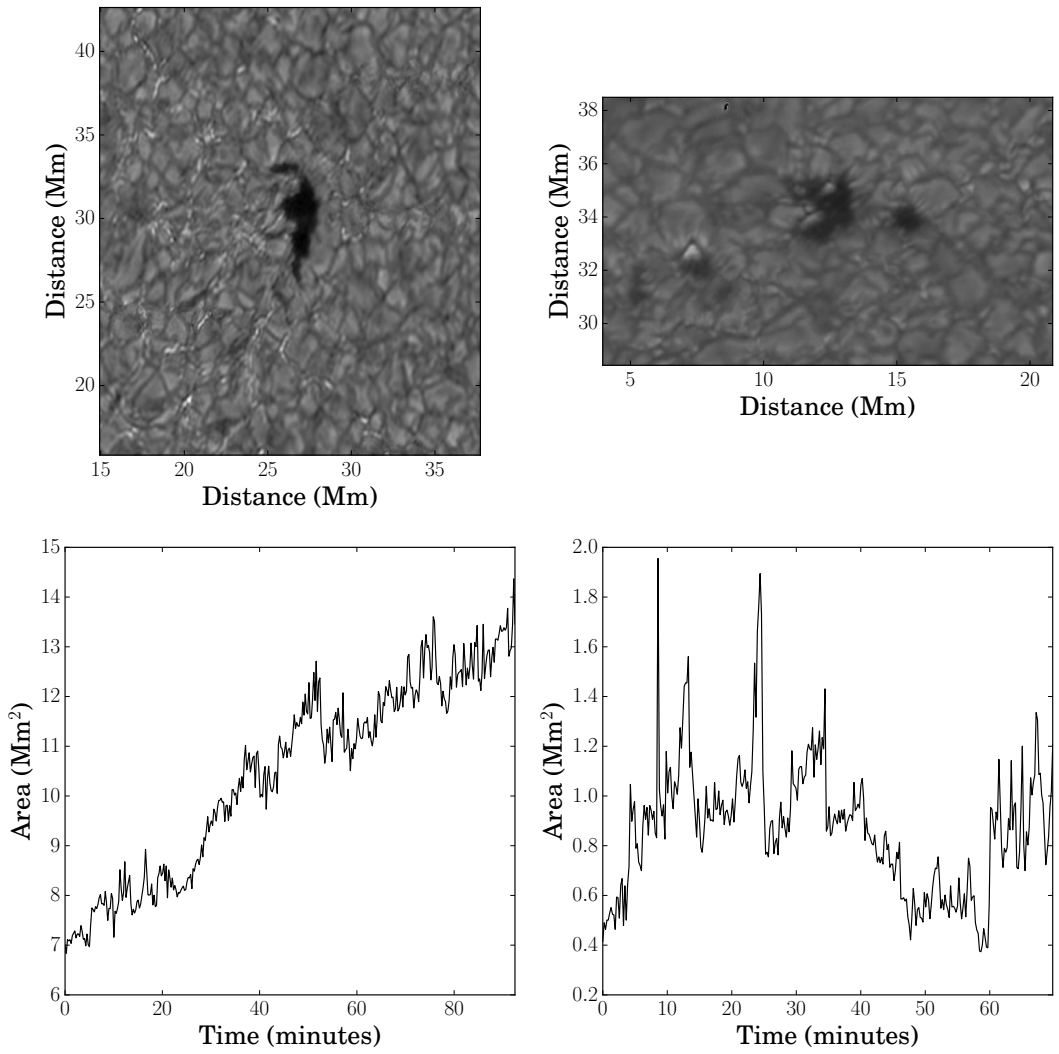

Fig. 4.1 The left column displays the pore observed by the DOT while the right column is the pore observed by the DST/ROSA. The pores at the start of the observation sequence (*Upper panels*). The original (trended) cross-sectional time series for each pore throughout the observation sequence. (*Lower panels*).

4.2 Data collection and method of analysis

Two high-resolution datasets are investigated within this article. The first dataset was acquired using the Dutch Open Telescope (DOT) (Rutten *et al.*, 2004), located on La Palma in the Canary Islands. The data were taken on 12th August 2007 with a G-band (430.5 nm) filter which samples the low photosphere and has a formation height of around 250 km above the solar surface. The observation started at 08:12 UTC and lasted for 92 minutes with a cadence of 15 seconds with a total field-of-view (FOV) of 60 Mm by 40.75 Mm. The DOT is able to achieve high spatial (0.071″ per pixel) resolution, due to the DOT reduction pipeline. It comes at a cost of temporal cadence which is decreased to 30 seconds as data reduction uses speckle reconstruction (Keller

and von der Luehe, 1992). Note, that the DOT does not have an adaptive optics system.

The second dataset was obtained on the 22nd August 2008 with the Rapid Oscillations in the Solar Atmosphere (ROSA) imaging system situated at the Dunn Solar Telescope (see Jess *et al.* 2010 for details on experimental setup and data reduction techniques). Observation started at 15:24 UTC, and data were taken using a 417 nm bandpass filter with a width of 0.5 nm. The 417 nm spectral line corresponds to the blue continuum that samples the lower photosphere and the formation height of the filter wavelength corresponds to around 250 km above the solar surface. It should be noted that this is an average formation height. This is because the contributions to the line are from a wide range of heights and the lines also form at different heights depending on the plasma properties (Uitenbroek and Tritschler, 2006).

ROSA has the ability for high spatial (0.069″ per pixel) and temporal (0.2 s) resolutions. After processing through the ROSA pipeline the cadence was reduced to 12.8 s to improve image quality via speckle reconstruction (Wöger *et al.*, 2008). To ensure alignment between frames, the broadband time series was Fourier co-registered and de-stretched (Jess *et al.*, 2007). Count rates for intensity are normalised by the ROSA pipeline.

The methodology of this analysis follows the method that was also applied by Morton *et al.* (2011) and Dorotovič *et al.* (2014). The area of the pore is determined by summing the pixels that have intensity values that are less than 3σ of the median background intensity, which is a large quiet-Sun region. This method contours the pore area well, but not perfectly, as the intensity between the pore and the background granulation is not a hard boundary. The top row of Figure 4.1 shows the pores at the start of the observation sequence, by DOT and ROSA, respectively. Furthermore, the output from the area analysis is shown in the bottom row for both pores. A strong linear trend can be observed for the DOT pore. The intensity time series was determined by the total intensity of all the pixels within the pore. To search for periodic phenomena in the time series, two data analysis methods were used: wavelets and EMD. The wavelet analysis employs an algorithm that is a modified version of the tool developed by Torrence and Compo (1998). The standard Morlet wavelet, which is a plane sine wave with the amplitude modulated by a Gaussian function, was chosen due to its high resolution in the frequency domain. The EMD code employed here is the one used by Terradas *et al.* (2004). First, we de-trended each time series by linear regression followed by wavelet analysis to determine the periodicity of the oscillations as a function of time. Second, cross-wavelet is applied to calculate the phase difference between the area and intensity series as a function of time. Although it is possible to obtain a better visual picture

of the phase relation between the two signals by using EMD, the results agreed with the cross-wavelet analysis when checked.

4.3 MHD wave theory

4.3.1 The sausage mode

We aim to identify MHD sausage modes, so, it is important to have a theoretical understanding of these modes. Assume that a pore is modelled adequately by a cylindrical waveguide with a straight background magnetic field, i.e., $\mathbf{B}_0 = B_0\hat{\mathbf{z}}$. We note that, for reasons of clarity, in the following discussion the theory does not take gravitational effects on wave propagation into account. However, the influence of gravity may be important for wave propagation in pores, especially at the photospheric level where the predicted scale height is comparable to the wavelengths of observed oscillations. Therefore we should be cautious with the interpretations. The velocity perturbation is denoted as $\mathbf{v}_1 = (v_r, v_\theta, v_z)$. From the theory of ideal linear MHD waves in cylindrical waveguides, for the $m = 0$ modes (here, m is the azimuthal wavenumber) i.e., for axisymmetric perturbations, the equations determining v_r and v_z decouple from the governing equation of v_θ. Hence, we will have magnetoacoustic modes described by v_r and v_z and the torsional Alfvén mode is described by v_θ. We are interested in the slow magnetoacoustic mode in this paper, so we neglect the v_θ component. The same applies to the component of the magnetic field in the θ-direction. The linear magnetoacoustic wave motion is then governed by the following ideal MHD equations,

$$\rho_0 \frac{\partial v_r}{\partial t} = -\frac{\partial}{\partial r}\left(p_1 + \frac{B_0 b_z}{\mu_0}\right) + \frac{B_0}{\mu_0}\frac{\partial b_r}{\partial z}, \tag{4.1}$$

$$\rho_0 \frac{\partial v_z}{\partial t} = -\frac{\partial p_1}{\partial z}, \tag{4.2}$$

$$\frac{\partial b_r}{\partial t} = B_0 \frac{\partial v_r}{\partial z}, \tag{4.3}$$

$$\frac{\partial b_z}{\partial t} = -B_0 \frac{1}{r}\frac{\partial (r v_r)}{\partial r}, \tag{4.4}$$

$$\frac{\partial p_1}{\partial t} = -\rho_0 c_s^2 \left(\frac{1}{r}\frac{\partial (r v_r)}{\partial r} + \frac{\partial v_z}{\partial z}\right), \tag{4.5}$$

$$\frac{\partial \rho_1}{\partial t} = -\rho_0 \left(\frac{1}{r}\frac{\partial (r v_r)}{\partial r} + \frac{\partial v_z}{\partial z}\right). \tag{4.6}$$

Here, p is the gas pressure, ρ is the density and $\mathbf{b} = (b_r, b_\theta, b_z)$ is the perturbed magnetic field. We have assumed that the plasma motion is adiabatic. The subscripts 0 and 1 refer to unperturbed and perturbed states, respectively.

Now, assume that the wave is harmonic and propagating and let $v_r = A(r)\cos(kz - \omega t)$. We then obtain the following equations for the perturbed variables,

$$\omega b_r = -B_0 k v_r, \tag{4.7}$$

$$\rho_0 \left(\frac{v_A^2 k^2}{\omega} - \omega \right) A(r) \sin(kz - \omega t) = \frac{\partial}{\partial r} \left(p_1 + \frac{B_0 b_z}{\mu_0} \right) \tag{4.8}$$

$$\rho_0 \frac{\partial v_z}{\partial t} = -\frac{\partial p_1}{\partial z}, \tag{4.9}$$

$$b_z = \frac{B_0}{\omega} \frac{1}{r} \frac{\partial (rA(r))}{\partial r} \sin(kz - \omega t), \tag{4.10}$$

$$\frac{\partial p_1}{\partial t} = c_s^2 \frac{\partial \rho_1}{\partial t} = -\rho_0 c_s^2 \left(\frac{1}{r} \frac{\partial (r v_r)}{\partial r} + \frac{\partial v_z}{\partial z} \right) \tag{4.11}$$

Integrating Equation (4.11) with respect to t and using Equation (4.9) (which is also integrated with respect to t) gives

$$p_1 = c_s^2 \rho_1 = -\frac{\omega \rho_0 c_s^2}{(c_s^2 k^2 - \omega^2)} \frac{1}{r} \frac{\partial (rA(r))}{\partial r} \sin(kz - \omega t). \tag{4.12}$$

The full derivation can be found in Appendix 1. Comparing Equation (4.10) to Equation (4.12), it can be noted that the magnetic field, b_z, and the pressure (density) are 180 degrees out of phase. This depends on the sign of $c_s^2 k^2 - \omega^2$, which is assumed to be positive. Consideration of Equations 4.8, 4.10 and 4.12 leads to the conclusion that v_r is 90° out of phase with b_z and −90° out of phase with p_1.

The flux conservation equation for the perturbed variables gives the following relation,

$$B_0 S_1 = -b_{1z} S_0, \tag{4.13}$$

where S refers to the cross-sectional area of the flux tube. We conclude that the perturbation of the area is out of phase with the perturbation of the z-component of the magnetic field, hence, the area is in phase with the fluctuations of the thermodynamic quantities. Perhaps more importantly, we re-write Equation (4.13) as

$$\frac{S_1}{S_0} = -\frac{b_{1z}}{B_0}. \tag{4.14}$$

Hence, if we are able to measure oscillations of a pore's area, we can calculate the percentage change in the magnetic field due to these oscillations (assuming conservation of flux in the pore). This was previously suggested by Grant *et al.*

(2015). Exploiting this relation will allow a comparison to be made between the observed changes in pore area and the magnetic oscillations found from Stokes profiles (e.g. Balthasar *et al.*, 2000). Furthermore, as there are known difficulties with using the Stokes profiles, observing changes in pore area could provide a novel way of validating or refuting the observed magnetic oscillations derived from Stokes profiles. These simplified phase relations were confirmed in a more complicated case by e.g., Moreels and Van Doorsselaere (2013) and Moreels *et al.* (2013), who also derived the phase relations for other linear MHD waves.

Previous research by Fujimura and Tsuneta (2009) showed that the magnetic field (pore area) should be in phase (out of phase) with the intensity if the oscillations are due to changes in optical depth, i.e., an opacity effect. This is the same relationship for the fast magnetoacoustic sausage mode, thus, identification of the fast magnetoacoustic mode will prove difficult with only the two variables used in this chapter.

By measuring the change in pore area with time, we will also be able to estimate the amplitude of the radial velocity perturbation. The changes in area are related to changes in the radius of the flux tube by

$$\frac{S_1}{S_0} = \frac{2r_1}{r_0}, \tag{4.15}$$

where r_0 and r_1 are the unperturbed radius and perturbation of the radius, respectively, assuming the flux tube has a cylindrical geometry. Once a periodic change in radius is identified, the radial velocity of the perturbation can then be calculated using the following relation

$$v_r = \frac{\partial r}{\partial t} = \frac{2\pi r_1}{P}. \tag{4.16}$$

Note the term "sausage mode" was introduced for waves in magnetic tubes with a circular cross-section. The main property of these waves that distinguishes them from other wave modes is that they change the cross-sectional area. The cross sectional areas of observed pores are typically non-circular. However, it seems to be reasonable to use the term sausage mode for any wave mode that changes the cross-sectional area. Several preceding papers have looked into non-circular, e.g., elliptic shapes, and found the effects to be marginal on the MHD waves within these tubes (see Erdélyi and Morton 2009 and Morton and Ruderman 2011).

4.3.2 Period ratio of standing slow MHD wave

The period of a standing wave in a uniform and homogeneous flux tube is given by $P \approx 2L/nc_{ph}$, where L is the tube length, n is a integer determining the wave mode harmonics and c_{ph} is the phase speed of the wave. This ratio is for ideal homogeneous tubes, however, this is not the case for the solar atmosphere from the photosphere to the transition region. Luna-Cardozo *et al.* (2012) modelled the effect of density stratification and expansion with the height of the flux tube on the ratio of the fundamental and first overtone periods for a vertical flux tube sandwiched between the photosphere and transition region. Their analysis studied the slow standing MHD sausage mode and assumed a thin flux tube with a small radial expansion with height. They investigated two cases; case one is where the flux tube undergoes weak magnetic expansion with constant density, finding,

$$\frac{\omega_2}{\omega_1} = 2 - \frac{15}{2}\frac{\beta_f}{(6+5\beta_f)\pi^2}(\Gamma - 1), \tag{4.17}$$

where ω_i is the period of specific harmonic or overtone (i.e., 1, 2), β_f is the plasma-β at the base of the flux tube and Γ is the ratio of the radial size of the flux tube at the apex to the foot-point. Here, Equation (4.17) is Equation (43) from Luna-Cardozo *et al.* (2012). Case two is where the flux tube has density stratification but a constant vertical magnetic field, finding,

$$\frac{\omega_2}{\omega_1} = \left[\frac{16\pi^2 + \left(\ln\frac{1-\sqrt{1-\kappa_1}}{1+\sqrt{1-\kappa_1}}\right)^2}{4\pi^2 + \left(\ln\frac{1-\sqrt{1-\kappa_1}}{1+\sqrt{1-\kappa_1}}\right)^2}\right]^{1/2}, \tag{4.18}$$

where κ_1 is the square root of the ratio of the density at the top of the flux tube to the density at the footpoint ($\kappa_1 = (\rho_{apex}/\rho_{footpoint})^{0.5}$). Here, Equation (4.18) is Equation (40) from Luna-Cardozo *et al.* (2012). The upper end of the flux tube may well be the transition region while the footpoint is in the photosphere. It should be noted that the form of Equation (4.18) depends on the longitudinal density profile; a density profile where the tube speed increased linearly with height was used in this analysis.

This may or may not model a realistic pore and given the uncertainty of the equilibrium quantities this must be kept in mind in order to avoid over-interpretation. Both Equations (4.17) and (4.18) modelling the frequency ratio of standing oscillations indicate that the ratio of the first harmonic to the fundamental will always be less than two for flux tube expansion while the density stratification could increase this value. Furthermore, the thin flux tube

approximation is used to derive these equations. Obviously, in a real flux tube, both the density and magnetic stratification would be present at the same time and would alter the ratio. This is not accounted for at the moment. Finally, Equations (4.17) and (4.18) are independent of height, which may limit the results, as it has been suggested that the height to the transition region varies (Tian *et al.*, 2009).

4.4 Results and discussion

Figures 4.2 and 4.3 show the results of a wavelet analysis of the area and intensity time series for the DOT and DST telescopes, respectively. The original signal is displayed above the wavelet power spectrum and the shaded region marks the cone of influence (COI), where edge effects of the finite length of the data affect the wavelet transform results. The contours show the confidence level of 95%.

4.4.1 DOT pore

There are four distinct periods found in the area time series of the pore; 4.7, 8.5, 20 and 32.6 minutes. The last period is outside the COI due to the duration of the time series, so it has been disregarded. It should be noted that periods of 8, 14 and 35 minutes have been observed in sunspots by Kobanov and Makarchik (2004). This is important because pores and sunspots share a number of common features. The intensity wavelet shows 4 periods of oscillations; 4.7, 8.6, 19.7, and 35 minutes. These periods are similar, if not the same as the period of the area oscillations, which enables a direct comparison of the two quantities. There is significant power that is co-temporal, which can be observed in both the intensity and area wavelets.

Using cross-wavelet in conjunction with the EMD allows the verification of the phase difference between the area and intensity signals for each period. These methods show that the phase difference is very close to 0°, i.e., the oscillations are in phase meaning that they are slow sausage MHD waves. The current MHD theory that is available (to the knowledge of the author), does not offer a different interpretation. Furthermore, the percentage change in intensity is of order as previously reported in Balthasar *et al.* (2000) and Fujimura and Tsuneta (2009). This suggests that, we are most likely observing the same oscillatory phenomena as these authors.

We also have to be certain that any change in area we observe is due to the magnetoacoustic wave rather than a change in the optical depth of the plasma. Fujimura and Tsuneta (2009) provide an insight into the expected

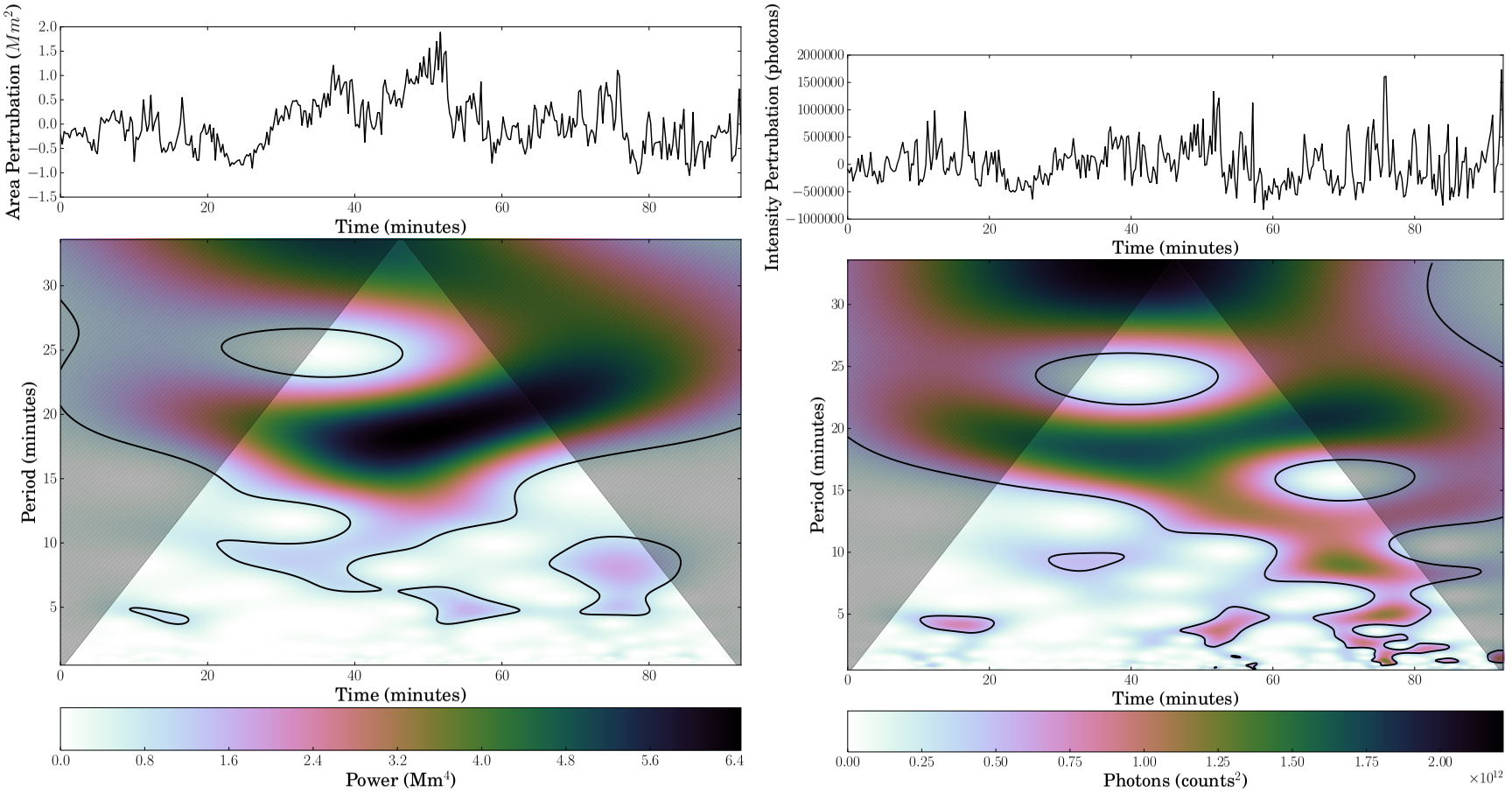

Fig. 4.2 Evolution of the area of the pore observed with DOT (*Upper panels*). The corresponding wavelet power spectrum for a white noise background. The cone of influence is marked as the shaded region and the contour lines show the 95% confidence level (*Lower panels*).

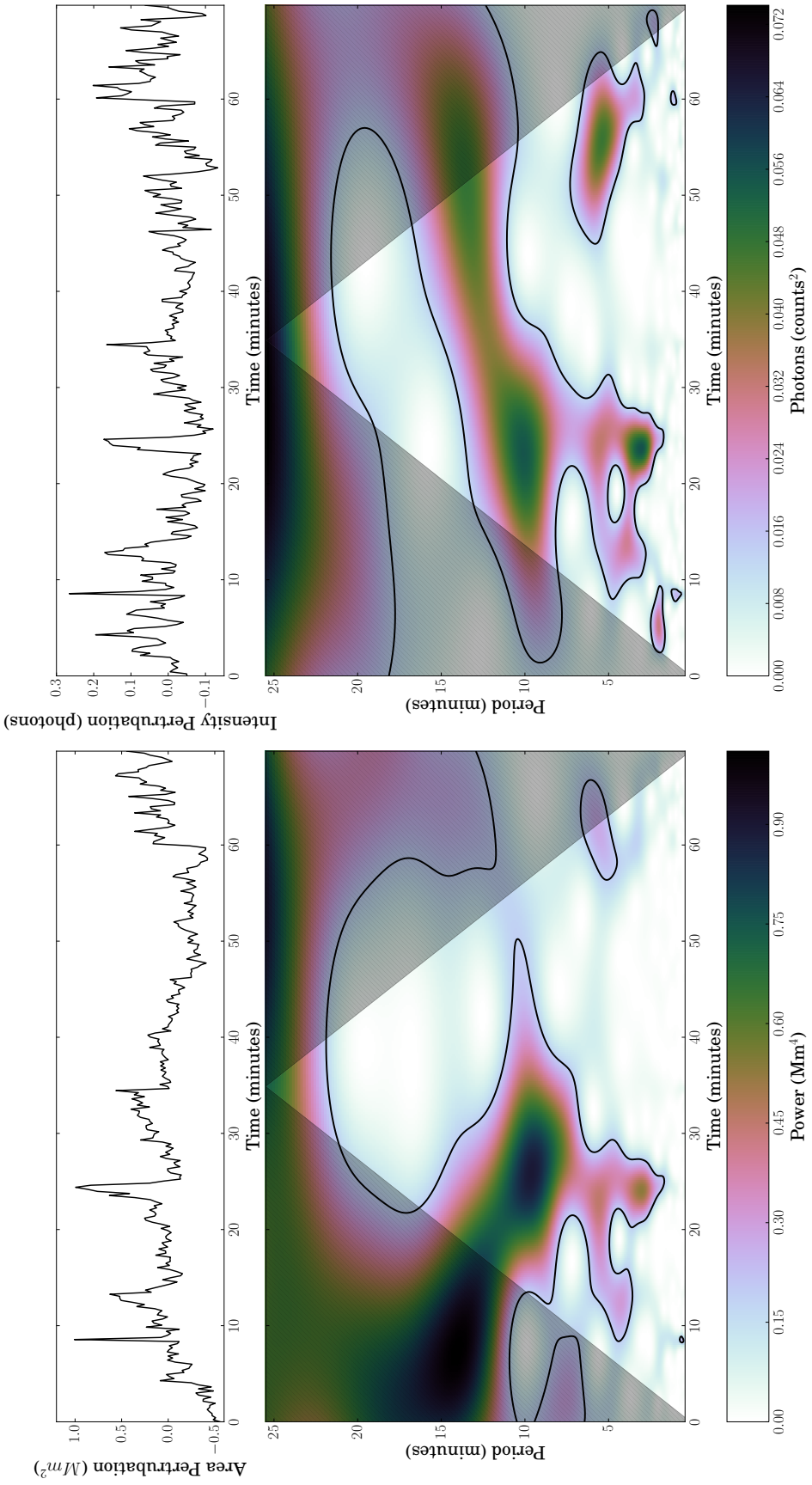

Fig. 4.3 Same as Figure 4.2 but for the pore observed with ROSA. Note that the intensity counts are normalised by the ROSA reduction pipeline (Jess *et al.*, 2010).

differences between the phase of magnetic field and intensity oscillations due to waves or the opacity effect. They demonstrate that the magnetic field (pore area) should be in phase (out of phase) with the intensity if the oscillations are due to changes in optical depth. We note that this is the same relationship expected for the fast magnetoacoustic sausage mode. Hence, the identification of the fast magnetoacoustic mode in pores may prove difficult with only limited datasets.

The application of Equations (4.15) and (4.16) require information about the amplitude of the area perturbation. This can be achieved using either an FFT power spectrum or the IMF's amplitude from the EMD analysis. Here, we use EMD for the amplitudes (which are time-average values) and they are 3.87x10^5 km^2, 3.61x10^5 km^2 and 5.90x10^5 km^2 for the oscillations with periods of 4.7, 8.5 and 20 minutes, respectively. It was not possible to find the amplitude of the largest period, as it did not appear in the EMD output. The values of the area perturbation translate, using Equation (4.15), to 37, 34, and 56 km, respectively, for the amplitude of the radial perturbation. Note that the increase in radius is about 100 km, meaning that the perturbation is only of the order of 1 pixel (at the DOT's resolution). This is within the expectations of linear theory (Jess *et al.*, 2015; Moreels and Van Doorsselaere, 2013; Moreels *et al.*, 2013).

Using the values above allows us to calculate the radial velocity perturbation for each period, by means of Equation (4.16). For the periods of 4.7, 8.5, and 20 minutes, we determine the radial velocity perturbation as 0.82, 0.42, and 0.29 km s^{-1}, respectively. The obtained radial speeds are very sub-sonic, as the sound speed is $\approx$ 10 km s^{-1} in the photosphere. They are, however, of order of observed horizontal flows around pores.

Furthermore, it is also possible to estimate the percentage change in the magnetic field that is expected from the identified linear slow MHD sausage modes. The percentage change in pore area, hence magnetic field, is found to be

$$\frac{A_1}{A_0} = \frac{b_1}{B_0} \rightarrow 4 - 7\%.$$

For another pore, the percentage change was found to be similar at 6% (Grant *et al.*, 2015). Let us now assume that the equilibrium magnetic field strength of the pore takes typical values of 1000-2000 G. Then, the amplitude of the magnetic field oscillations should be 40-140 G. The lower end of this estimated range of percentage change in the magnetic field agrees well with percentage changes in the magnetic field obtained using Stokes profiles by, for example, Balthasar *et al.* (2000) and Fujimura and Tsuneta (2009). However, the upper end of the range, i.e. $\sim$ 140 G, appears twice as large as any of the previously

reported periodic variations in the magnetic field. This apparent difference could be due to the spatial resolution of the magnetograms averaging out the magnetic field fluctuations. A summary of these findings can be found in Table 4.1.

Now we estimate the wavelength (wavenumber) for each mode. An important fact needs to be remembered, i.e., the velocity perturbation determined is radial, not vertical. Furthermore, since the waveguide is strongly stratified, we define the wavelength as the distance between the first two nodes, which is the half wavelength of the wave. However, in this regime, the vertical phase speed of the slow sausage MHD wave is the tube speed, which is $c_T \approx 4.5$ km s^{-1} using typical values for the photospheric plasma (Edwin and Roberts, 1983; Evans and Roberts, 1990). For the periods of 4.7, 8.5 and 20 minutes we obtain estimates of the wavelength (wavenumber) as 1269 km (4.95x10^{-6} m^{-1}), 2268 km (2.77x10^{-6} m^{-1}) and 5319 km (1.18x10^{-6} m^{-1}), respectively. Note that these wavelengths are larger than the scale height in the photosphere ($\approx$ 160 km) or the lower chromosphere. For the observed pore, it had an average radius, $a = 1.5$ Mm, where $ka = 8, 5, 2$. See Table 4.2 for a summary.

4.4.2 ROSA pore

There are four distinct periods found in the area time series of the pore observed by ROSA; 2-3, 5.5, 10 and 27 minutes. All of these reported periods are at least at the 95% confidence level (or over). A few words about two of the periods have to be mentioned. First, the power of the 2-3 minute period is spread broadly, and, as such it is hard to differentiate the exact period. Secondly, the 10-minute period slowly migrates to 13.5 minutes as the time series comes to its end. The intensity wavelet shows four periods of oscillations; 2-3, 5.5, 10, and 27 minutes. For the pore observed by DOT, the oscillations found in the area and intensity data share similar periods. Also, there is another period that is below the 95% confidence level for white noise at 1-2 minutes at the start of the time series. This is a similar behaviour as found for the DOT pore.

We found that the phase difference between the area and intensity periods is 0°. This means, as before, that these oscillations are in phase and are interpreted as signatures of slow sausage MHD waves. While we have chosen not to discuss the out of phase behaviour, there are small regions of 45° phase difference that have been previously reported (Dorotovič *et al.*, 2014). This needs to be investigated in the future, as the author is unaware of which MHD mode would cause this behaviour, however, it has been suggested that is due to noise within the dataset (Moreels *et al.*, 2015a). As for the DOT pore, the

DOT	r_1	v_{r_1}	$\frac{b_{z1}}{B_0}$	ROSA	r_1	v_{r_1}	$\frac{b_{z1}}{B_0}$
Period 1 4.7 mins	37 km	0.82 km s^{-1}	4.34%	Period 1 2-3 mins	69.1 km	3.03 km s^{-1}	26.3%
Period 2 8.4 mins	34 km	0.42 km s^{-1}	4.04%	Period 2 5.5 mins	74.2 km	1.41 km s^{-1}	28.2%
Period 3 19.7 mins	56 km	0.29 km s^{-1}	6.60%	Period 3 10 mins	117 km	1.23 km s^{-1}	44.5%

Table 4.1 The properties of each observed period for the DOT and ROSA data respectively. r_1 is the radial perturbation, v_{r1} is the velocity perturbation and $\frac{b_{z1}}{B_0}$ is the magnetic field perturbation. These quantities are determined by using Equations 4.15 and 4.16

DOT	λ_z	k_z	$k_z a$	ROSA	λ_z	k_z	$k_z a$
Period 1 4.7 mins	1269 km	4.95 x10^{-6} m^{-1}	8	Period 1 2-3 mins	540-810 km	7.76-12 x10^{-6} m^{-1}	4-6
Period 2 8.4 mins	2268 km	2.77 x10^{-6} m^{-1}	5	Period 2 5.5 mins	1485 km	4.2 x10^{-6} m^{-1}	2
Period 3 19.7 mins	5319 km	1.18 x10^{-6} m^{-1}	2	Period 3 10 mins	2700 km	2.33 x10^{-6} m^{-1}	1

Table 4.2 The wavelength (wavenumber) for each observed period for the DOT and ROSA data respectively. Here, $k = 2\pi/\lambda$ and $\lambda = v/f$, where k is the wavenumber, λ is the wavelength, v is the velocity and f is the frequency.

same properties can be obtained for each period observed as within the ROSA pore, which are summarized in Table 4.1 and 4.2.

The amplitudes for the area oscillations are 2.29x10^5 km^2, 2.45x10^5 km^2, and 3.87x10^5 km^2 for periods of 2-3, 5.5, and 10 minutes, respectively. The 13.5-minute period is found by the EMD process as well, and has an amplitude that is the same as that of the 10-minute period. Again, it was not possible to find the amplitude of the largest period. These then, lead to the radial perturbation amplitude of 69.1, 74.2, and 117 km and a radial velocity perturbation as 3.03, 1.41, and 1.23 km s^{-1}, respectively. The increase in radius is around 100 km meaning that the perturbation is only of the order of 2 pixels (at ROSA's resolution). This means that for each part of the structure, its radius increases by 2 pixels. Once again, the radial velocity perturbations are found to be sub-sonic.

The percentage change in the pore's area, and thus the magnetic field, is given by

$$\frac{A_1}{A_0} = \frac{b_1}{B_0} \rightarrow 25 - 45\%.$$

This is a large effect and linear MHD theory might not be applicable in this case. From the above relations we conclude that the size of the magnetic field oscillation is in the region of 200-400 G. To the current knowledge of the author, this has not been reported previously. This is a substantial increase when compared to the measurements of the pore detected by DOT, as the amplitudes for these oscillations are of the same order but the cross-sectional area of the pore is an order of magnitude smaller. This suggests that the oscillation strength might be independent of the scale of the structure (Dorotovič *et al.*, 2014).

Once again, we determine the wavelength (wavenumber) for each period, using the tube speed as defined in the previous section. For the periods of $2-3$, 5.5, and 10 minutes we obtain estimates of the wavelength (wavenumber) as 540-810 km (7.76x10^{-6} m^{-1}), 1485 km (3.58x10^{-6} m^{-1}), and 2.2 Mm (2.85x10^{-6} m^{-1}), respectively. For the observed pore radius, $a = 0.5$ Mm, we obtain values of $ka = 2, 1.8, 1.5$, and 1.5.

4.4.3 Standing oscillations

With the important understanding that the observed waves are trapped, there is a possibility of them being standing waves. Assuming that the pore can be modelled as a straight homogeneous magnetic flux tube that does not expand with height, the sharp gradients (often modelled as discontinuities) of the temperature/density at the photosphere and at the transition region form a

DOT Period (Mins)	Ratio (P_1/P_i)	ROSA Period (Mins)	Ratio (P_1/P_i)
8.5 mins	-	10 mins	-
4.7 mins	1.81	5.5 mins	1.81
		2-3 mins	3.3-5

Table 4.3 The periods of oscillations as well as the harmonic ratios for the DOT and ROSA pore respectively. The periods listed here exist at 95% confidence level and are within the COI. Periods greater than 10 minutes have been neglected.

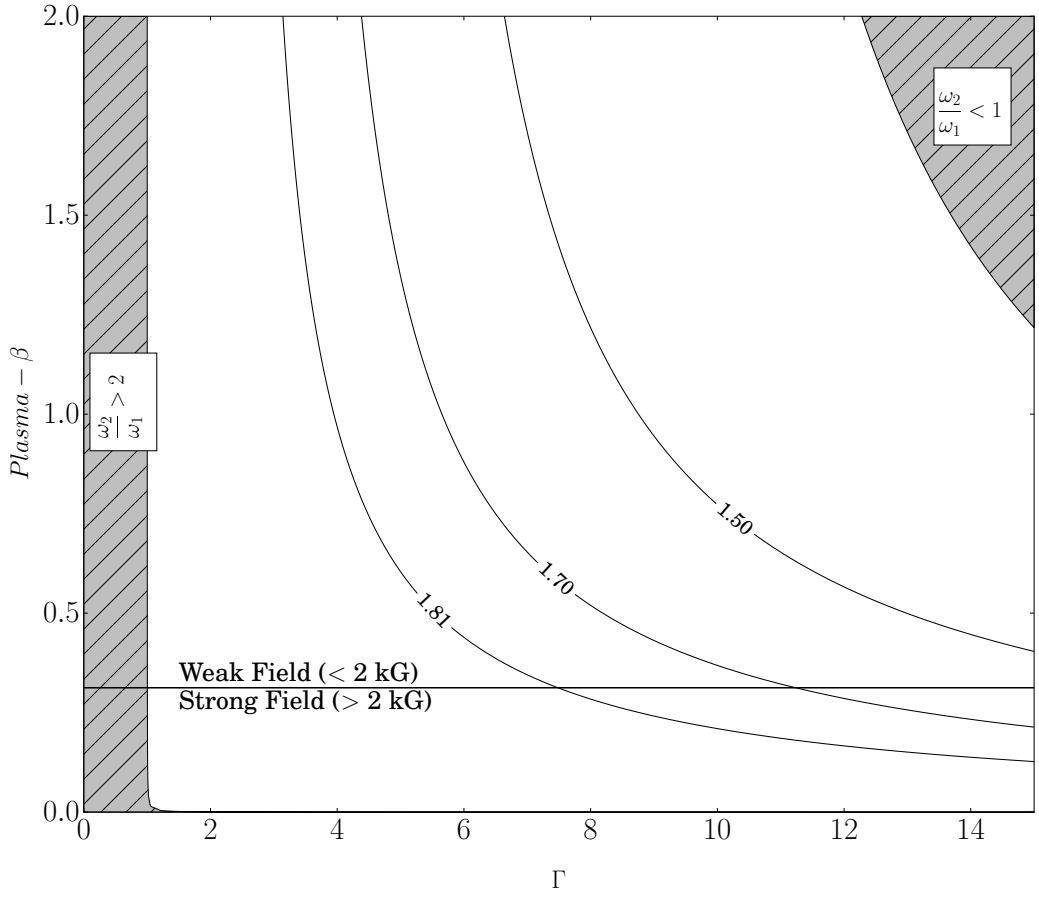

Fig. 4.4 The range of solutions for Equation (4.17). The threaded areas are where the period ratios are either less than one or greater than two. The horizontal line divides the image into a weak (< 2 kG) and strong (> 2 kG) field regions for the plasma-β. The blue contour lines indicate observed period ratios for this paper and the values within Dorotovič *et al.* (2014).

resonant cavity that can support standing waves (see Fleck and Deubner, 1989; Malins and Erdélyi, 2007).

Calculating the harmonic periods ($P \approx 2L/nc_{ph}$, where L is the distance between the boundaries (2 Mm), n is the harmonic number), a fast MHD oscillation ($c_p \approx 12$ kms^{-1}) would have a fundamental period ~333 s, while the period of a slow MHD wave ($c_p \approx 5.7$ kms^{-1}) would be ~700 s. Other slow MHD sausage waves have been observed with phase speeds similar to this (Moreels *et al.*, 2015a). The interpretation of the observed waves is that they are slow MHD sausage waves, which, in the ideal homogeneous case, is the most similar to the observed results; however, it is still different by two minutes. Therefore, the basic assumption of an ideal homogeneous flux tube (constant L, constant c_{ph} etc.) is inadequate for explaining the results presented in this chapter.

There are several further considerations that need to be taken into account. From observations, many magnetic structures are not cylindrical or symmetrical and are often irregular in shape. Furthermore, large-scale magnetic structures have been thought to be made up of either a tight collection of small-scale flux tubes or one large monolithic structure (Priest, 1984, and the references within). Also, these magnetic structures extend from the photosphere to the transition region which means that the plasma-β will vary by an order of 2 magnitude, which will change the dynamics of the MHD waves considerably. We have also ignored the effect of gravity (i.e., density stratification Andries and Cally 2011; Díaz and Roberts 2006), as well as the equally important fact that flux tubes expand with height, i.e., magnetic stratification, which alters the ratio of the periods, i.e, $P_1/P_2 \neq 2$ (Luna-Cardozo *et al.*, 2012). All of these effects will further affect the wave dynamics inside flux tubes.

Here, we will ignore periods greater than 10 minutes; as shown above in the ideal homogeneous case, the largest period possible is 11.6 minutes for MHD waves (with the above assumptions). Here, we will consider two effects: the effect of density stratification and magnetic expansion with height in the radial direction. For the first case; Equation (4.18) is calculated with typical density values from the VAL-III C model (Vernazza *et al.*, 1981) at the apex (transition region) and footpoint (photosphere) of the flux tube. The VAL-III C model is an estimation of a quiet-Sun region and the interior density ratio between the photosphere and the transition region of a flux tube need not necessarily differ greatly from that of the exterior atmosphere (see Figures 3 and 1 of Gent *et al.*, 2013 and Gent *et al.*, 2014, respectively). The resulting value for the period ratio in this instance is 1.44 (density values are 2.727x10^{-7} and 2.122x10^{-13} g cm^{-3} for the footpoint and apex, respectively). Using the model given by Maltby *et al.* (1986), which models a sunspot umbra, this period

ratio is 1.38 (density values are $1.364\text{x}10^{-6}$ and $9.224\text{x}10^{-14}$ g cm^{-3} for the footpoint and apex respectively). This does not correspond well to the results in this paper, but only for one previously reported result; a highly dynamical non-radially uniform sunspot (Dorotovič *et al.*, 2014). The ratio is substantially smaller than what is detected here, which means the first harmonic should be at ≈ 5.9 minutes. The reason for this, the author believe, is due to the effect of finite radius. The dispersion relation for slow MHD waves in a finite radial flux tube, shows that the dispersion related to the finite tube radius increases the wave frequency. The shorter the wavelength, the stronger the dispersion effect is. Hence, the relative increase of the first overtone frequency due to the effect of finite radius is larger than that of the fundamental harmonic. This modifies the period of the first harmonic to be higher, which shifts the period ratio to be larger than values that are obtained theoretically in the thin tube approximation. Table 4.3 details the periods that have been found from the two pore datasets used within this article. However, the arguments set forth in this paragraph have been taken into account, and as a result, the table contains only the periods that can be supported within these magnetic flux tubes. In conclusion, this density stratification model does not seem to be applicable to the observational results presented here, which the is an important point to note.

Figure 4.4 details the various solutions (*i.e.,* period ratio) for Equation (4.17) over a large range of plasma-β and expansion ratio (Γ). It is difficult to estimate how much a flux tube expands with height, therefore, we explore the parameter space widely, taking Γ of 0-15. The values for the plasma-β are divided into strong ($\geq$ 2 kG) and weak ($\leq$ 2 kG) field regions, as the magnetic field of flux tubes hypothesised, and will vary from 0.5 kG to 4 kG. The pores were observed before the launch of NASA's Solar Dynamics Observatory (SDO), so the best magnetic data comes from the Michelson Doppler Imager (MDI) instrument on board SOHO. As such, the magnetic field of these pores is hard to know precisely due to their small scale and MDI's large pixel size. However, ground-based observations of similar sized pores reveal magnetic fields ranging from 1 kG to 2.5 kG. The blue contour lines show the parameter space that matches the period ratios reported in this article and the ones in Dorotovič *et al.* (2014). For example, if the plasma-β is around 1, the expansion factors for the three period ratios reported here are around 4, 6, and 9. If we have plasma-$\beta \ll 1$, the expansion ratio starts to increase rapidly.

Once again, this effect can be dominant when the flux tube expands too much, however, it is unlikely that a flux tube would expand by such a large amount. Browning and Priest (1982), for example, suggest that when the

internal gas pressure exceeds the external gas pressure, the flux tube becomes unstable and this occurs when the flux tube expands greatly with height.

For the cases presented in this chapter, the flux tube has to expand four to six times to have a period ratio that is observed. In a number of numerical simulations that model these types of flux tubes, the magnetic field expands approximately 4-10 times, which is in good agreement with our findings, which is another important result (see Fedun *et al.*, 2011a,b; Khomenko *et al.*, 2008). It should be noted that these estimates for expansion are for flux tubes with magnetic fields that have a field strength less than 2 kG.

Unfortunately, as of yet, little is known about the source of the oscillations analysed in this paper. One possible origin of MHD sausage waves is suggested by e.g. Khomenko *et al.* (2008) and Fedun *et al.* (2011a), where magnetoacoustic wave propagation in small-scale flux tubes was modelled using non-linear MHD simulations. One of the results of their simulations is that 5-minute vertical drivers can generate a mixture of slow and fast sausage modes in localised magnetic flux tubes that propagate upward. Furthermore, Fedun *et al.* (2011b) model the effect of photospheric vortex motion on a thin flux tube, finding that vertex motions can excite dominantly slow sausage modes. However, these simulations need to be developed further before we may comfortably link them to our assertions.

Another potential source is from mode conversion that will occur at the lower region of the photosphere within sunspots and pores. For example, Khomenko and Cally (2012), modelled a background sunspot-like atmosphere, and solving the non-linear ideal MHD equations for this system, found that the fast MHD wave will turn into a slow MHD sausage wave at the Alfvén-acoustic equipartition level (which is where the sound speed is equal the Alfvén speed) and the reverse is also true. The fast MHD wave to Alfvén conversion occurs higher up, where there is a steep Alfvén speed gradient, as the fast MHD wave will reflect from this boundary. Below this level, the MHD waves are fast and above this level, slow MHD waves can be supported. This level occurs at approximately 200 km in their model. The observations used within this paper are thought to form at a height around 250 km. Furthermore, sunspot umbras are depressed in height and it would likely be the same for pores. These facts can offer an insight into the formation height of G-band since we believe that we are observing a primary slow acoustic mode modified by the magnetic field i.e., the slow MHD sausage wave.

A word of caution: the absence of line-of-sight (LOS) Doppler data, it is difficult to know whether the oscillations reported are standing or propagating. The data available for pores does not cover higher levels of the solar atmosphere such as the chromosphere or the transition region. The data presented here only

represents a slice of the flux tube near the photosphere. Future work is needed to acquire simultaneous observations of pores in several wavelengths in order to sample the solar atmosphere at different heights. Detailed spectral images would allow other LOS quantities such as Doppler velocity and magnetic field to be measured. This way, the oscillations could be determined confidently either as standing or propagating due to their different phase relations.

4.5 Conclusions

The use of high-resolution data with short cadence, coupled with two methods of data analysis (wavelets and EMD), has allowed the observation of small-scale wave phenomena in magnetic waveguides situated on the solar surface. By studying the area and intensity perturbations of pores, it enables the investigation of the phase relations between these two quantities with the use of wavelets and EMD. The in phase (0° phase difference) behaviour reveals that the oscillations observed are indicative of slow sausage MHD waves. Furthermore, with the amplitude of oscillations measured, several properties could be estimated; such as the amplitude of the magnetic field perturbation and the radial speed of the perturbation. The scale of the magnetic field perturbations that are caused by slow MHD waves is of the order 10% and has radial speeds that are sub-sonic when compared to the sound speed at the photosphere. With the MHD mode of these waves identified, the obtained vertical wavelength indicates that the flux tubes would have a strong reflection at the transition region boundary, further indicating a chromospheric resonator. Finally, the investigation of the period ratio of the oscillations suggests that the fundamental and first harmonic has been observed within these flux tubes. The period ratio observed, coupled with magneto-seismology, enabled an expansion factor to be calculated that was in very good agreement with values found in numerical models used for MHD wave simulations.

Chapter 5

The detection of upwardly propagating waves in a pore[1]

[1]This chapter is based on Freij, N., Scullion, E. M., Nelson, C. J., Mumford, S., Wedemeyer, S. and Erdélyi, R., 2014, "The Detection of Upwardly Propagating Waves Channeling Energy from the Chromosphere to the Low Corona", *The Astrophysical Journal*, **791**, 61. [DOI], [ADS], [arXiv:1408.4621 [astro-ph.SR]]. Reproduced with permission from AAS

5.1 Introduction

How energy is transported from the lower solar atmosphere into the corona is an important question that has yet to be fully answered despite decades of research(Erdélyi, 2004; Erdélyi and Ballai, 2007; Taroyan and Erdélyi, 2009). The complex interactions between strong magnetic fields and powerful flows, the latter created by the interplay of gravity, convection and magnetic forces, leads to a number of dynamic phenomena throughout the atmosphere, such as magneto-hydrodynamic (MHD) waves (Edwin and Roberts, 1983), which are theorised to supply energy into the corona. Strong inhomogeneities and steep gradients of key atmospheric properties (such as temperature and density) can lead to strong reflection of wave energy in the upper chromosphere. It has proved difficult to both observe (Aschwanden, 2006; Jess *et al.*, 2009; Marsh and Walsh, 2006; Mathioudakis *et al.*, 2013; McIntosh *et al.*, 2011; Morton *et al.*, 2012; Parnell and De Moortel, 2012; Taroyan and Erdélyi, 2009; Wedemeyer-Böhm *et al.*, 2012) and simulate (Erdélyi and Fedun, 2007, 2010; Hasan *et al.*, 2005; Peter *et al.*, 2006; Steiner *et al.*, 1998; Vigeesh *et al.*, 2012) the propagation of energy from the lower atmosphere into the corona (De Pontieu *et al.*, 2007, 2011; McIntosh, 2012; Rutten, 2012; Vecchio *et al.*, 2007; Zaqarashvili and Erdélyi, 2009).

The most basic model of MHD theory suggests that three distinct types of waves should manifest in the solar atmosphere; namely slow and fast magneto-acoustic and the widely sought-after Alfvén wave (Banerjee *et al.*, 2007; Jess *et al.*, 2009; Mathioudakis *et al.*, 2013; McIntosh *et al.*, 2011; McLaughlin *et al.*, 2011; Suzuki, 2011). High spatial and temporal resolution observations carried out using modern ground- and space-based instrumentation have revealed a plethora of energetic, incompressible (Aschwanden *et al.*, 1999; De Pontieu *et al.*, 2007; Jess *et al.*, 2009), compressible (Morton *et al.*, 2012), and significantly more complicated (De Pontieu *et al.*, 2011; Wedemeyer-Böhm *et al.*, 2012), oscillations and flows. What has yet to be observed is the direct propagation of energy from the lower regions of the solar atmosphere into the corona raising the question as to whether any of these wave processes are actually heating the outer solar atmosphere. Here, we contribute to addressing this question.

Running penumbral waves (RPWs) were originally thought to be evidence of horizontal wave propagation (Bloomfield *et al.*, 2007; Giovanelli, 1972; Zirin and Stein, 1972) which traced the topology of the local magnetic field (Nye and Thomas, 1974; Zhugzhda, 1973) around large sunspots. Due to this assertion, RPWs have been largely ignored with regards to any potential injection of energy into the corona. More recently, it has been suggested that these events are, in fact, upwardly propagating waves (UPWs, Bloomfield *et al.* 2007; Bogdan

and Judge 2006; Jess *et al.* 2013), which could facilitate the propagation of non-thermal energy into the corona. Here, we present the first observations of UPWs situated around a pore and demonstrate that these waves can indeed penetrate from the lower solar atmosphere into the corona, potentially making them an excellent candidate for plasma heating within solar Active Regions (ARs).

Discussed here is the propagation of UPWs through the plasma surrounding a large pore structure. By conducting a multi-wavelength, multi-instrument analysis, we are able to trace upward propagating wave-fronts from the chromosphere into the transition region (TR) and corona, estimating key properties such as apparent horizontal and vertical velocities, and non-thermal energy supply. The chapter is organised as follows: Section 5.2 details the collection and reduction of the data presented; Section 5.3 describes the analysis of the data and studies the observed UPWs within the AR; Section 5.4 we summarise and conclude.

5.2 Data collection and reduction

The analysis presented here is conducted on AR 11511, which displayed a myriad of complex features during these observations. The ground-based data were obtained using the CRisp Imaging SpectroPolarimeter (CRISP Scharmer *et al.* 2008) instrument, situated at the Swedish 1-m Solar Telescope (SST), on the 22nd June 2012 between 07:23 UT and 08:28 UT, during a period of excellent seeing. These data have a high spatial resolution of around 0.2″ (1″ ≈ 725 km) and a cadence of 2.2 seconds, allowing the small-scale structures of the lower solar atmosphere to be resolved (diffraction-limited) using a narrow-band 0.0269 nm Hα filter centred on 656.28 nm. Hα line scans were returned for $-0.1032, -0.0774, 0$ and 0.1032 nm Each frame captured by the SST/CRISP instrument sampled a 68″ by 68″ FOV close to the disc centre. The data were reconstructed using the *Multi-Object Multi-Frame Blind Deconvolution* (MOMFBD) technique, giving an overall cadence of 2.2 seconds and a spatial resolution of 0.12″(van Noort *et al.*, 2005). We followed the standard procedures in the reduction pipeline for CRISP data (de la Cruz Rodríguez *et al.* (2015)) which includes the post-MOMFBD correction for differential stretching suggested by Henriques (2012), also see Sekse *et al.* (2013) for more details.

Finally, co-aligned highly ionised plasma comprising the upper solar atmosphere was observed using the Solar Dynamics Observatory's (SDO) Atmospheric Imaging Assembly (AIA) instrument at a spatial resolution of approximately 1.5″ and a temporal resolution of 12 seconds.

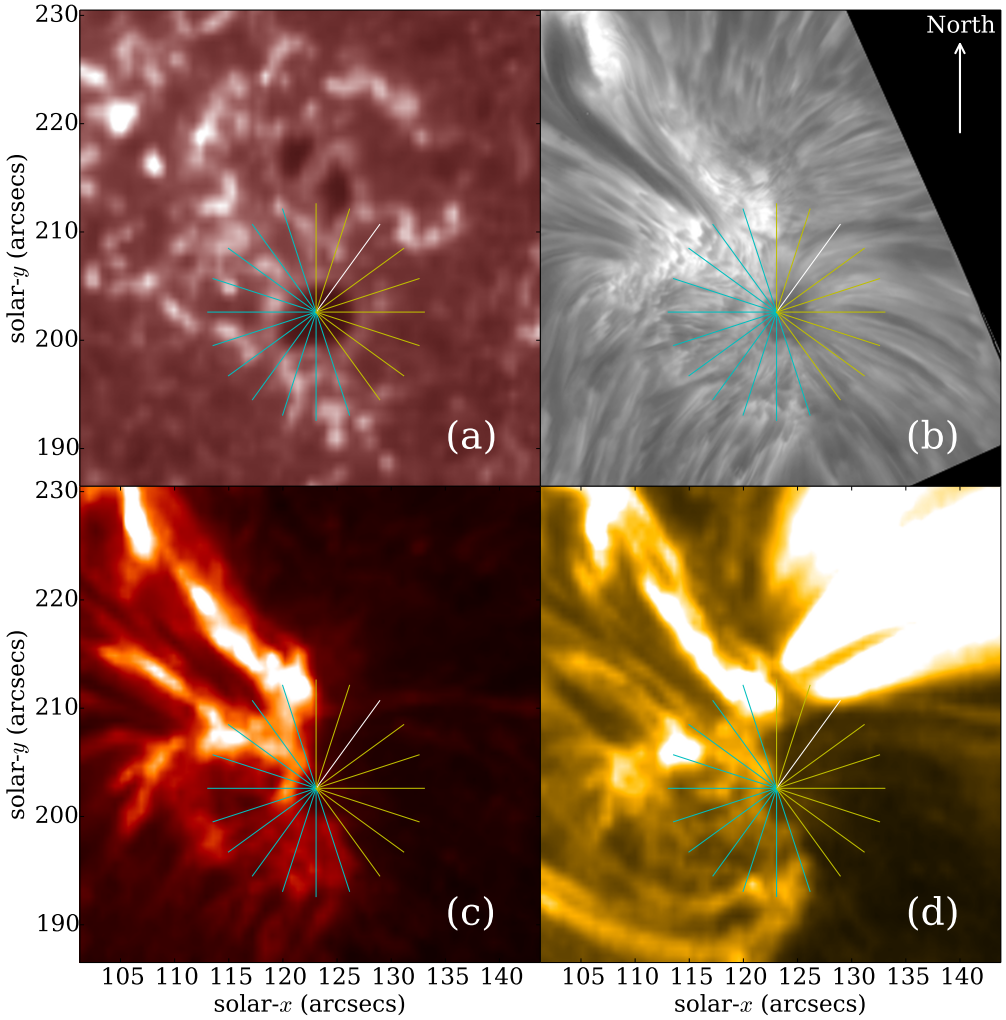

Fig. 5.1 An overview of the field-of-view (FOV) inferred by SST/CRISP and SDO/AIA consisting of: (a) SDO/AIA 170 nm, detailing the photosphere; (b) SST Hα 656.28 nm (line core) sampling the chromosphere; the (c) SDO/AIA 30.4 nm filter (TR); and the lower corona detailed by (d) SDO/AIA 17.1 nm. The white line on each image represents the slit used to construct the time-distance diagrams plotted in Figure 5.3. The yellow and cyan lines outline each slit used to investigate UPW behaviour. The yellow slits show where UPWs were observed and cyan slits show no UPWs.

In Figure 5.1, we include a general overview of the FOV analysed here, taken at 07:23 UT. The pore of primary interest is located at approximately [123″, 203″] in helioprojective coordinates, and can be easily identified as it is situated underneath the overlaid cyan star symbol. Four images sampled at different heights in the atmosphere are included to give an impression of the three-dimensional structuring evident in this region. The photosphere and chromosphere are sampled by the SDO/AIA 170 nm filter (Figure 5.1a) and the SST/CRISP Hα line core (Figure 5.1b), respectively. The dynamic fibril events which appear to protrude away from the large pore in the Hα line core, obscure the majority of the large-scale structuring (such as the network) observed within the photosphere. Only in regions where strong vertical magnetic fields are present, such as within the confines of the large pore, does any evidence of the photospheric structuring penetrate into the chromosphere. Finally, the TR and corona are observed through the SDO/AIA 30.4 nm (Figure 5.1c) and 17.1 nm (Figure 5.1d) filters. It should be noted that two small pores are also within the FOV, situated at approximately [123″, 215″], however, they are not evident in the Hα line core.

5.3 Results and discussion

5.3.1 The observed active region

In Figure 5.2, a stacked image outlining the counpling between the lower and upper regions of the solar atmosphere is presented. An extended FOV of the photospheric magnetic field is used as the base (with the SST/CRISP FOV overlaid as the purple box), from which the extrapolated field lines are plotted. Co-aligned photospheric magnetic field data were inferred by the SDO's Helioseismic and Magnetic Imager (HMI) instrument at a spatial resolution of around 1″ and a cadence of 45 seconds. Extrapolations of the magnetic field were then achieved by passing these data into the MPole Interactive Data Language package (Longcope, 1996; Longcope and Klapper, 2002).

We use MPOLE to determine the 3D coronal magnetic field line connectivity about the FOV as observed by CRISP. MPOLE implements the Magnetic Charge Topology models and the Minimum Current Corona model to derive the coronal field from a set of point charges. In our analysis, the charges are an approximation of an observed photospheric magnetic field. The complete set of charge positions and strengths (fluxes) are contained as a set poles. The poles are extracted from the observations through applying a feature tracking algorithm to HMI magnetograms of the active region of interest (extended about the CRISP co-aligned FOV by 50 arcsec in both solar-x and solar-y directions).

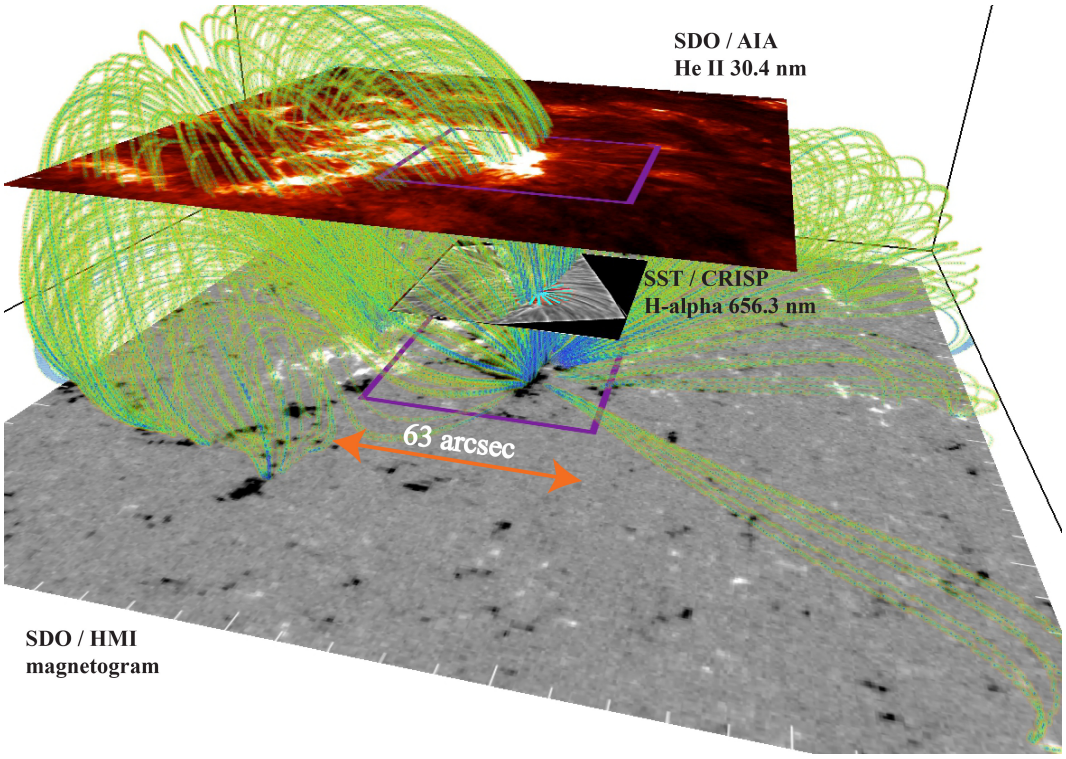

Fig. 5.2 The base layer indicates the magnetic field inferred by the SDO/HMI instrument. The purple box highlights the SST/CRISP FOV which is overlaid. An extended FOV context image from the SDO/AIA 30.4 nm filter is also included. The green lines are the visualisation of the magnetic field extrapolation. A strong correlation exists between these lines and the brighter regions in the SDO/AIA 30.4 nm image underpinning that the extrapolation is a reasonable approximation over such a large height.

Feature tracking of regions of positive and negative flux is carried out using YAFTA (Yet Another Feature Tracking Algorithm DeForest *et al.* 2007). Poles are labelled features which are collections of pixels in the magnetogram that are grouped according to criterion such as, spatial size and magnetic field strength. Subsequently, pixels below a threshold in flux density are not grouped, and receive a zero label in the mask. The thresholds are employed to ensure a suitably representative distribution of the magnetic flux concentrations of the active region of interest.

It is immediately noticeable that a non-rotationally symmetric distribution of field lines is present. Over-laid the magnetic field, we stack concurrent images from the SST/CRISP Hα, SDO/AIA 30.4 nm, and SDO/AIA 17.1 nm filters. Typically, the formation heights of the Hα line core is estimated to be around 1.5 Mm, which agrees to the mid-chromosphere (Leenaarts *et al.*, 2007). The SDO/AIA 30.4 nm and 17.1 nm filters correspond to plasma in the TR and low corona, while SDO/AIA 19.3 nm and 21.1 nm filters correspond to plasma in the corona/hot flare plasma and AR corona, respectively. The chromosphere shows many elongated dark and bright structures surrounding the

pore, identified as fibrils. Furthermore, a bright moss-like region to the north of the pore is evident, which corresponds well with regions of high magnetic flux, identified by the extrapolation process. The associated magnetic field from the large pore is observed to penetrate into the chromosphere and potentially higher, and corresponds well with the regions of increased intensity within the 30.4 nm and 17.1 nm filters, supporting that this extrapolation is reasonable over such a large height. The umbra of the two smaller pores do not appear to penetrate into the chromosphere, most likely due to insufficient magnetic flux. It should be noted, however, that UPWs patterns are still seen to propagate above the location of the rightmost pore in the Hα line core. This indicates that the magnetic field lines do still expand into the solar chromosphere. In the higher temperature filters, the clarity of the pore fades, and large-scale loop structures, co-spatial with the extrapolated field lines, can be found. On the opposite side of the pore, a region of lower emission is observed in the TR and coronal lines co-spatially with less vertically inclined field lines returned by the magnetic field extrapolation. In the following sections, we discuss the influence of the magnetic field topology on observations of UPWs within this AR. It is imperative to note, that the height of each stacked image in Figure 5.2 was estimated merely for ease of visualisation and should not, therefore, be used as strong evidence that the less vertically inclined field lines do not penetrate into the upper atmosphere.

5.3.2 Upwardly propagating waves

The main focus of this chapter is the analysis of UPWs. These events manifest as dark wavefronts, easily identified against the Hα background, which appear to propagate radially away from the large pore with a coverage angle of approximately 160°. The coverage of the UPWs is inclusive of both unstructured (such as at the north of the pore) and highly structured regions (on the east of the pore), implying that no specific magnetic topology is required in the Hα line core to facilitate the propagation of these waves. It is interesting to note, however, that no UPWs are observed to propagate either south or west from the pore during these observations, implying that a fundamental, but as of yet unknown, factor is limiting either the observation or propagation of waves in this region. A reason for the absence could be the inclination of the magnetic field (see Figure 5.2) and will be expanded upon later in this Section.

In Figure 5.3, we present a series of time-distance diagrams constructed using the white representative slit overlaid on Figure 5.1. The top row of Figure 5.3 plots the raw data extracted for this slit between 07:23:35 UT and 07:41:53 UT for the Hα line core (a), the SDO/AIA 30.4 nm filter (b), and

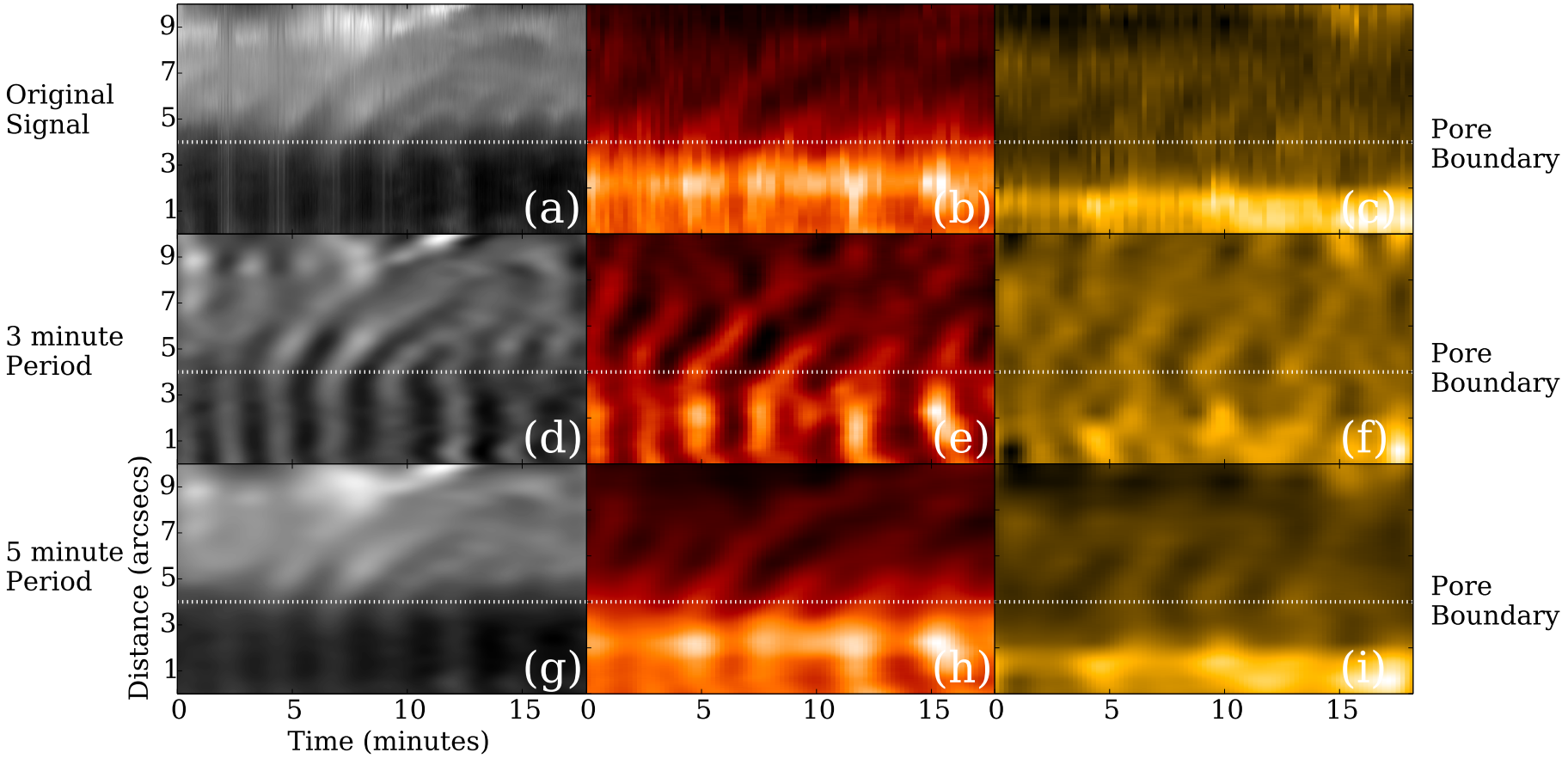

Fig. 5.3 (Top row) Unfiltered time-distance slits for the Hα line core (a), SDO/AIA 30.4 nm filter (b), and 17.1 nm filter (c) constructed for the white slit in Figure 5.1. (Middle row) Time-filtered 3-minute FFT output for Hα (d), SDO/AIA 30.4 nm (e), and SDO/AIA 17.1 nm (f). (Bottom row) 5-minute FFT output for Hα (g), SDO/AIA 30.4 nm (h), and SDO/AIA 17.1 nm (i). The windows used are centred on 3 ± 1.5 mHz (referred to as 5 minutes) and 5 ± 1.5 mHz (referred to as 3 minutes). The white dotted line is the pore boundary, below the line is the pore and above is the background chromosphere.

the SDO/AIA 17.1 nm filter (c). It should be noted that the start times for the SDO/AIA 30.4 nm and 17.1 nm filters are 9 seconds and 1 second ahead of the SST/CRISP data series, respectively. The UPWs are easily identified within the Hα line core (as dark wavefronts) and the SDO/AIA 30.4 nm filter (as bright wavefronts) propagating diagonally away from the pore between 3″ and, approximately, 8″. The apparent horizontal velocity of the observed UPWs appears to decrease as the wavefront propagates away from the source. It has been hypothesised that the decrease in speed may be explained by "the combined action of different frequency modes"(Kobanov *et al.*, 2006), i.e., that an UPW is a superposition of two or more waves with different frequencies. Within the representative Hα slit, the detected UPWs slow from 17 ± 0.5 km s^{-1} to 12 ± 0.5 km s^{-1} at distances of 4″ to 5″, respectively. To conclusively test whether the observed deceleration was a physical property of the waves or a product of using straight slits for analysis, we conducted further research of time-distance diagrams constructed using curved slits, which traced fibril structures within the Hα line core. Due to the occurrence of this deceleration in each analysed slit, we conclude that this behaviour of a reduction in apparent velocity is indeed a property of UPWs. Intuitively, as only two factors, namely the actual velocity and the angle of propagation, are required to formulate the apparent velocity, we are able to tentatively suggest that we observe either a physical slow-down of the wavefront or a change in the angle of propagation of these waves.

The spatial occurrence of these waves is a further interesting point which requires discussion. Through the analysis of each cyan slit highlighted in Figure 5.1, investigation into how the behaviour of these waves changes spatially around the pore is feasible. At distances between 2″ and 3″ away from the pore boundary (indicated by the dashed white line in Figure 5.3) for each individual slit, the apparent phase speed ranges from 10-20 km s^{-1} (*i.e.*, approximately the sound speed in the chromosphere). As UPWs are observed as single wavefronts, it is possible that the magnetic field topology is influencing the apparent horizontal velocity spatially around the pore. By overlaying the slits in which UPWs are observed onto the interpolated magnetic field, plotted in Figure 5.2, we are able to infer a spatial correlation between the apparently less vertically inclined magnetic fields and the occurrence of UPWs. The observations of such non-radially symmetric wavefronts around a pore, guided by the magnetic field, suggests that the extension of the magnetic field into the solar atmosphere from the pore, is non-axially symmetric. This result poses an interesting question: Does a combination of viewing angle and magnetic field topology limit the potential detection of propagating UPWs around the magnetic waveguide? In

order to disentangle these two effects, it would be imperative that a future analysis would combine observations and simulations to test this hypothesis.

We now direct our investigation towards understanding the potential influence of different wave modes on the raw UPW signals. By employing the FFT technique on each row of the time-distance diagrams (Figure 5.3a-c), the 3-minute period for each wavelength can be isolated from the general wave behaviour. The windows used are Gaussian shaped, centred on 3 ± 1.5 mHz (referred to as 5 minutes) and 5 ± 1.5 mHz (referred to as 3 minutes) with a width of 2 mHz.

The second row of Figure 5.3 depicts the result of such an analysis for the Hα line core (d), the SDO/AIA 30.4 nm filter (e), and the SDO/AIA 17.1 nm filter (f). The Hα 3-minute component starts off within the pore as an umbral flash-like event and, then, as the wave enters the surrounding atmosphere, moves away at a near constant speed, comparable to the raw data. It is easy to identify, that within the Hα line core 3-minute slit, the contrast of the waves against the background is increased when compared to the raw data. This suggests that the 3-minute mode provides a high proportion of the energy carried by UPWs around the pore. A similar behaviour is observed within the SDO/AIA 30.4 nm wavelength, however, no signal is isolated within the SDO/AIA 17.1 nm filter for this slit. Understanding these observations in terms of the physical properties of waves is essential to fully understand the UPW phenomena. Overall, the coverage angle, around the pore, of the 3-minute mode within the SDO/AIA 17.1 nm filter is approximately 50 % lower than the 30.4 nm filter. The question as to whether this is a result of the waves not propagating into the 17.1 nm passband or a reduced contrast against the background should lend itself to an interesting future study.

Analysis of the 5-minute period (Figure 5.3g-i) allows for further inferences about the nature of these waves to be made. Within the Hα line core, the occurrence of the 5-minute mode is limited to regions outside of the pore, potentially due to the dependence of higher frequency modes on the magnetic field inclination(De Pontieu *et al.*, 2004). The phase speed is also reduced by approximately 1-2 km s^{-1} consistently around the pore. As there is more power within the 3-minute mode close to the pore, it is assumed that this comprises the dominant component of the raw wavefront. It is possible, therefore, that the increased amplitude of the 5-minute component as the wave moves away from the pore could explain the deceleration in raw phase speed. In other words, since the 3-minute and 5-minute component travel at different phase speeds, the observational signature of UPWs is a linear combination of these two components (Jess *et al.*, 2013). Thus as one component dominates, it determines the observed phase speed and once a different component becomes

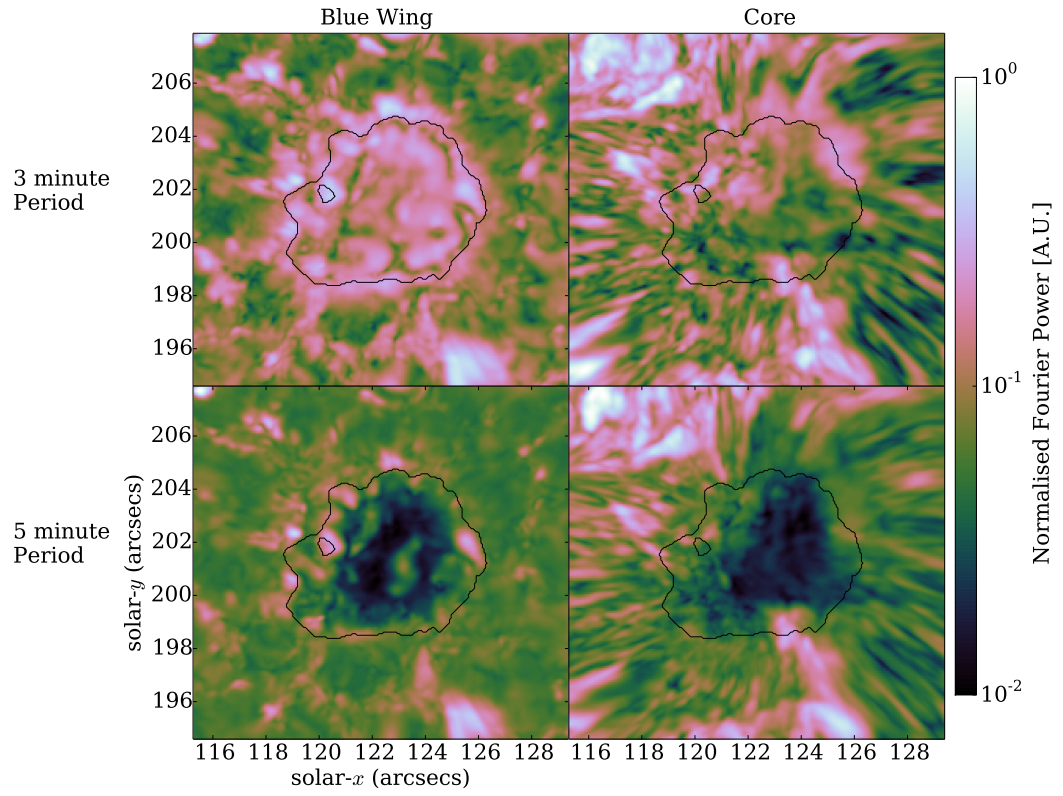

Fig. 5.4 The spatial distribution of normalised Fourier power of the LOS intensity with 3- and 5-minute filter windows. The black contour line highlights the pore boundary as observed within the Hα line wings. We depict the: (a) 3-minute filtering of the Hα wing; (b) 3-minute filtering of the Hα core; (c) 5-minute filtering of the Hα wing; (d) 5-minute filtering of the Hα core.

dominant, the observed phase speed will change. However, further research should be carried out to fully test this assertion. Within the SDO/AIA 17.1 nm filter, the 5-minute mode has a more defined wave pattern than the 3-minute mode. We are, therefore, able to suggest that the 5-minute mode more easily penetrates into the 17.1 nm passband as has been suggested by previous researchers (De Moortel *et al.*, 2002), potentially providing energy into the TR.

Another method that can be exploited to further understand the physical properties of these waves is a time-delay analysis. We were able to compare both the raw and FFT-filtered data for each wavelength in order to establish whether evidence of a lag exists. By taking into account the different start times for the SST/CRISP and SDO/AIA data, no observable lag was discernible. Therefore, we are able to conclude that either any lag between the signals is less than the cadence of these SDO/AIA data or that, indeed, no lag exists. Should the second hypothesis prove true, it would suggest that these observations support the propagation of a single wave, which occurs within the combined passbands of each of these filters, i.e., around the TR.

By expanding the FFT analysis to the full FOV, we are able to analyse how power is manifested within the local plasma. Figure 5.4 shows the result of applying a 3- and 5-minute period FFT filter on the LOS intensity for the Hα line core and far wing (−0.1032 nm). The same process was also applied to the concurrently taken SDO/AIA data, however, the obtained power maps lost their spatial structure and, as such, we were unable to make further conclusions. The black contour depicts the outline of the pore as observed in the photosphere sampled by the Hα wing. Within the photosphere (Figure 5.4a,c) the 3-minute power is isolated inside the pore structure; specifically, there appears to be large regions of power tracing the boundary of the pore, apparently analogous to the distribution of power within a sunspot (Reznikova and Shibasaki, 2012; Stangalini *et al.*, 2012). The power in the 5-minute band is minimal in the body of the pore but there is an increase at the pore-photosphere transition boundary corresponding to enhanced p-mode power (Mathew, 2008). We interpret the confinement of the power at the pore boundary as evidence that p-modes are absorbed by the pore and the author speculates that this power drives MHD waves within the pore which acts as a magnetic waveguide.

Finally, we are able to analyse the Hα line core. The increase of power especially within the 3-minute, easily observed to the north-east of the pore, corresponds well with the occurrence of UPWs within these data. It is intuitive to suggest that, as the FFT analysis is only applied in the vertical direction, the horizontal component of the UPWs in these regions limits the detection of power. Potentially, the increase in the FFT power observed to the north of the pore, could be indicative of the propagation of UPWs into the upper solar atmosphere along more vertically inclined magnetic field lines (as observed within Figure 5.2). We interpret the lack of power co-spatially with the UPWs (in the east) as further evidence that the pore's magnetic field has become non-symmetric in the chromosphere. Evidence of the apparent dependence of both the observation of UPWs and the localised power within the plasma around a pore on the potential magnetic field topology, as presented within this chapter, is a key step in fully understanding the complex nature of coupling between layers of the solar atmosphere.

5.3.3 Energy of UPWs

Following the identification and detailed analysis of UPWs around a pore, it is essential to estimate the potential energy carried by these waves into the upper solar atmosphere. Due to the decrease and increase in intensity in comparison to the background plasma for the Hα line core and the SDO/AIA filters, respectively, it can be inferred that the wavefront represents an increase

in density (Allen, 1947; Leenaarts *et al.*, 2012). By measuring the contrast between the background plasma and the wavefronts, as this ratio is not >25%, it is apparent that the intensity perturbations are within the linear regime. As these waves follow field lines and change the observed intensity, this waves appear to be magnetoacoustic in nature. In order to further this analysis, we assume here that the lack of observed time-delay in these data implies that the lag is below the cadence of these data. Given estimated formation height-differences between the chromospheric Hα line core and the SDO/AIA 30.4 nm filter can be estimated to be around 0.5 ± 0.25 Mm, the upward propagation speed can be calculated as 42 ± 21 km s^{-1}. This speed is close to previous estimates of the fast speed in the chromosphere (Morton *et al.*, 2012). It should be noted, that this corresponds well with previous results, which suggest that *p*-mode oscillations, which appear to drive these UPWs, are converted to fast modes (Vigeesh *et al.*, 2012). The combination of these factors allows us to suggest that one of the most likely interpretations of these observations is that UPWs are *fast MHD sausage* waves.

With the wave type being identified, it is now possible to calculate the estimated non-thermal energy for these waves. It is possible to estimate the energy flux at each pixel based on linearised MHD theory (e.g. Kitagawa *et al.*, 2010). The equation for the total energy flux of the fast MHD sausage wave is,

$$E_{wave} = \sum_{i=1}^{N} \rho_0 [\tilde{I}_i / I_0]^2 c_{ph}^3, \tag{5.1}$$

where $\tilde{I}_i$ is the intensity perturbation for each pixel, I_0 is the background intensity, c_{ph} is the phase speed of the sausage wave, ρ_0 is the background density. It should be noted that the filter passband was not taken into account. We sum over each pixel which is part of the wave, giving us the average energy for that wave. Since the wave is a fast MHD sausage wave, the phase speed is c_{fast} which is the local fast speed, however, since the ratio of the Alfvén to the sound speed is >> 1, the Alfvén speed is the dominant value in the fast speed calculation. This assumes that the plasma is optically thin (intensity is proportional to density), which is true for the coronal lines however, not the case for Hα. For Hα this means that the intensity could be affected by changes in temperature or opacity effects, which implies that assumption would be the maximum limit.

This analysis leads to energy estimates of the order of 150 W m^{-2} for the wavefronts in the Hα line core. These values drop by two orders of magnitude within the SDO/AIA filters. The reason for this is unclear; one potential reason is that SDO/AIA uses broader filters, compared to SST/CRISP, which lowers

the contrast and thus will lower the calculated wave energy. To investigate this point would require IRIS observations that avoid this issue. These energy flux values are about a factor of 100 less than reported for other abundant sausage wave events in the chromosphere (Morton *et al.*, 2012), however, they still comprise a important fraction of the energy flux required to heat the local quiet (Wedemeyer-Böhm *et al.*, 2012) and active corona (Aschwanden *et al.*, 2007), respectively. It should be noted, that these estimates are influenced by a number of observational factors, such as attenuation in the telescopic apparatus, changes in light levels throughout these data, and the angle of observation, to name a few. We do, however, suggest that during the period of these observations, there are approximately constant seeing conditions and, therefore, these energy estimates should be consistent. pores cannot heat the entire corona, but can contribute to heating the local corona that is above and near the pore. The value for the energy flux is for the region where we can observe the UPWs and the most logical case is that UPWs occurs across the entire pore but are difficult to observe due to the local solar atmosphere. This should raise the value for the energy flux that has been obtained.

5.4 Conclusions

The results presented in this chapter support the assertions that waves propagating radially away from concentrated magnetic waveguides (such as pores and sunspots) in the solar photosphere have significant vertical components that give rise to the illusion of horizontal propagation. The magnetic field reconstruction (as seen in Figure 5.2) gives us a useful insight into the non-radially symmetric nature of this pore and, specifically, how the apparent topology of the magnetic field influences UPWs. The case that RPWs are in fact UPWs that travel along the field lines is mounting (Bloomfield *et al.*, 2007; Jess *et al.*, 2013). Here, strong evidence is presented that energy from p-modes in the lower solar atmosphere travels directly upwards into the TR and lower corona. It has been reported that there is absorption of power at the boundary of the umbra-penumbra for a sunspot (e.g. Gosain *et al.*, 2011). Here, we observe enhanced power at the boundary of the pore at both three and five minutes, while in the chromosphere, where UPWs are observed, there is a reduction of power. As the energy from the acoustic p-modes is converted into MHD waves along the flux tube, the period of the p-mode becomes three minutes and traces the magnetic field. When the wave travels into the TR and solar corona, there is decrease of the wave period. Rudimentary energy flux calculations reveal that these waves are able to contribute to heating the local corona, however, how much they contribute requires further study.

From this primarily wave-based study of the solar atmosphere we deduce that, in the outside environment surrounding the pore, the magnetic field of the pore becomes non-symmetric. The non-symmetric magnetic field appears to be integral in allowing UPWs to be observed, however, whether these events occur in other regions around the pore but are undetected, requires further study. Further investigation is also required to fully assess whether the lack of UPW signal within some regions around the pore is a consequence of seeing or an, as of yet unascertained, physical property (such as the cut-off frequency). A possible interpretation of these waves is a singular wavefront observed in multiple pass bands, data from a wider range of sources should help answer these. This calls for an extensive investigation using detailed spectropolarimetry (ground-based) data to resolve the issue but also to determine the consequence of changing the LOS (i.e on the limb) on the observation of UPWs. We have shown that the complex lower solar atmosphere, which does act as a powerhouse in the heating of the outer atmosphere, can in fact be further understood through a purely wave-based investigation.

Chapter 6

Conclusion

6.1 Overview of the thesis

In this thesis, the results of a two-dimensional image analysis of sunspots and pores observed in the lower solar atmosphere is detailed. These results are directly compared to theoretically derived phase relations and these indicate the ubiquitous presence of slow MHD sausage waves in the larger magnetic structures that inhabit the solar surface.

In Chapter 2, the telescopes and their associated instruments that supplied the science ready datasets are described. Then the signal analysis methods used to determine the periods and phase difference are detailed. These being the Fast Fourier Transform (FFT), Wavelets and Empirical Mode Decomposition (EMD). Finally, the method used to measure the cross-sectional area and total intensity of magnetic structures is examined. The reason for this is to understand what the effects of varying the sigma multiplier has on the results of the signal analysis. This is important to know before this method is used to analyse datasets.

In Chapter 3, the cross-sectional area and total intensity is measured for two sunspots and one pore. By comparing the phase difference between the cross-sectional area and total intensity signals, which are calculated using the method described in Chapter 2. It was possible to find the ubiquitous presence of slow MHD sausage waves within these magnetic structures. This conclusion is reached because the measured phase difference was very close to 0°, i.e., they were in phase. This is the signature of the slow MHD sausage wave within cylindrical magnetic flux tubes.

In Chapter 4, the cross-sectional area and total intensity is calculated for two new pore datasets and the phase difference indicated that the oscillations are slow MHD sausage waves. The usage of magneto-seismology equations allowed the calculation of several properties of the detected oscillations. These are, the radial distance perturbation, radial velocity perturbation and magnetic field perturbations. The properties of these oscillations give the impression of standing harmonics. However, it was possible to use magneto-seismology to demonstrate that these oscillations are in fact standing harmonics. This was accomplished by working out if density stratification or radial expansion of the flux can cause the observed period ratios. The calculated radial expansion is in good agreement with previous MHD simulations and observations.

In Chapter 5, the focus shifted from analysing the cross-sectional of magnetic structures to the analysis of Running Penumbral Waves (RPWs) in a pore. RPWs have only observed in sunspot penumbras; however, RPW-like events were observed, for the first time, to occur around a pore. This observation is the final step in confirming that RPWs are a visual effect of MHD sausage waves

travelling along magnetic field lines of sunspots and pores. These have been previously termed Upwardly Propagating Waves (UPWs). This visual effect is caused because the magnetic field becomes more radially inclined further from the umbral centre. These radially inclined fields have longer arc lengths and as these MHD waves follow these field lines, they travel a larger distance before they appear in the chromosphere. This creates a delay of the appearance of these waves at higher levels, causing this patten of radially outward propagating waves. These events are able to deliver a small amount of energy into the local corona, but not enough to heat the active corona.

6.2 Summary of results

6.2.1 Chapter 2

Chapter 2 started by detailing the various solar telescopes, space- and ground-based utilised. It covered the instruments that are either on board the space-based telescopes or attached to an optics bench for ground-based telescopes. From here, the three signal analysis methods employed are described: FFT, Wavelets and EMD. It detailed how each method works, strengths and weakness and why three methods were used instead of just one.

The chapter finishes on a study of the principle method that is used to measure the cross-sectional area of the sunspots and pores analysed. The motivation was to understand if the method output was heavily affected or dependent on the sigma multiplier value chosen. If this was the case, then this had to be known before this method could be used for any scientific analysis. In order to undertake this study, high-quality ground-based data was used from the Dunn Solar Telescope (DST). The instruments used from the DST are the *Interferometric Bidimensional Spectrometer* (IBIS) and the *Rapid Oscillations in the Solar Atmosphere* (ROSA) instrument. There are two datasets, one for each instrument, with the telescope pointed at a sunspot and a pore for IBIS and ROSA, respectively. These can be seen in Figure 2.5 and are a good representative of the datasets studied within this thesis.

The sigma value used comes from a background box of quiet Sun, i.e., a region of the photosphere that contains no magnetic features. Once the sigma value is calculated, it is multiplied by a value which is called the sigma multiplier. Both magnetic structures were contoured using a selection of sigma multipliers, 3, 3.5, 4, and 4.5 and 2, 2.5, 3, and 3.5 for the sunspot and pore respectively. This contouring is displayed in Figure 2.6 and these values correspond to the colours: blue, green, purple and orange. The reason for difference in sigma multipliers between the sunspot and pore is due to the lack of a good quiet Sun

region within the IBIS dataset. This is clearly seen in the top right histogram in Figure 2.6, where the returned distribution is skewed, and this had the result of increasing the sigma multipliers.

The resultant cross-sectional area signals are analysed using the wavelet transform and this revealed a range of periods within these magnetic structures. For the IBIS sunspot, the range of sigma multipliers did not alter the periods found by the wavelet transform. What did vary was the wavelet power of the periods, as seen in Figure 2.7. The range of sigma multipliers return a threshold value that contours pixels which encompass the sunspot umbra and not the penumbra or background photosphere and is why the sigma multiplier has little effect on the output in this case. For the ROSA pore, the difference in multipliers is more important. Figure 2.8 demonstrates that for the larger sigma multipliers, the smaller periods have disappeared from the wavelet transform. This is because the threshold value from the higher sigma multiplier under contours the pore. As a result, the returned cross-sectional signal is missing a large number of pixels, which can be seen in the signals at the top of Figure 2.8.

The results can be summarised as the following. The most ideal way to choose a sigma multiplier, is to take into account the structures's intensity distribution. This way choosing a sigma multiplier becomes more straightforward and more robust than choosing a threshold value this is a percentage of the quiet Sun intensity. So as long as the sigma multiplier is sane, then there will be nothing missed from an analysis.

Finally, the phase relations are used to identify the various MHD wave modes and these are listed in Table 1.2. All three signal analysis methods offer the ability to calculate the phase of each signal and this allow the direct comparison of the cross-sectional area phase to the total intensity phase. For this analysis, the wavelet transform was used to check the phase difference between the cross-sectional area and total intensity, which can be seen in Figures 2.9 and 2.10 for the IBIS sunspot and ROSA pore, respectively. Overall, the periods show in phase behaviour within these two magnetic structures which indicates slow MHD sausage modes. The cross-wavelet phase images show that there is no effect due to the different sigma multipliers. Thus regarding MHD wave mode identification, there is no dependency in this case. It should be noted that this study does not cover every aspect and this is discussed later on.

6.2.2 Chapter 3

Chapter 3 detailed the application of the method, described previously in Chapter 2, to three magnetic structures: two sunspots and one pore. These

datasets came from two ground-based solar telescopes: the Dutch Open Telescope (DOT) and the Swedish Vacuum Solar Telescope (SVST) and are shown in Figure 3.1. These telescopes were covered in Chapters 2 and 3 and while these telescopes are now out of service, they offered very good datasets during their lifetimes.

Using a sigma multiplier of 3 to contour these magnetic structures resulted in the cross-sectional area and total intensity signals. Both the wavelet and EMD were employed to identify periods within these datasets and they revealed a range of periods within each magnetic structure's cross-sectional area and total intensity signals. These can be seen in Figures 3.3 and 3.4, 3.5 and 3.6, 3.7 and 3.8, for the sunspot observed with the SVST, the sunspot and the pore observed with the DOT respectively. The periods found ranged from 2 to 40 minutes and many of the cross-sectional area periods had a corresponding total intensity period. Furthermore, a comparison of the cross-sectional area periods with line-of-sight (LOS) intensity oscillations that have been found in sunspots demonstrates similar periods (Kobanov and Makarchik, 2004). However, if they are linked or a different manifestation of the same MHD wave has yet to be established.

The phase difference between the cross-sectional area and total intensity was calculated to be close to 0°, from both the wavelet and EMD analyses. Using the phase relations from Table 1.2 indicates that the observed oscillations are slow MHD sausage waves. This implies that there is a prevalent amount of slow MHD sausage waves within these magnetic structures which are located in the photosphere. In addition, there were small regions of out of phase and ±45 degree behaviour. The out of phase behaviour indicates a fast MHD sausage wave, however this behaviour was not consistent and thus was ignored. The ±45 phase difference is more difficult to explain. While there is no current MHD theory that explains this phase difference, it has been shown that noise in a signal can cause the cross-wavelet phase to become shifted by ±45 degrees (Moreels *et al.*, 2015a). This would be one reason why the wavelet transform would need to be cross-checked with another signal analysis method. However, it should be noted that in Moreels *et al.* (2015a), the artificial signal had a very low signal to noise ratio, which is not generally the case with solar observations.

Finally, whether these oscillations are propagating or standing waves is still an open question. Since it is not possible to distinguish between propagating or standing waves using only the cross-sectional area and total intensity phase relations. It would require another observable quantity. It has been previously suggested that these oscillations are standing oscillations (Morton *et al.*, 2011). To this end, Table 3.1 lists the discovered periods and their corresponding period ratios, if these oscillations are harmonics. In order to calculate these

period ratios, it was assumed that the largest period within that dataset was the fundamental mode. Furthermore, Table 3.1 lists the period ratios in the ideal homogeneous flux tube case. Thus, by comparing these values to the observed period ratios, gives additional momentum, that these oscillations are standing harmonics; however, further investigation is required.

6.2.3 Chapter 4

Chapter 4 expands on the previous work undertaken in Chapter 3 by studying two further pores. These two new datasets come from the DOT and the DST using the ROSA instrument, which offers an increase in spatial resolution and a decrease in cadence from the datasets studied in Chapter 3. These two datasets can be seen in Figure 4.1 and the cross-sectional area and total intensity of each pore is calculated by the method previously used in Chapters 2 and 3. Both pores display a collection of oscillations but due to the shorter length of these datasets, the maximum periods found were shorter. The periods range from 2 to 20 minutes and the resultant wavelet transforms can be seen in Figures 4.2 and 4.3. The phase difference between the cross-sectional area and total intensity signals show that these oscillations are slow MHD sausage waves.

The extension within this chapter is utilisation of the perturbation amplitude of these oscillations. Using linear ideal MHD theory, it is possible to derive equations that will calculate the the ratio of magnetic field perturbation to the background magnetic field as well as the radial displacement and radial velocity perturbation of these oscillations and are Equations 4.14, 4.15, and 4.16, respectively. To calculate these quantities, the amplitude of the oscillations was required and the EMD was used to provide the amplitudes. The IMFs returned from the EMD algorithm are known to return close to the actual amplitude of the original frequency components. To make sure this was accurate, these values were compared with the FFT output and were in good agreement. It should be noted that the wavelet transform can not be used to work out perturbation amplitudes because the power spectrum is biased towards lower frequencies and thus must be normalised (Liu *et al.*, 2007).

For the DOT pore, the amplitudes for the cross-sectional area oscillations are measured to be $3.87\text{x}10^5$, $3.61\text{x}10^5$ and $5.90\text{x}10^5$ km^2 for the oscillations with periods of 4.7, 8.5 and 20 minutes, respectively. The radial perturbation was calculated to be 37, 34, and 56 km and the radial velocity perturbation was calculated to be 0.82, 0.42, and 0.29 km s^{-1}. The obtained radial speeds are sub-sonic, however, they are of order of observed horizontal flows around pores. Furthermore, the percentage change in the magnetic field was to be found 4-7% which was found for another pore observed with DST/IBIS (Grant *et al.*, 2015).

Finally, the wavelength of the oscillations are calculated but it requires the phase speed of the wave to be known. As the oscillations have been identified as the slow MHD sausage mode, the phase speed in a photospheric tube was calculated to be 5.2 km s^{-1} using a background sunspot atmosphere model. The obtained estimate of the wavelength for these oscillations was 1269, 2268 and 5319 km.

For the ROSA pore, the amplitudes for the cross-sectional area oscillations are measured to be 2.29x10^5, 2.45x10^5, and 3.87x10^5 km^2 for periods of 2-3, 5.5, and 10 minutes, respectively. The radial perturbation amplitude was calculated to be 69.1, 74.2, and 117 km and the radial velocity perturbation as 3.03, 1.41, and 1.23 km s^{-1}. The percentage change in the magnetic field was found to be 25-45% and is much larger than the DOT pore and should be measurable in future observations. For this dataset, there was no corresponding magnetogram and as a result this effect could not be verified. This suggests that the oscillation strength might be independent of the scale of the structure (Dorotovič *et al.*, 2014). Finally, the calculated wavelength was 540-810, 1485, and 2216 km. A summary of these findings can be found in Tables 4.1 and 4.2.

The calculated wavelengths are further evidence for standing harmonic oscillations within magnetic flux tubes in the photosphere. To show this, if the assumption that these are standing harmonics is taken, magneto-seismology can be used to prove or disprove this assumption. This is possible because magneto-seismology allows the calculation of two important background properties of magnetic flux tubes. The first is density stratification, which is the ratio of the density at the top of the flux tube to the bottom of the flux tube. The second is the expansion factor (Γ), which is the ratio of the radius at the top of the flux tube to the bottom of the flux tube. These are Equations (4.18) and (4.17) and the period ratio between the fundamental and first harmonic is the output value from these equations. It should be noted that these flux tubes are photospheric flux tubes that start at the photosphere and end at the transition region. Table 4.3 lists the period ratios of the observed oscillations for the two pores within this chapter. Furthermore, period ratios from Chapter 3 are used for this analysis.

For density stratification, three density models were used: VAL-III C, sunspot umbra and magnetic bright point which come from Vernazza *et al.* (1981), Maltby *et al.* (1986) and Gent *et al.* (2013, 2014), respectively. The resulting period ratio from these three models are 1.44, 1.38 and 1.41 and these values do not correspond well to the results presented in this chapter. It can be concluded that density stratification does not seem to be applicable for the cases presented here.

For the expansion factor, Equation (4.17) was solved for a range of expansion factors and plasma-β values, which can be seen in Figure 4.4. For the results within this chapter, the flux tube has to expand four to six times to have the period ratios that are observed. When compared to a number of MHD numerical simulations that model flux tubes and an observation of a coronal loop, there is good agreement with these results (Fedun *et al.*, 2011a,b; Khomenko *et al.*, 2008; Kontar *et al.*, 2008). This result demonstrates that these oscillations are standing harmonics that are supported between the photosphere and transition region within sunspots and pores.

6.2.4 Chapter 5

Chapter 5 shifts the focus from the cross-sectional area analysis of sunspots and pores to the investigation of Running Penumbral Waves (RPWs). RPWs have been observed within sunspot penumbras since the 1970's as intensity fronts propagating radially outwards from the outer umbra into the penumbra, before disappearing at the penumbra photosphere boundary. To study RPWs, ground-based data from the Swedish Solar Telescope's (SST) *CRisp Imaging SpectroPolarimeter* (CRISP) instrument was combined with co-aligned and co-temporal data from the *Atmospheric Imaging Assembly* (AIA) instrument on board the Solar Dynamics Observatory (SDO) satellite. An overview of the ground- and space-based data can be seen in Figure 5.1 and the focus was on a small active region (AR) containing two pores. The first pore had a light-bridge through the middle and it could not been seen in the chromosphere. The second pore was the target for this observation and it was larger than the first pore and can be seen clearly in the chromosphere. Wideband and white light images from the SST and SDO, respectively, showed that these pores had no penumbral structure in the photosphere.

By focusing on the chromosphere around the two pores, RPW-like events could be seen to emanate clearly from the larger pore. It was also noted that despite the smaller pore not being able to penetrate into the chromosphere, RPW-like waves could be seen to from the chromosphere above it. To confirm if these were RPWs, a slit analysis was performed around the larger pore in order to find out the periodicity and speed of these RPW-like events. One example of this slit analysis can be seen in Figure 5.3 and the result of that slit analysis is as follows. The periodicity and speed of these RPW-like events are consistent with RPWs observed around sunspots. These events do not emanate concentrically around the pore as commonly happens with sunspots. The RPW-like events are confined to a small arc, the regions of the chromosphere which are not dominated with dynamic fibrils or large static fibrils. It has

been hypothesised that RPWs are an optical illusion caused by a delay in the appearance of MHD waves that travel along magnetic field lines and they have been termed Upwardly Propagating Waves (UPWs, Bloomfield *et al.* 2007). If this was the case for the wave events observed here, understanding how the magnetic field behaviours around this pore is important. Figure 5.2 shows the output of a magnetic field extrapolation code called MPole (Longcope, 1996; Longcope and Klapper, 2002), which used magnetograms from the *Helioseismic and Magnetic Imager* (HMI) on board SDO as a source. It offers evidence that where the RPW-like events are observed, the magnetic field is significantly more radially inclined which is a requirement in order to observe RPWs if they are UPWs. This result is the first direct imaging of RPWs in a pore in the Hα line core and confirms that RPWs are in fact UPWs.

Furthermore, these UPWs are observed in two SDO/AIA ion lines, 30.4 and 17.1 nm, that are formed in temperatures that correspond to the transition region and low corona. This suggests that UPWs are able to reach the hotter regions of the solar atmosphere, which is consistent as various MHD wave phenomena have been observed in the corona above sunspots previously. Finally, it was found that the UPWs are most likely a superposition of MHD waves that have different dominant periods and was discovered previously for RPWs observed around a sunspot (Jess *et al.*, 2013).

As RPWs became under heavy investigation, the identification of the MHD wave type become important topic and the current literature indicates that RPWs are slow magnetoacoustic waves (Bloomfield *et al.*, 2007). To identify the wave type for the UPWs observed in this chapter, the phase speed needs to be measured. A time lag analysis between the Hα slit and the SDO/AIA slits was attempted and returned a result of less than 12 seconds, i.e., the lag is less than the cadence of SDO/AIA. The best assumption that can be made is that the lag is 12 seconds. It should be noted that this lag could actually be 0 seconds. This would imply that Hα and the two SDO/AIA ion lines have a temperature response, at least partially, within the same temperature range and thus this observation is of UPWs in three different wavelengths at the same time. To confirm if this the case would require a future study with an expanded dataset that consisted of ground and several space telescope observations.

Using the highest cadence gives the lower limit of the estimated phase speed, which is 42 ± 21 km s^{-1}. This speed is greater than the sound speed in the chromosphere which is estimated to be around 10 km s^{-1} (Morton *et al.*, 2012) and is greater than the local Alfvén speed. Thus the phase speed indicates that this is a fast magnetoacoustic wave and not a slow magnetoacoustic wave that RPWs and UPWs are thought to be. This is the first reported observation that suggests that RPWs/UPWs are a fast MHD wave.

Finally, as the MHD wave type has been identified, it becomes possible to calculate the energy of these UPWs. Using Equation (5.1) which uses the perturbation intensity and phase speed of the wave (Kitagawa *et al.*, 2010), the energy of the UPWs was calculated to be around 150 W m^{-2} in the chromosphere and 1 W m^{-2} in the transition region and corona. This value is enough to supply the majority of the energy needed to heat the quiet Sun corona. However, it is a factor of 10 less than the energy required to heat the corona around an AR. It was previously found that the wave energy for cross-sectional area oscillations at lower chromospheric heights is of a similar value (Grant *et al.*, 2015). When compared to other fast MHD wave energies measured within the chromosphere, it is a factor of 100 less (Morton *et al.*, 2012). Overall these waves play a small role in supplying energy to the corona, assuming a mechanism of dissipation, but this study has helped to reveal that RPWs are UPWs.

6.3 Future work and questions

Within this thesis, many interesting MHD wave phenomena have been discovered and discussed. However, as one question is answered, further questions arise regarding these MHD waves. Here, the questions regarding the work presented within this thesis and the regions that can be expanded upon in the future will be detailed. This will be split into two parts: Methods and Science.

6.3.1 Methods

To begin, in Chapter 2 the signal analysis methods used to analyse signals in order to measure the period and phase of a signal are described. Overall, they were used successfully to achieve the scientific goals within each chapter. However, the field of signal analysis is fast moving and many papers are published either suggesting improvements to current methods or offering new methods. The wavelet transform has had several extensions suggested to the core algorithm. For example, it was discovered that there is a power bias towards lower frequencies within the outputted spectrum (Liu *et al.*, 2007; Veleda *et al.*, 2012). Furthermore, a modified version wavelet transform has been developed that is able to discern if the input signal is made up of standing or propagating components (Sych and Nakariakov, 2008). The EMD has been extended, adding a further step to the algorithm where an ensemble approach is undertaken in order to improve the outputted Intrinsic Mode Functions (IMFs Wu and Huang 2009). Other improvements are on how to deal with the edge effects associated with the spline fitting (Zeng and He, 2004) and improved stopping criterion

(Huang and Wu, 2008). Recently a new method has been created called the Variational Mode Decomposition (VMD, Dragomiretskiy and Zosso 2014). It has a mathematical framework that underpins the decomposition, as do the FFT and wavelet transform. The EMD algorithm lacks this framework and preliminary results suggest that it is more robust to sampling and noise effects than EMD. It is important that improved signal analysis methods are employed within solar physics as more complex signals are interpreted within the literature (Sych and Nakariakov, 2014). Furthermore, the magneto-seismology equations used in Chapter 4, require the amplitude of the perturbation and as a result, any method that is more robust to noise should be used as the perturbation amplitude will directly affect any scientific results.

Finally, at the end of Chapter 2 was an analysis of the method used to measure the cross-sectional area and total intensity of sunspots and pores. To extend this study, it is important to look at the effect of light level change during an observation sequence and if a pure intensity oscillation would result in a false detection of a cross-sectional area oscillation. Theoretically, a pure intensity oscillation would result in a cross-sectional area oscillation due the usage of a fixed sigma multiplier. This is because, if the intensity oscillation is higher, a larger cross-sectional area will be measured compared to when the intensity oscillation is lower and thus a smaller area would be measured. An artificial dataset that models a basic sunspot or pore could be constructed to study these effects in the future. Until then, how likely there will be a cross-talk between the cross-sectional area and total intensity signals is unknown.

6.3.2 Science

Within Chapter 2, it was shown that a high sigma multiplier would under estimate the cross-sectional area of a pore. The end result, after signal analysis, was that certain periods had vanished within that signal. This means that it might be possible to isolate the regions where the pore oscillates and could provide an insight into if the magnetic structure is a monolithic or polylithic (Parker, 1979).

Each study that analysed how the cross-sectional area of sunspots and pore changes with time used datasets collected with a G-band filter which samples the lower photosphere (<250 km). The first extension to these studies would be utilising a broader range of wavelength filters that are available on ground-based telescopes. For example, Fe I 630.26 nm, Na D 589.70 nm, and Ca II 854.16 nm filters sample the lower photosphere (~50 km), mid-photosphere (~450 km) and mid-chromosphere (~1000 km), respectively. This would allow a study into how the cross-sectional area and total intensity vary as a function

of height for a sunspot or pore. The main issue with a study like this is that the boundary between the sunspot or pore and the background atmosphere becomes less distinct in the higher formation lines. As a result, defining this boundary becomes a non-trivial problem that further complicates any method that measures the cross-sectional area.

Furthermore, atmospheric effects during a ground-based observational sequence can heavily affect the quality of the data and introduce artefacts (Moreels *et al.*, 2015a). To counteract this, moving to space-based telescopes would remove the Earth's atmosphere. While SDO does not offer a high enough resolution to observe these cross-sectional area oscillations, Hinode as well as NASA's Interface Region Imaging Spectrograph (IRIS) telescope could be used to study these oscillations. Both satellites are able to observe the photosphere and wavelengths that sample the higher regions of the solar atmosphere. Combining all of these into one comprehensive dataset would enable a highly detailed study of a sunspot or pore from the photosphere to the transition region and corona.

In Chapter 4 the phase speed of the observed MHD waves was calculated using typical background plasma properties and not from any observational quantity. To measure the phase speed normally would require a multi-height analysis, as detailed above, by calculating the time lag between the signal at different heights. Recently, Moreels *et al.* (2015a) detailed a theoretical MHD framework that would return a phase speed for any observed MHD wave by using the perturbation amplitude of the oscillation which could be verified by observations. Added to this, Moreels *et al.* (2015b) extended the previous MHD framework to calculate the energy of an observed MHD sausage wave using the phase speed and amplitude of that wave. With all of this information, it would be possible to understand if MHD waves that perturb the cross-sectional area of sunspots and pores are important within the solar atmosphere.

The current range of ground-based and high-resolution space-based solar telescopes have approximately the same spatial resolution. This puts a upper limit on the size of perturbations that can be measured for the cross-sectional area of sunspots and pores. There are two reasons why spatial resolution is important. Firstly, as discussed in Chapter 1, the slow MHD surface mode has a lower amplitude when compared to the other MHD wave modes and with current capabilities it is impossible to observe. Secondly, Moreels *et al.* (2015a) using an artificial sunspot dataset showed that due to sub-resolution perturbations, the thresholding routine did not correctly detect the contraction of the sunspot and that the magnitude of the cross-sectional area perturbation had been under estimated by a factor of two. So an increase in spatial resolution will reduce these effects during an analysis. With Daniel K. Inouye Solar Tele-

scope (DKIST) becoming operational within the next 5 years, will significantly increase the spatial resolution of ground-based solar data. Hopefully, Japan Aerospace Exploration Agency's (JAXA) Solar-C satellite and the European Space Agency's (ESA) European Solar telescope (EST) will join DKIST within the next decade.

Finally, the observed UPWs within the pore discussed in Chapter 5, offer an interesting avenue for MHD wave research. Here, there are many unanswered questions which require an expanded dataset that has more spectral information. To begin, the observation indicated that these UPWs were fast sausage modes which is in opposition with the current literature (Bloomfield *et al.*, 2007; Jess *et al.*, 2013). There are two answers to this problem; either the analysis presented in Chapter 5 is incorrect or the analysis is correct and UPWs can either be fast or slow MHD sausage waves. The second case would lead to further insights into magnetic structures, as currently UPWs in sunspots are slow MHD sausage waves while in this pore they are fast MHD sausage waves. This could be due to differing magnetic field geometries or background plasma properties. For example, does the presence of the penumbra cause this difference or does the plasma-β vary such that mode conversion leads to a slow MHD sausage wave instead of a fast MHD sausage wave?

Generally symmetrical sunspots display concentric and clear RPWs, but is that due to the magnetic field of the sunspot able to dominate the surrounding atmosphere unlike the pore in this case? The region that displayed clear UPWs for the pore, was a small region of quiet chromosphere where the magnetic field was radially inclined. Thus do the observations of UPWs allow the observer to infer the magnetic field topology around sunspots and pores? This can be verified with a more complex magnetic field extrapolation code than the one used in Chapter 5. Finally, do UPWs have a common source with the LOS oscillations and cross-sectional area oscillations observed in these magnetic structures, or are they the same phenomena that is observed in several different ways due to the non-homogeneous background plasma properties? Ground-based observations of sunspots and pores would need to be conducted in order to understand how UPWs vary within these structures. This can be coupled with full-Stokes polarimetric measurements of Ca II 854.2 nm spectral line and Fe I 630.2 nm which would allow the computation of the background density and temperature of the photosphere and chromosphere using the NLTE Stokes Synthesis/Inversion Code (NICOLE Beck *et al.* 2015; Socas-Navarro *et al.* 2015).

While the Sun still offers more questions than answers; new analysis methods, faster simulations and higher resolution observations provide more ways to find answers to the questions presented here.

References

Alfvén, H., 1942, "Existence of Electromagnetic-Hydrodynamic Waves", *Nature*, **150**, 405–406. [DOI], [ADS].

Allen, C. W., 1947, "Interpretation of Electron Densities from Corona Brightness", *Monthly Notices of the Royal Astronomical Society*, **107**, 426. [ADS].

Andries, J. and Cally, P. S., 2011, "On the Dispersion and Scattering of Magnetohydrodynamic Waves by Longitudinally Stratified Flux Tubes", *The Astrophysical Journal*, **743**, 164. [DOI], [ADS].

Andries, J., Arregui, I. and Goossens, M., 2005a, "Determination of the Coronal Density Stratification from the Observation of Harmonic Coronal Loop Oscillations", *The Astrophysical Journal, Letters*, **624**, L57–L60. [DOI], [ADS].

Andries, J., Goossens, M., Hollweg, J. V., Arregui, I. and Van Doorsselaere, T., 2005b, "Coronal loop oscillations. Calculation of resonantly damped MHD quasi-mode kink oscillations of longitudinally stratified loops", *Astronomy & Astrophysics*, **430**, 1109–1118. [DOI], [ADS].

Andries, J., van Doorsselaere, T., Roberts, B., Verth, G., Verwichte, E. and Erdélyi, R., 2009, "Coronal Seismology by Means of Kink Oscillation Overtones", *Space Science Reviews*, **149**, 3–29. [DOI], [ADS].

Aschwanden, M. J., 2004, *Physics of the Solar Corona. An Introduction*, Praxis Publishing Ltd. [ADS].

Aschwanden, M. J., 2006, "Coronal magnetohydrodynamic waves and oscillations: observations and quests", *Royal Society of London Philosophical Transactions Series A*, **364**, 417–432. [DOI], [ADS].

Aschwanden, M. J., Fletcher, L., Schrijver, C. J. and Alexander, D., 1999, "Coronal Loop Oscillations Observed with the Transition Region and Coronal Explorer", *The Astrophysical Journal*, **520**, 880–894. [DOI], [ADS].

Aschwanden, M. J., Winebarger, A., Tsiklauri, D. and Peter, H., 2007, "The Coronal Heating Paradox", *The Astrophysical Journal*, **659**, 1673–1681. [DOI], [ADS].

Astropy Collaboration, Robitaille, T. P., Tollerud, E. J. et al., 2013, "Astropy: A community Python package for astronomy", *Astronomy & Astrophysics*, **558**, A33. [DOI], [ADS], [arXiv:1307.6212 [astro-ph.IM]].

Balthasar, H., 1999, "Temporal fluctuations of the magnetic field in sunspots", *Solar Physics*, **187**, 389–403. [DOI], [ADS].

Balthasar, H., Collados, M. and Muglach, K., 2000, "Oscillations in a solar pore", *Astronomische Nachrichten*, **321**, 121–127. [DOI], [ADS].

Banerjee, D., Erdélyi, R., Oliver, R. and O'Shea, E., 2007, "Present and Future Observing Trends in Atmospheric Magnetoseismology", *Solar Physics*, **246**, 3–29. [DOI], [ADS].

Basu, S., Chaplin, W. J., Elsworth, Y., New, R. and Serenelli, A. M., 2009, "Fresh Insights on the Structure of the Solar Core", *The Astrophysical Journal*, **699**, 1403–1417. [DOI], [ADS], [arXiv:0905.0651 [astro-ph.SR]].

Beck, C., Choudhary, D. P., Rezaei, R. and Louis, R. E., 2015, "Fast Inversion of Solar Ca II Spectra", *The Astrophysical Journal*, **798**, 100. [DOI], [ADS], [arXiv:1410.8451 [astro-ph.SR]].

Beck, J. G., 2000, "A comparison of differential rotation measurements - (Invited Review)", *Solar Physics*, **191**, 47–70. [DOI], [ADS].

Beckers, J. M. and Tallant, P. E., 1969, "Chromospheric Inhomogeneities in Sunspot Umbrae", *Solar Physics*, **7**, 351–365. [DOI], [ADS].

Bellot Rubio, L. R., Balthasar, H., Collados, M. and Schlichenmaier, R., 2003, "Field-aligned Evershed flows in the photosphere of a sunspot penumbra", *Astronomy & Astrophysics*, **403**, L47–L50. [DOI], [ADS].

Bloomfield, D. S., Lagg, A. and Solanki, S. K., 2007, "The Nature of Running Penumbral Waves Revealed", *The Astrophysical Journal*, **671**, 1005–1012. [DOI], [ADS], [arXiv:0709.3731].

Bogdan, T. J. and Judge, P. G., 2006, "Observational aspects of sunspot oscillations", *Royal Society of London Philosophical Transactions Series A*, **364**, 313–331. [DOI], [ADS].

Bonet, J. A., Márquez, I., Muller, R., Sobotka, M. and Roudier, T., 2005, "Phase diversity restoration of sunspot images. II. Dynamics around a decaying sunspot", *Astronomy & Astrophysics*, **430**, 1089–1097. [DOI], [ADS].

Browning, P. K. and Priest, E. R., 1982, "The structure of untwisted magnetic flux tubes", *Geophysical & Astrophysical Fluid Dynamics*, **21**, 237–263. [DOI], [ADS].

Burroughs, W. J., 2007, *Climate Change: A Multidisciplinary Approach*, Cambridge University Press, Cambridge, 2nd edn.

Cameron, R., Schüssler, M., Vögler, A. and Zakharov, V., 2007, "Radiative magnetohydrodynamic simulations of solar pores", *Astronomy & Astrophysics*, **474**, 261–272. [DOI], [ADS].

Cavallini, F., 2006, "IBIS: A New Post-Focus Instrument for Solar Imaging Spectroscopy", *Solar Physics*, **236**, 415–439. [DOI], [ADS].

Chorley, N., Hnat, B., Nakariakov, V. M., Inglis, A. R. and Bakunina, I. A., 2010, "Long period oscillations in sunspots", *Astronomy & Astrophysics*, **513**, A27. [DOI], [ADS].

Chorley, N., Foullon, C., Hnat, B., Nakariakov, V. M. and Shibasaki, K., 2011, "Period persistence of long period oscillations in sunspots", *Astronomy & Astrophysics*, **529**, A123. [DOI], [ADS].

Christensen-Dalsgaard, J., 2002, "Helioseismology", *Reviews of Modern Physics*, **74**, 1073–1129. [DOI], [ADS], [astro-ph/0207403].

Christopoulou, E. B., Georgakilas, A. A. and Koutchmy, S., 2000, "Oscillations and running waves observed in sunspots", *Astronomy & Astrophysics*, **354**, 305–314. [ADS].

Christopoulou, E. B., Skodras, A., Georgakilas, A. A. and Koutchmy, S., 2003, "Wavelet Analysis of Umbral Oscillations", *The Astrophysical Journal*, **591**, 416–431. [DOI], [ADS].

Cooley, James W and Tukey, John W, 1965, "An algorithm for the machine calculation of complex Fourier series", *Mathematics of computation*, **19**(90), 297–301.

Cooper, F. C., Nakariakov, V. M. and Tsiklauri, D., 2003a, "Line-of-sight effects on observability of kink and sausage modes in coronal structures with imaging telescopes", *Astronomy & Astrophysics*, **397**, 765–770. [DOI], [ADS], [arXiv:astro-ph/0207167].

Cooper, F. C., Nakariakov, V. M. and Williams, D. R., 2003b, "Short period fast waves in solar coronal loops", *Astronomy & Astrophysics*, **409**, 325–330. [DOI], [ADS].

Cox, A. N., Livingston, W. C. and Matthews, M. S., 1991, *Solar interior and atmosphere*. [ADS].

Danielson, R. E., 1964, "The Structure of Sunspot Umbras. I. Observations.", *The Astrophysical Journal*, **139**, 45. [DOI], [ADS].

de la Cruz Rodríguez, J., Löfdahl, M. G., Sütterlin, P., Hillberg, T. and Rouppe van der Voort, L., 2015, "CRISPRED: A data pipeline for the CRISP imaging spectropolarimeter", *Astronomy & Astrophysics*, **573**, A40. [DOI], [ADS], [arXiv:1406.0202 [astro-ph.SR]].

de La Torre, L., Gimeno, L., Añel, J. A. and Nieto, R., 2007, "The role of the solar cycle in the relationship between the North Atlantic Oscillation and Northern Hemisphere surface temperatures", *Advances in Atmospheric Sciences*, **24**, 191–198. [DOI], [ADS].

De Moortel, I., 2005, "An overview of coronal seismology", *Royal Society of London Philosophical Transactions Series A*, **363**, 2743–2760. [DOI], [ADS].

De Moortel, I. and Nakariakov, V. M., 2012, "Magnetohydrodynamic waves and coronal seismology: an overview of recent results", *Royal Society of London Philosophical Transactions Series A*, **370**, 3193–3216. [DOI], [ADS], [arXiv:1202.1944 [astro-ph.SR]].

De Moortel, I., Ireland, J. and Walsh, R. W., 2000, "Observation of oscillations in coronal loops", *Astronomy & Astrophysics*, **355**, L23–L26. [ADS].

De Moortel, I., Hood, A. W. and Ireland, J., 2002, "Coronal seismology through wavelet analysis", *Astronomy & Astrophysics*, **381**, 311–323. [DOI], [ADS].

De Moortel, I., Munday, S. A. and Hood, A. W., 2004, "Wavelet Analysis: the effect of varying basic wavelet parameters", *Solar Physics*, **222**, 203–228. [DOI], [ADS].

De Pontieu, B., Erdélyi, R. and James, S. P., 2004, "Solar chromospheric spicules from the leakage of photospheric oscillations and flows", *Nature*, **430**, 536–539. [DOI], [ADS].

De Pontieu, B., McIntosh, S. W., Carlsson, M. et al., 2007, "Chromospheric Alfvénic Waves Strong Enough to Power the Solar Wind", *Science*, **318**, 1574. [DOI], [ADS].

De Pontieu, B., McIntosh, S. W., Carlsson, M. et al., 2011, "The Origins of Hot Plasma in the Solar Corona", *Science*, **331**, 55. [DOI], [ADS].

DeForest, C. E., Hagenaar, H. J., Lamb, D. A., Parnell, C. E. and Welsch, B. T., 2007, "Solar Magnetic Tracking. I. Software Comparison and Recommended Practices", *The Astrophysical Journal*, **666**, 576–587. [DOI], [ADS], [arXiv:0704.2921].

Deubner, F.-L. and Gough, D., 1984, "Helioseismology: Oscillations as a Daignostic of the Solar Interior", *Annual Review of Astronomy and Astrophysics*, **22**, 593–619. [DOI], [ADS].

Díaz, A. J. and Roberts, B., 2006, "Slow MHD oscillations in density structured coronal loops", *Astronomy & Astrophysics*, **458**, 975–985. [DOI], [ADS].

Dikpati, M. and Gilman, P. A., 2007, "Global solar dynamo models: simulations and predictions of cyclic photospheric fields and long-term non-reversing interior fields", *New Journal of Physics*, **9**, 297. [DOI], [ADS].

Domingo, V., Fleck, B. and Poland, A. I., 1995, "The SOHO Mission: an Overview", *Solar Physics*, **162**, 1–37. [DOI], [ADS].

Domínguez Cerdeña, I., Sánchez Almeida, J. and Kneer, F., 2006, "The Distribution of Quiet Sun Magnetic Field Strengths from 0 to 1800 G", *The Astrophysical Journal*, **636**, 496–509. [DOI], [ADS], [astro-ph/0509243].

Dorotovič, I., Sobotka, M., Brandt, P. N. and Simon, G. W., 2002, "Evolution and motions of small-scale photospheric structures near a large solar pore", *Astronomy & Astrophysics*, **387**, 665–671. [DOI], [ADS].

Dorotovič, I., Erdélyi, R. and Karlovský, V., 2008, "Identification of linear slow sausage waves in magnetic pores", in *Waves & Oscillations in the Solar Atmosphere: Heating and Magneto-Seismology*, (Eds.) Erdélyi, R., Mendoza-Briceno, C. A., IAU Symposium, 247, [DOI], [ADS].

Dorotovič, I., Erdélyi, R., Freij, N., Karlovský, V. and Márquez, I., 2014, "Standing sausage waves in photospheric magnetic waveguides", *Astronomy & Astrophysics*, **563**, A12. [DOI], [ADS].

Dragomiretskiy, K. and Zosso, D., 2014, "Variational Mode Decomposition", *IEEE Transactions on Signal Processing*, **62**, 531–544. [DOI], [ADS].

Eddy, J. A., 1976, "The Maunder Minimum", *Science*, **192**, 1189–1202. [DOI], [ADS].

Edwin, P. M. and Roberts, B., 1982, "Wave propagation in a magnetically structured atmosphere. III - The slab in a magnetic environment", *Solar Physics*, **76**, 239–259. [DOI], [ADS].

Edwin, P. M. and Roberts, B., 1983, "Wave propagation in a magnetic cylinder", *Solar Physics*, **88**, 179–191. [DOI], [ADS].

Erdélyi, R., 2004, "Coronal heating: Heating in the solar atmosphere", *Astronomy and Geophysics*, **45**(4), 34. [DOI], [ADS].

Erdélyi, R. and Ballai, I., 2007, "Heating of the solar and stellar coronae: a review", *Astronomische Nachrichten*, **328**, 726–733. [DOI], [ADS].

Erdélyi, R. and Fedun, V., 2007, "Are There Alfvén Waves in the Solar Atmosphere?", *Science*, **318**, 1572. [DOI], [ADS].

Erdélyi, R. and Fedun, V., 2010, "Magneto-Acoustic Waves in Compressible Magnetically Twisted Flux Tubes", *Solar Physics*, **263**, 63–85. [DOI], [ADS].

Erdélyi, R. and Morton, R. J., 2009, "Magnetohydrodynamic waves in a compressible magnetic flux tube with elliptical cross-section", *The Astrophysical Journal*, **494**, 295–309. [DOI], [ADS].

Erdélyi, R., Doyle, J. G., Perez, M. E. and Wilhelm, K., 1998, "Center-to-limb line width measurements of solar chromospheric, transition region and coronal lines", *Astronomy & Astrophysics*, **337**, 287–293. [ADS].

Erdélyi, R., Malins, C., Tóth, G. and de Pontieu, B., 2007, "Leakage of photospheric acoustic waves into non-magnetic solar atmosphere", *Astronomy & Astrophysics*, **467**, 1299–1311. [DOI], [ADS].

Erdélyi, R., Hague, A. and Nelson, C. J., 2013, "Effects of Stratification and Flows on P_1/P_2 Ratios and Anti-node Shifts Within Closed Loop Structures", *Solar Physics*. [DOI], [ADS], [arXiv:1306.1051 [astro-ph.SR]].

Evans, D. J. and Roberts, B., 1990, "The oscillations of a magnetic flux tube and its application to sunspots", *The Astrophysical Journal*, **348**, 346–356. [DOI], [ADS].

Farge, M., 1992, "Wavelet transforms and their applications to turbulence", *Annual Review of Fluid Mechanics*, **24**, 395–457. [DOI], [ADS].

Fedun, V., Shelyag, S. and Erdélyi, R., 2011a, "Numerical Modeling of Footpoint-driven Magneto-acoustic Wave Propagation in a Localized Solar Flux Tube", *The Astrophysical Journal*, **727**, 17. [DOI], [ADS].

Fedun, V., Shelyag, S., Verth, G., Mathioudakis, M. and Erdélyi, R., 2011b, "MHD waves generated by high-frequency photospheric vortex motions", *Annales Geophysicae*, **29**, 1029–1035. [DOI], [ADS].

Feng, S., Deng, L., Yang, Y. and Ji, K., 2013, "Statistical study of photospheric bright points in an active region and quiet Sun", *Astrophysics and Space Science*, **348**, 17–24. [DOI], [ADS].

Fleck, B. and Deubner, F.-L., 1989, "Dynamics of the solar atmosphere. II - Standing waves in the solar chromosphere", *Astronomy & Astrophysics*, **224**, 245–252. [ADS].

Freeland, S. L. and Handy, B. N., 1998, "Data Analysis with the SolarSoft System", *Solar Physics*, **182**, 497–500. [DOI], [ADS].

Freij, N., Scullion, E. M., Nelson, C. J., Mumford, S., Wedemeyer, S. and Erdélyi, R., 2014, "The Detection of Upwardly Propagating Waves Channeling Energy from the Chromosphere to the Low Corona", *The Astrophysical Journal*, **791**, 61. [DOI], [ADS], [arXiv:1408.4621 [astro-ph.SR]].

Freij, N., Dorotovič, I., Morton, R. J., Ruderman, M. S., Karlovský, V. and Erdélyi, R., 2016, "On the Properties of Slow MHD Sausage Waves within Small-scale Photospheric Magnetic Structures", *The Astrophysical Journal*, **817**, 44. [DOI], [ADS], [arXiv:1509.08680 [astro-ph.SR]].

Friis-Christensen, E. and Lassen, K., 1991, "Length of the Solar Cycle: An Indicator of Solar Activity Closely Associated with Climate", *Science*, **254**, 698–700. [DOI], [ADS].

Fujimura, D. and Tsuneta, S., 2009, "Properties of Magnetohydrodynamic Waves in the Solar Photosphere Obtained with Hinode", *The Astrophysical Journal*, **702**, 1443–1457. [DOI], [ADS], [arXiv:0907.3025 [astro-ph.SR]].

Gary, G. A., 2001, "Plasma Beta above a Solar Active Region: Rethinking the Paradigm", *Solar Physics*, **203**, 71–86. [DOI], [ADS].

Gent, F. A., Fedun, V., Mumford, S. J. and Erdélyi, R., 2013, "Magnetohydrostatic equilibrium - I. Three-dimensional open magnetic flux tube in the stratified solar atmosphere", *Monthly Notices of the Royal Astronomical Society*, **435**, 689–697. [DOI], [ADS].

Gent, F. A., Fedun, V. and Erdélyi, R., 2014, "Magnetohydrostatic Equilibrium. II. Three-dimensional Multiple Open Magnetic Flux Tubes in the Stratified Solar Atmosphere", *The Astrophysical Journal*, **789**, 42. [DOI], [ADS], [arXiv:1405.0613 [astro-ph.SR]].

Georgakilas, A. A., Christopoulou, E. B. and Koutchmy, S., 2002, "Oscillations and waves related to sunspots", *Nuovo Cimento C Geophysics Space Physics C*, **25**, 601. [ADS].

Gimeno, L., de la Torre, L., Nieto, R., García, R., Hernández, E. and Ribera, P., 2003, "Changes in the relationship NAO-Northern hemisphere temperature due to solar activity", *Earth and Planetary Science Letters*, **206**, 15–20. [DOI], [ADS].

Giovanelli, R. G., 1972, "Oscillations and Waves in a Sunspot", *Solar Physics*, **27**, 71–79. [DOI], [ADS].

Goedbloed, J. P. H. and Poedts, S., 2004, *Principles of Magnetohydrodynamics*. [ADS].

Goossens, M., Andries, J. and Aschwanden, M. J., 2002, "Coronal loop oscillations. An interpretation in terms of resonant absorption of quasi-mode kink oscillations", *Astronomy & Astrophysics*, **394**, L39–L42. [DOI], [ADS].

Gosain, S., Mathew, S. K. and Venkatakrishnan, P., 2011, "Acoustic Power Absorption and its Relation to Vector Magnetic Field of a Sunspot", *Solar Physics*, **268**, 335–348. [DOI], [ADS], [arXiv:1008.1456 [astro-ph.SR]].

Grant, S. D. T., Jess, D. B., Moreels, M. G. et al., 2015, "Wave Damping Observed in Upwardly Propagating Sausage-mode Oscillations Contained within a Magnetic Pore", *The Astrophysical Journal*, **806**, 132. [DOI], [ADS], [arXiv:1505.01484 [astro-ph.SR]].

Handy, B. N., Acton, L. W., Kankelborg, C. C. et al., 1999, "The transition region and coronal explorer", *Solar Physics*, **187**, 229–260. [DOI], [ADS].

Hasan, S. S. and van Ballegooijen, A. A., 2008, "Dynamics of the Solar Magnetic Network. II. Heating the Magnetized Chromosphere", *The Astrophysical Journal*, **680**, 1542–1552. [DOI], [ADS], [arXiv:0802.3509].

Hasan, S. S., van Ballegooijen, A. A., Kalkofen, W. and Steiner, O., 2005, "Dynamics of the Solar Magnetic Network: Two-dimensional MHD Simulations", *The Astrophysical Journal*, **631**, 1270–1280. [DOI], [ADS], [astro-ph/0503525].

Henriques, V. M. J., 2012, "Three-dimensional temperature mapping of solar photospheric fine structure using Ca ii H filtergrams", *Astronomy & Astrophysics*, **548**, A114. [DOI], [ADS], [arXiv:1210.4168 [astro-ph.SR]].

Hirzberger, J., Bonet, J. A., Sobotka, M., Vázquez, M. and Hanslmeier, A., 2002, "Fine structure and dynamics in a light bridge inside a solar pore", *Astronomy & Astrophysics*, **383**, 275–282. [DOI], [ADS].

Horne, J. H. and Baliunas, S. L., 1986, "A prescription for period analysis of unevenly sampled time series", *The Astrophysical Journal*, **302**, 757–763. [DOI], [ADS].

Howe, R., Christensen-Dalsgaard, J., Hill, F., Komm, R. W., Larsen, R. M., Schou, J., Thompson, M. J. and Toomre, J., 2000, "Dynamic Variations at the Base of the Solar Convection Zone", *Science*, **287**, 2456–2460. [DOI], [ADS].

Huang, N. E. and Wu, Z., 2008, "A review on Hilbert-Huang transform: Method and its applications to geophysical studies", *Reviews of Geophysics*, **46**, RG2006. [DOI], [ADS].

Huang, N. E., Shen, Z., Long, S. R. et al., 1998, "The empirical mode decomposition and the Hilbert spectrum for nonlinear and non-stationary time series analysis", *Proceedings of the Royal Society of London Series A*, **454**, 903–998. [DOI], [ADS].

Hunter, J. D., 2007, "Matplotlib: A 2D Graphics Environment", *Computing in Science and Engineering*, **9**, 90–95. [DOI], [ADS].

Jess, D. B., Andić, A., Mathioudakis, M., Bloomfield, D. S. and Keenan, F. P., 2007, "High-frequency oscillations in a solar active region observed with the RAPID DUAL IMAGER", *Astronomy & Astrophysics*, **473**, 943–950. [DOI], [ADS], [arXiv:0707.2716].

Jess, D. B., Mathioudakis, M., Erdélyi, R., Crockett, P. J., Keenan, F. P. and Christian, D. J., 2009, "Alfvén Waves in the Lower Solar Atmosphere", *Science*, **323**, 1582. [DOI], [ADS], [arXiv:0903.3546 [astro-ph.SR]].

Jess, D. B., Mathioudakis, M., Christian, D. J., Keenan, F. P., Ryans, R. S. I. and Crockett, P. J., 2010, "ROSA: A High-cadence, Synchronized Multi-camera Solar Imaging System", *Solar Physics*, **261**, 363–373. [DOI], [ADS], [arXiv:0912.4118 [astro-ph.SR]].

Jess, D. B., Reznikova, V. E., Van Doorsselaere, T., Keys, P. H. and Mackay, D. H., 2013, "The Influence of the Magnetic Field on Running Penumbral Waves in the Solar Chromosphere", *The Astrophysical Journal*, **779**, 168. [DOI], [ADS], [arXiv:1310.7939 [astro-ph.SR]].

Jess, D. B., Morton, R. J., Verth, G., Fedun, V., Grant, S. D. T. and Giagkiozis, I., 2015, "Multiwavelength Studies of MHD Waves in the Solar Chromosphere. An Overview of Recent Results", *Space Science Reviews*, **190**, 103–161. [DOI], [ADS], [arXiv:1503.01769 [astro-ph.SR]].

Jones, E., Oliphant, T. and Peterson, P., 2001, "SciPy: Open source scientific tools for Python".

Kato, Y., Steiner, O., Steffen, M. and Suematsu, Y., 2011, "Excitation of Slow Modes in Network Magnetic Elements Through Magnetic Pumping", *The Astrophysical Journal, Letters*, **730**, L24. [DOI], [ADS], [arXiv:1102.5164 [astro-ph.SR]].

Katsiyannis, A. C., Williams, D. R., McAteer, R. T. J., Gallagher, P. T., Keenan, F. P. and Murtagh, F., 2003, "Eclipse observations of high-frequency oscillations in active region coronal loops", *Astronomy & Astrophysics*, **406**, 709–714. [DOI], [ADS], [astro-ph/0305225].

Katsukawa, Y., Berger, T. E., Ichimoto, K. et al., 2007, "Small-Scale Jetlike Features in Penumbral Chromospheres", *Science*, **318**, 1594. [DOI], [ADS].

Keller, C. U. and von der Luehe, O., 1992, "Solar speckle polarimetry", *Astronomy & Astrophysics*, **261**, 321–328. [ADS].

Kelvinsong, 2015, accessed: 2015-01-01. License: Creative Commons Attribution-ShareAlike 3.0 Unported.

Khomenko, E. and Cally, P. S., 2012, "Numerical Simulations of Conversion to Alfvén Waves in Sunspots", *The Astrophysical Journal*, **746**, 68. [DOI], [ADS], [arXiv:1111.2851 [astro-ph.SR]].

Khomenko, E., Collados, M. and Felipe, T., 2008, "Nonlinear Numerical Simulations of Magneto-Acoustic Wave Propagation in Small-Scale Flux Tubes", *Solar Physics*, **251**, 589–611. [DOI], [ADS], [arXiv:0710.3335].

Kiselman, D., Pereira, T. M. D., Gustafsson, B., Asplund, M., Meléndez, J. and Langhans, K., 2011, "Is the solar spectrum latitude-dependent?. An investigation with SST/TRIPPEL", *Astronomy & Astrophysics*, **535**, A14. [DOI], [ADS], [arXiv:1108.4527 [astro-ph.SR]].

Kitagawa, N., Yokoyama, T., Imada, S. and Hara, H., 2010, "Mode Identification of MHD Waves in an Active Region Observed with Hinode/EIS", *The Astrophysical Journal*, **721**, 744–749. [DOI], [ADS], [arXiv:1008.1823 [astro-ph.SR]].

Kobanov, N. I. and Makarchik, D. V., 2004, "Pulsating Evershed Flows and Propagating Waves in a Sunspot", *Astronomy Reports*, **48**, 954–964. [DOI], [ADS].

Kobanov, N. I., Kolobov, D. Y. and Makarchik, D. V., 2006, "Umbral Three-Minute Oscillations and Running Penumbral Waves", *Solar Physics*, **238**, 231–244. [DOI], [ADS].

Kontar, E. P., Hannah, I. G. and MacKinnon, A. L., 2008, "Chromospheric magnetic field and density structure measurements using hard X-rays in a flaring coronal loop", *Astronomy & Astrophysics*, **489**, L57–L60. [DOI], [ADS], [arXiv:0808.3334].

Kosovichev, A. G., 2009, "Solar Oscillations", in *American Institute of Physics Conference Series*, (Eds.) Guzik, J. A., Bradley, P. A., American Institute of Physics Conference Series, 1170, [DOI], [ADS], [arXiv:1001.5283 [astro-ph.SR]].

Kubo, M., Lites, B. W., Shimizu, T. and Ichimoto, K., 2008, "Magnetic Flux Loss and Flux Transport in a Decaying Active Region", *The Astrophysical Journal*, **686**, 1447–1453. [DOI], [ADS], [arXiv:0807.4340].

Langhans, K., Scharmer, G. B., Kiselman, D., Löfdahl, M. G. and Berger, T. E., 2005, "Inclination of magnetic fields and flows in sunspot penumbrae", *Astronomy & Astrophysics*, **436**, 1087–1101. [DOI], [ADS].

Leenaarts, J., Carlsson, M., Hansteen, V. and Rutten, R. J., 2007, "Non-equilibrium hydrogen ionization in 2D simulations of the solar atmosphere", *Astronomy & Astrophysics*, **473**, 625–632. [DOI], [ADS], [arXiv:0709.3751].

Leenaarts, J., Carlsson, M. and Rouppe van der Voort, L., 2012, "The Formation of the Hα Line in the Solar Chromosphere", *The Astrophysical Journal*, **749**, 136. [DOI], [ADS], [arXiv:1202.1926 [astro-ph.SR]].

Leibacher, J., Gouttebroze, P. and Stein, R. F., 1982, "Solar atmospheric dynamics. II - Nonlinear models of the photospheric and chromospheric oscillations", *The Astrophysical Journal*, **258**, 393–403. [DOI], [ADS].

Lemen, J. R., Title, A. M., Akin, D. J. et al., 2012, "The Atmospheric Imaging Assembly (AIA) on the Solar Dynamics Observatory (SDO)", *Solar Physics*, **275**, 17–40. [DOI], [ADS].

Lin, H., Kuhn, J. R. and Coulter, R., 2004, "Coronal Magnetic Field Measurements", *The Astrophysical Journal Letters*, **613**, L177–L180. [DOI], [ADS].

Linnell Nemec, A. F. and Nemec, J. M., 1985, "A test of significance for periods derived using phase-dispersion-minimization techniques", *Astronomical Journal*, **90**, 2317–2320. [DOI], [ADS].

Liu, Y., San Liang, X. and Weisberg, R. H., 2007, "Rectification of the Bias in the Wavelet Power Spectrum", *Journal of Atmospheric and Oceanic Technology*, **24**, 2093. [DOI], [ADS].

Livingston, W., Harvey, J. W., Malanushenko, O. V. and Webster, L., 2006, "Sunspots with the Strongest Magnetic Fields", *Solar Physics*, **239**, 41–68. [DOI], [ADS].

Lockwood, M., Harrison, R. G., Woollings, T. and Solanki, S. K., 2010, "Are cold winters in Europe associated with low solar activity?", *Environmental Research Letters*, **5**(2), 024001. [DOI], [ADS].

Longcope, D. W., 1996, "Topology and Current Ribbons: A Model for Current, Reconnection and Flaring in a Complex, Evolving Corona", *Solar Physics*, **169**, 91–121. [DOI], [ADS].

Longcope, D. W. and Klapper, I., 2002, "A General Theory of Connectivity and Current Sheets in Coronal Magnetic Fields Anchored to Discrete Sources", *The Astrophysical Journal*, **579**, 468–481. [DOI], [ADS].

Luna-Cardozo, M., Verth, G. and Erdélyi, R., 2012, "Longitudinal Oscillations in Density Stratified and Expanding Solar Waveguides", *The Astrophysical Journal*, **748**, 110. [DOI], [ADS], [arXiv:1204.4201 [astro-ph.SR]].

Malins, C. and Erdélyi, R., 2007, "Direct Propagation of Photospheric Acoustic p Modes into Nonmagnetic Solar Atmosphere", *Solar Physics*, **246**, 41–52. [DOI], [ADS].

Maltby, P., Avrett, E. H., Carlsson, M., Kjeldseth-Moe, O., Kurucz, R. L. and Loeser, R., 1986, "A new sunspot umbral model and its variation with the solar cycle", *The Astrophysical Journal*, **306**, 284–303. [DOI], [ADS].

Marsh, M. S. and Walsh, R. W., 2006, "p-Mode Propagation through the Transition Region into the Solar Corona. I. Observations", *The Astrophysical Journal*, **643**, 540–548. [DOI], [ADS].

Marsh, M. S., Walsh, R. W. and Bromage, B. J. I., 2002, "A wavelet analysis of quasi-periodic variability across a solar coronal hole region", *Astronomy & Astrophysics*, **393**, 649–659. [DOI], [ADS].

Martínez Pillet, V., 2002, "Decay of sunspots", *Astronomische Nachrichten*, **323**, 342–348. [DOI], [ADS].

Mathew, S. K., 2008, "Enhanced p-Mode Absorption Seen Near the Sunspot Umbral Penumbral Boundary", *Solar Physics*, **251**, 515–522. [DOI], [ADS], [arXiv:0806.2700].

Mathioudakis, M., Bloomfield, D. S., Jess, D. B., Dhillon, V. S. and Marsh, T. R., 2006, "The periodic variations of a white-light flare observed with ULTRACAM", *Astronomy & Astrophysics*, **456**, 323–327. [DOI], [ADS], [astro-ph/0605196].

Mathioudakis, M., Jess, D. B. and Erdélyi, R., 2013, "Alfvén Waves in the Solar Atmosphere. From Theory to Observations", *Space Science Reviews*, **175**, 1–27. [DOI], [ADS], [arXiv:1210.3625 [astro-ph.SR]].

McIntosh, S. W., 2012, "Recent Observations of Plasma and Alfvénic Wave Energy Injection at the Base of the Fast Solar Wind", *Space Science Reviews*, **172**, 69–87. [DOI], [ADS], [arXiv:1205.3821 [astro-ph.SR]].

McIntosh, S. W., de Pontieu, B., Carlsson, M., Hansteen, V., Boerner, P. and Goossens, M., 2011, "Alfvénic waves with sufficient energy to power the quiet solar corona and fast solar wind", *Nature*, **475**, 477–480. [DOI], [ADS].

McLaughlin, J. A., Hood, A. W. and de Moortel, I., 2011, "Review Article: MHD Wave Propagation Near Coronal Null Points of Magnetic Fields", *Space Science Reviews*, **158**, 205–236. [DOI], [ADS], [arXiv:1004.5568 [astro-ph.SR]].

Mein, N. and Mein, P., 1976, "Velocity waves in the quiet solar chromosphere", *Solar Physics*, **49**, 231–248. [DOI], [ADS].

Metcalf, T. R., Jiao, L., McClymont, A. N., Canfield, R. C. and Uitenbroek, H., 1995, "Is the solar chromospheric magnetic field force-free?", *The Astrophysical Journal*, **439**, 474–481. [DOI], [ADS].

Meyer, F., Schmidt, H. U., Wilson, P. R. and Weiss, N. O., 1974, "The growth and decay of sunspots", *Monthly Notices of the Royal Astronomical Society*, **169**, 35–57. [DOI], [ADS].

Montesinos, B. and Thomas, J. H., 1997, "The Evershed effect in sunspots as a siphon flow along a magnetic flux tube", *Nature*, **390**, 485. [DOI], [ADS].

Moreels, M. G. and Van Doorsselaere, T., 2013, "Phase relations for seismology of photospheric flux tubes", *Astronomy & Astrophysics*, **551**, A137. [DOI], [ADS].

Moreels, M. G., Goossens, M. and Van Doorsselaere, T., 2013, "Cross-sectional area and intensity variations of sausage modes", *Astronomy & Astrophysics*, **555**, A75. [DOI], [ADS].

Moreels, M. G., Freij, N., Erdélyi, R., Van Doorsselaere, T. and Verth, G., 2015a, "Observations and mode identification of sausage waves in a magnetic pore", *Astronomy & Astrophysics*, **579**, A73. [DOI], [ADS].

Moreels, M. G., Van Doorsselaere, T., Grant, S. D. T., Jess, D. B. and Goossens, M., 2015b, "Energy and energy flux in axisymmetric slow and fast waves", *Astronomy & Astrophysics*, **578**, A60. [DOI], [ADS].

Moreton, G. E., 1960, "Hα Observations of Flare-Initiated Disturbances with Velocities ≈1000 km/sec.", *Astronomical Journal*, **65**, 494. [DOI], [ADS].

Morton, R. J. and Erdélyi, R., 2009, "The effect of elliptic shape on the period ratio P_1/P_2 of emerging coronal loops", *Astronomy & Astrophysics*, **502**, 315–323. [DOI], [ADS].

Morton, R. J. and Ruderman, M. S., 2011, "Kink and fluting modes of stratified coronal magnetic loops with elliptical cross-sections", *Astronomy & Astrophysics*, **527**, A53. [DOI], [ADS], [arXiv:1011.2377 [astro-ph.SR]].

Morton, R. J., Erdélyi, R., Jess, D. B. and Mathioudakis, M., 2011, "Observations of Sausage Modes in Magnetic Pores", *The Astrophysical Journal, Letters*, **729**, L18. [DOI], [ADS], [arXiv:1011.2375 [astro-ph.SR]].

Morton, R. J., Verth, G., Jess, D. B., Kuridze, D., Ruderman, M. S., Mathioudakis, M. and Erdélyi, R., 2012, "Observations of ubiquitous compressive waves in the Sun's chromosphere", *Nature Communications*, **3**, 1315. [ADS].

Mumford, S. J., Fedun, V. and Erdélyi, R., 2015, "Generation of Magnetohydrodynamic Waves in Low Solar Atmospheric Flux Tubes by Photospheric Motions", *The Astrophysical Journal*, **799**, 6. [DOI], [ADS], [arXiv:1305.7415 [astro-ph.SR]].

Nakariakov, V. M., 2007, "MHD oscillations in solar and stellar coronae: Current results and perspectives", *Advances in Space Research*, **39**, 1804–1813. [DOI], [ADS].

Nakariakov, V. M. and Verwichte, E., 2005, "Coronal Waves and Oscillations", *Living Reviews in Solar Physics*, **2**. [DOI], [ADS].

Nakariakov, V. M., Ofman, L., Deluca, E. E., Roberts, B. and Davila, J. M., 1999, "TRACE observation of damped coronal loop oscillations: Implications for coronal heating", *Science*, **285**, 862–864. [DOI], [ADS].

Nelson, C. J. and Doyle, J. G., 2013, "Excitation of an outflow from the lower solar atmosphere and a co-temporal EUV transient brightening", *Astronomy & Astrophysics*, **560**, A31. [DOI], [ADS], [arXiv:1310.8490 [astro-ph.SR]].

Nelson, C. J., Doyle, J. G., Erdélyi, R., Huang, Z., Madjarska, M. S., Mathioudakis, M., Mumford, S. J. and Reardon, K., 2013a, "Statistical Analysis of Small Ellerman Bomb Events", *Solar Physics*, **283**, 307–323. [DOI], [ADS], [arXiv:1301.1351 [astro-ph.SR]].

Nelson, C. J., Shelyag, S., Mathioudakis, M., Doyle, J. G., Madjarska, M. S., Uitenbroek, H. and Erd''elyi, R., 2013b, "Ellerman Bombs-Evidence for Magnetic Reconnection in the Lower Solar Atmosphere", *The Astrophysical Journal*, **779**, 125. [DOI], [ADS], [arXiv:1310.7756 [astro-ph.SR]].

Nelson, C. J., Scullion, E. M., Doyle, J. G., Freij, N. and Erdélyi, R., 2015, "Small-scale Structuring of Ellerman Bombs at the Solar Limb", *The Astrophysical Journal*, **798**, 19. [DOI], [ADS], [arXiv:1410.5715 [astro-ph.SR]].

Nye, A. H. and Thomas, J. H., 1974, "The nature of running penumbral waves", *Solar Physics*, **38**, 399–413. [DOI], [ADS].

Ofman, L. and Aschwanden, M. J., 2002, "Damping Time Scaling of Coronal Loop Oscillations Deduced from Transition Region and Coronal Explorer Observations", *The Astrophysical Journal, Letters*, **576**, L153–L156. [DOI], [ADS].

Ofman, L., Romoli, M., Poletto, G., Noci, G. and Kohl, J. L., 1997, "Ultraviolet Coronagraph Spectrometer Observations of Density Fluctuations in the Solar Wind", *The Astrophysical Journal, Letters*, **491**, L111–L114. [DOI], [ADS].

Olcott, W.T., 1914, *Sun Lore of All Ages: A Collection of Myths and Legends Concerning the Sun and Its Worship*, G.P. Putnam's sons.

O'Shea, E., Srivastava, A. K., Doyle, J. G. and Banerjee, D., 2007, "Evidence for wave harmonics in cool loops", *Astronomy & Astrophysics*, **473**, L13–L16. [DOI], [ADS].

Page, D. and Hirsch, J. G. (Eds.), 2000, *From the Sun to the Great Attractor*, Lecture Notes in Physics, Berlin Springer Verlag, 556. [ADS].

Parker, E. N., 1979, "Sunspots and the physics of magnetic flux tubes. I - The general nature of the sunspot. II - Aerodynamic drag", *The Astrophysical Journal*, **230**, 905–923. [DOI], [ADS].

Parnell, C. E. and De Moortel, I., 2012, "A contemporary view of coronal heating", *Royal Society of London Philosophical Transactions Series A*, **370**, 3217–3240. [DOI], [ADS], [arXiv:1206.6097 [astro-ph.SR]].

Perez, Fernando and Granger, Brian E., 2007, "IPython: A System for Interactive Scientific Computing", *Computing in Science & Engineering*, **9**(3), 21–29. [DOI].

Pesnell, W. D., Thompson, B. J. and Chamberlin, P. C., 2012, "The Solar Dynamics Observatory (SDO)", *Solar Physics*, **275**, 3–15. [DOI], [ADS].

Peter, H., Gudiksen, B. V. and Nordlund, Å., 2006, "Forward Modeling of the Corona of the Sun and Solar-like Stars: From a Three-dimensional Magnetohydrodynamic Model to Synthetic Extreme-Ultraviolet Spectra", *The Astrophysical Journal*, **638**, 1086–1100. [DOI], [ADS], [astro-ph/0503342].

Phillips, K. J. H., 1995, *Guide to the Sun*. [ADS].

Priest, E., 2014, *Magnetohydrodynamics of the Sun*, Cambridge University Press. [ADS].

Priest, E. R., 1984, *Solar magneto-hydrodynamics*, Springer. [ADS].

Project, Galileo, 2015, accessed: 2015-01-01. No copyright.

Reale, F., 2010, "Coronal Loops: Observations and Modeling of Confined Plasma", *Living Reviews in Solar Physics*, **7**. [DOI], [ADS], [arXiv:1010.5927 [astro-ph.SR]].

Reid, A., Mathioudakis, M., Scullion, E., Doyle, J. G., Shelyag, S. and Gallagher, P., 2015, "Ellerman Bombs with Jets: Cause and Effect", *The Astrophysical Journal*, **805**, 64. [DOI], [ADS], [arXiv:1503.05359 [astro-ph.SR]].

Rempel, M. and Schlichenmaier, R., 2011, "Sunspot Modeling: From Simplified Models to Radiative MHD Simulations", *Living Reviews in Solar Physics*, **8**. [DOI], [ADS].

Reznikova, V. E. and Shibasaki, K., 2012, "Spatial Structure of Sunspot Oscillations Observed with SDO/AIA", *The Astrophysical Journal*, **756**, 35. [DOI], [ADS].

Rieutord, M. and Rincon, F., 2010, "The Sun's Supergranulation", *Living Reviews in Solar Physics*, **7**. [DOI], [ADS], [arXiv:1005.5376 [astro-ph.SR]].

Roberts, B., 2006, "Slow magnetohydrodynamic waves in the solar atmosphere", *Philosophical Transactions of the Royal Society of London Series A*, **364**, 447–460. [DOI], [ADS].

Roudier, T., Bonet, J. A. and Sobotka, M., 2002, "Properties of horizontal flows inside and outside a solar pore", *Astronomy & Astrophysics*, **395**, 249–255. [DOI], [ADS].

Rouppe van der Voort, L. H. M., Rutten, R. J., Sütterlin, P., Sloover, P. J. and Krijger, J. M., 2003, "La Palma observations of umbral flashes", *Astronomy & Astrophysics*, **403**, 277–285. [DOI], [ADS].

Ruderman, M. S., 2003, "The resonant damping of oscillations of coronal loops with elliptic cross-sections", *Astronomy & Astrophysics*, **409**, 287–297. [DOI], [ADS].

Ruderman, M. S. and Erdélyi, R., 2009, "Transverse Oscillations of Coronal Loops", *Space Science Reviews*, **149**, 199–228. [DOI], [ADS].

Rutten, R. J., 2012, "The quiet-Sun photosphere and chromosphere", *Royal Society of London Philosophical Transactions Series A*, **370**, 3129–3150. [DOI], [ADS], [arXiv:1110.6606 [astro-ph.SR]].

Rutten, R. J. and Severino, G., 2012, *Solar and Stellar Granulation*, Nato Science Series C:, Springer NetherlandsURL: https://books.google.co.uk/books?id=5zXqCAAAQBAJ.

Rutten, R. J., Hammerschlag, R. H., Bettonvil, F. C. M., Sütterlin, P. and de Wijn, A. G., 2004, "DOT tomography of the solar atmosphere. I. Telescope summary and program definition", *Astronomy & Astrophysics*, **413**, 1183–1189. [DOI], [ADS].

Sánchez Almeida, J., Márquez, I., Bonet, J. A., Domínguez Cerdeña, I. and Muller, R., 2004, "Bright Points in the Internetwork Quiet Sun", *The Astrophysical Journal, Letters*, **609**, L91–L94. [DOI], [ADS], [astro-ph/0405515].

Scargle, J. D., 1982, "Studies in astronomical time series analysis. II - Statistical aspects of spectral analysis of unevenly spaced data", *The Astrophysical Journal*, **263**, 835–853. [DOI], [ADS].

Scharmer, G. and Lofdahl, M., 1991, "Swedish Solar Telescope - Short summary of instrumentation and observation techniques", *Advances in Space Research*, **11**, 129–132. [DOI], [ADS].

Scharmer, G. B., Pettersson, L., Brown, D. S. and Rehn, J., 1985, "Concepts for the Swedish 50-cm vacuum solar telescope", *Applied Optics*, **24**, 2558–2564. [DOI], [ADS].

Scharmer, G. B., Gudiksen, B. V., Kiselman, D., Löfdahl, M. G. and Rouppe van der Voort, L. H. M., 2002, "Dark cores in sunspot penumbral filaments", *Nature*, **420**, 151–153. [ADS].

Scharmer, G. B., Narayan, G., Hillberg, T. et al., 2008, "CRISP Spectropolarimetric Imaging of Penumbral Fine Structure", *The Astrophysical Journal, Letters*, **689**, L69–L72. [DOI], [ADS], [arXiv:0806.1638].

Scharmer, G. B., Henriques, V. M. J., Kiselman, D. and de la Cruz Rodríguez, J., 2011, "Detection of Convective Downflows in a Sunspot Penumbra", *Science*, **333**, 316. [DOI], [ADS].

Schlichenmaier, R., Rezaei, R., Bello González, N. and Waldmann, T. A., 2010, "The formation of a sunspot penumbra", *Astronomy & Astrophysics*, **512**, L1. [DOI], [ADS].

Schou, J., Scherrer, P. H., Bush, R. I. et al., 2012, "Design and Ground Calibration of the Helioseismic and Magnetic Imager (HMI) Instrument on the Solar Dynamics Observatory (SDO)", *Solar Physics*, **275**, 229–259. [DOI], [ADS].

Schrijver, C. J., Title, A. M., Berger, T. E. et al., 1999, "A new view of the solar outer atmosphere by the Transition Region and Coronal Explorer", *Solar Physics*, **187**, 261–302. [DOI], [ADS].

Scullion, E., Erdélyi, R., Fedun, V. and Doyle, J. G., 2011, "The Response of A Three-dimensional Solar Atmosphere to Wave-driven Jets", *The Astrophysical Journal*, **743**, 14. [DOI], [ADS].

Sekse, D. H., Rouppe van der Voort, L., De Pontieu, B. and Scullion, E., 2013, "Interplay of Three Kinds of Motion in the Disk Counterpart of Type II Spicules: Upflow, Transversal, and Torsional Motions", *The Astrophysical Journal*, **769**, 44. [DOI], [ADS], [arXiv:1304.2304 [astro-ph.SR]].

Shelyag, S., Fedun, V., Keenan, F. P., Erdélyi, R. and Mathioudakis, M., 2011, "Photospheric magnetic vortex structures", *Annales Geophysicae*, **29**, 883–887. [DOI], [ADS].

Simon, G. W. and Weiss, N. O., 1970, "On the Magnetic Field in Pores", *Solar Physics*, **13**, 85–103. [DOI], [ADS].

Sobotka, M., Brandt, P. N. and Simon, G. W., 1997a, "Fine structure in sunspots. I. Sizes and lifetimes of umbral dots", *Astronomy & Astrophysics*, **328**, 682–688. [ADS].

Sobotka, M., Brandt, P. N. and Simon, G. W., 1997b, "Fine structure in sunspots. II. Intensity variations and proper motions of umbral dots", *Astronomy & Astrophysics*, **328**, 689–694. [ADS].

Socas-Navarro, H., de la Cruz Rodríguez, J., Asensio Ramos, A., Trujillo Bueno, J. and Ruiz Cobo, B., 2015, "An open-source, massively parallel code for non-LTE synthesis and inversion of spectral lines and Zeeman-induced Stokes profiles", *Astronomy & Astrophysics*, **577**, A7. [DOI], [ADS], [arXiv:1408.6101 [astro-ph.SR]].

Solanki, S. K., 2003, "Sunspots: An overview", *Astronomy & Astrophysics Reviews*, **11**, 153–286. [DOI], [ADS].

Soward, A. M., Jones, C. A., Hughes, D. W. and Weiss, N. O. (Eds.), 2005, *Fluid Dynamics and Dynamos in Astrophysics and Geophysics: reviews emerging from the Durham Symposium on Astrophysical Fluid Mechanics held July 29 to August 8, 2002*. [ADS].

Stangalini, M., Giannattasio, F., Del Moro, D. and Berrilli, F., 2012, "Three-minute wave enhancement in the solar photosphere", *Astronomy & Astrophysics*, **539**, L4. [DOI], [ADS], [arXiv:1202.1384 [astro-ph.SR]].

Staude, J., 1999, "Sunspot Oscillations", in *Third Advances in Solar Physics Euroconference: Magnetic Fields and Oscillations*, (Eds.) Schmieder, B., Hofmann, A., Staude, J., Astronomical Society of the Pacific Conference Series, 184, [ADS].

Steiner, O., Grossmann-Doerth, U., Knoelker, M. and Schuessler, M., 1998, "Dynamical Interaction of Solar Magnetic Elements and Granular Convection: Results of a Numerical Simulation", *The Astrophysical Journal*, **495**, 468. [DOI], [ADS].

Stix, M., 2004, *The Sun: An Introduction*, Astronomy and Astrophysics Library, Springer Berlin HeidelbergURL: https://books.google.co.uk/books?id=wxHN9jP-mNMC.

Strong, K., Bruner, M., Tarbell, T., Title, A. and Wolfson, C. J., 1994, "Trace - The transition region and coronal explorer", *Space Science Reviews*, **70**, 119–122. [DOI], [ADS].

SunPy Community, T., Mumford, S. J., Christe, S. et al., 2015, "SunPy - Python for solar physics", *Computational Science and Discovery*, **8**(1), 014009. [DOI], [ADS], [arXiv:1505.02563 [astro-ph.IM]].

Suzuki, T. K., 2011, "Self-consistent Simulations of Alfvén Wave Driven Winds from the Sun and Stars", *Space Science Reviews*, **158**, 339–363. [DOI], [ADS], [arXiv:1001.2400 [astro-ph.SR]].

Sych, R. and Nakariakov, V. M., 2014, "Wave dynamics in a sunspot umbra", *Astronomy & Astrophysics*, **569**, A72. [DOI], [ADS], [arXiv:1409.4530 [astro-ph.SR]].

Sych, R. A. and Nakariakov, V. M., 2008, "The Pixelised Wavelet Filtering Method to Study Waves and Oscillations in Time Sequences of Solar Atmospheric Images", *Solar Physics*, **248**, 395–408. [DOI], [ADS].

SymPy Development Team, 2014, "SymPy: Python library for symbolic mathematics".

Taroyan, Y. and Erdélyi, R., 2009, "Heating Diagnostics with MHD Waves", *Space Science Reviews*, **149**, 229–254. [DOI], [ADS].

Taroyan, Y., Erdélyi, R., Doyle, J. G. and Bradshaw, S. J., 2005, "Footpoint excitation of standing acoustic waves in coronal loops", *Astronomy & Astrophysics*, **438**, 713–720. [DOI], [ADS].

Terradas, J., Oliver, R. and Ballester, J. L., 2004, "Application of Statistical Techniques to the Analysis of Solar Coronal Oscillations", *The Astrophysical Journal*, **614**, 435–447. [DOI], [ADS].

Thiessen, G., 1950, "The structure of the sunspot-umbra", *The Observatory*, **70**, 234–235. [ADS].

Thomas, J. H. and Weiss, N. O., 2008, *Sunspots and Starspots*, Cambridge University Press. [ADS].

Thomas, J. H., Weiss, N. O., Tobias, S. M. and Brummell, N. H., 2002, "Downward pumping of magnetic flux as the cause of filamentary structures in sunspot penumbrae", *Nature*, **420**, 390–393. [ADS].

Thompson, B. J., Plunkett, S. P., Gurman, J. B., Newmark, J. S., St. Cyr, O. C. and Michels, D. J., 1998, "SOHO/EIT observations of an Earth-directed coronal mass ejection on May 12, 1997", *Geophysics Research Letters*, **25**, 2465–2468. [DOI], [ADS].

Tian, H., Curdt, W., Teriaca, L., Landi, E. and Marsch, E., 2009, "Solar transition region above sunspots", *Astronomy & Astrophysics*, **505**, 307–318. [DOI], [ADS], [arXiv:0906.2211 [astro-ph.SR]].

Tiwari, S. K., van Noort, M., Lagg, A. and Solanki, S. K., 2013, "Structure of sunspot penumbral filaments: a remarkable uniformity of properties", *Astronomy & Astrophysics*, **557**, A25. [DOI], [ADS], [arXiv:1307.3668 [astro-ph.SR]].

Toriumi, S., Iida, Y., Kusano, K., Bamba, Y. and Imada, S., 2014, "Formation of a Flare-Productive Active Region: Observation and Numerical Simulation of NOAA AR 11158", *Solar Physics*, **289**, 3351–3369. [DOI], [ADS], [arXiv:1403.4029 [astro-ph.SR]].

Torrence, C. and Compo, G. P., 1998, "A Practical Guide to Wavelet Analysis.", *Bulletin of the American Meteorological Society*, **79**, 61–78. [DOI], [ADS].

Tritschler, A., Schlichenmaier, R., Bellot Rubio, L. R., KAOS Team, Berkefeld, T. and Schelenz, T., 2004, "Two-dimensional spectroscopy of a sunspot. I. Properties of the penumbral fine structure", *Astronomy & Astrophysics*, **415**, 717–729. [DOI], [ADS].

Uitenbroek, H. and Tritschler, A., 2006, "The Contrast of Magnetic Elements in Synthetic CH- and CN-Band Images of Solar Magnetoconvection", *The Astrophysical Journal*, **639**, 525–533. [DOI], [ADS], [astro-ph/0510333].

van der Walt, Stéfan, Schönberger, Johannes L., Nunez-Iglesias, Juan, Boulogne, François, Warner, Joshua D., Yager, Neil, Gouillart, Emmanuelle and Yu, Tony, 2014, "scikit-image: image processing in Python", *PeerJ*, **2**, e453. [DOI].

van Noort, M., Rouppe van der Voort, L. and Löfdahl, M. G., 2005, "Solar Image Restoration By Use Of Multi-frame Blind De-convolution With Multiple Objects And Phase Diversity", *Solar Physics*, **228**, 191–215. [DOI], [ADS].

Vecchio, A., Cauzzi, G., Reardon, K. P., Janssen, K. and Rimmele, T., 2007, "Solar atmospheric oscillations and the chromospheric magnetic topology", *Astronomy & Astrophysics*, **461**, L1–L4. [DOI], [ADS], [astro-ph/0611206].

Veleda, D., Montagne, R. and Araujo, M., 2012, "Cross-Wavelet Bias Corrected by Normalizing Scales", *Journal of Atmospheric and Oceanic Technology*, **29**, 1401–1408. [DOI], [ADS].

Vernazza, J. E., Avrett, E. H. and Loeser, R., 1981, "Structure of the solar chromosphere. III - Models of the EUV brightness components of the quiet-sun", *The Astrophysical Journal, Supplement*, **45**, 635–725. [DOI], [ADS].

Verth, G. and Erdélyi, R., 2008, "Effect of longitudinal magnetic and density inhomogeneity on transversal coronal loop oscillations", *Astronomy & Astrophysics*, **486**, 1015–1022. [DOI], [ADS].

Verth, G., Erdélyi, R. and Jess, D. B., 2008, "Refined Magnetoseismological Technique for the Solar Corona", *The Astrophysical Journal, Letters*, **687**, L45–L48. [DOI], [ADS].

Verwichte, E., Nakariakov, V. M. and Cooper, F. C., 2005, "Transverse waves in a post-flare supra-arcade", *Astronomy & Astrophysics*, **430**, L65–L68. [DOI], [ADS].

Vigeesh, G., Fedun, V., Hasan, S. S. and Erdélyi, R., 2012, "Three-dimensional Simulations of Magnetohydrodynamic Waves in Magnetized Solar Atmosphere", *The Astrophysical Journal*, **755**, 18. [DOI], [ADS], [arXiv:1109.6471 [astro-ph.SR]].

Viticchié, B., Sánchez Almeida, J., Del Moro, D. and Berrilli, F., 2011, "Interpretation of HINODE SOT/SP asymmetric Stokes profiles observed in the quiet Sun network and internetwork", *Astronomy & Astrophysics*, **526**, A60. [DOI], [ADS], [arXiv:1009.6065 [astro-ph.SR]].

Vögler, A., Shelyag, S., Schüssler, M., Cattaneo, F., Emonet, T. and Linde, T., 2005, "Simulations of magneto-convection in the solar photosphere. Equations, methods, and results of the MURaM code", *Astronomy & Astrophysics*, **429**, 335–351. [DOI], [ADS].

Wang, T., 2011, "Standing Slow-Mode Waves in Hot Coronal Loops: Observations, Modeling, and Coronal Seismology", *Space Science Reviews*, **158**, 397–419. [DOI], [ADS], [arXiv:1011.2483 [astro-ph.SR]].

Wang, T. J., 2004, "Coronal Loop Oscillations: Overview of Recent Results In Observations", in *SOHO 13 Waves, Oscillations and Small-Scale Transients Events in the Solar Atmosphere: Joint View from SOHO and TRACE*, (Ed.) Lacoste, H., ESA Special Publication, 547, [ADS].

Wang, T. J., Solanki, S. K., Curdt, W., Innes, D. E., Dammasch, I. E. and Kliem, B., 2003, "Hot coronal loop oscillations observed with SUMER: Examples and statistics", *Astronomy & Astrophysics*, **406**, 1105–1121. [DOI], [ADS].

Wedemeyer-Böhm, S., Lagg, A. and Nordlund, Å., 2009, "Coupling from the Photosphere to the Chromosphere and the Corona", *Space Science Reviews*, **144**, 317–350. [DOI], [ADS], [arXiv:0809.0987].

Wedemeyer-Böhm, S., Scullion, E., Steiner, O., Rouppe van der Voort, L., de La Cruz Rodriguez, J., Fedun, V. and Erdélyi, R., 2012, "Magnetic tornadoes as energy channels into the solar corona", *Nature*, **486**, 505–508. [DOI], [ADS].

Williams, D. R., Phillips, K. J. H., Rudawy, P. et al., 2001, "High-frequency oscillations in a solar active region coronal loop", *Monthly Notices of the Royal Astronomical Society*, **326**, 428–436. [DOI], [ADS].

Williams, D. R., Mathioudakis, M., Gallagher, P. T., Phillips, K. J. H., McAteer, R. T. J., Keenan, F. P., Rudawy, P. and Katsiyannis, A. C., 2002, "An observational study of a magneto-acoustic wave in the solar corona", *Monthly Notices of the Royal Astronomical Society*, **336**, 747–752. [DOI], [ADS].

Wöger, F., von der Lühe, O. and Reardon, K., 2008, "Speckle interferometry with adaptive optics corrected solar data", *Astronomy & Astrophysics*, **488**, 375–381. [DOI], [ADS].

Woods, T. N., Eparvier, F. G., Hock, R. et al., 2012, "Extreme Ultraviolet Variability Experiment (EVE) on the Solar Dynamics Observatory (SDO): Overview of Science Objectives, Instrument Design, Data Products, and Model Developments", *Solar Physics*, **275**, 115–143. [DOI], [ADS].

Wu, Zhaohua and Huang, Norden E, 2009, "Ensemble empirical mode decomposition: a noise-assisted data analysis method", *Advances in adaptive data analysis*, **1**(01), 1–41.

Zaqarashvili, T. V. and Erdélyi, R., 2009, "Oscillations and Waves in Solar Spicules", *Space Science Reviews*, **149**, 355–388. [DOI], [ADS], [arXiv:0906.1783 [astro-ph.SR]].

Zeng, K. and He, M., 2004, "A simple boundary process technique for empirical mode decomposition", in *Geoscience and Remote Sensing Symposium, 2004. IGARSS '04. Proceedings. 2004 IEEE International*, 6, [DOI].

Zhugzhda, I. D. and Dzhalilov, N. S., 1982, "Transformation of magnetogravitational waves in the solar atmosphere", *Astronomy & Astrophysics*, **112**, 16–23. [ADS].

Zhugzhda, Y. D., 1973, "Resonance in a Semi-Infinite Isothermal Atmosphere", *The Astrophysical Journal, Letters*, **15**, 119. [ADS].

Zirin, H. and Stein, A., 1972, "Observations of Running Penumbral Waves", *The Astrophysical Journal, Letters*, **178**, L85. [DOI], [ADS].

Appendix A

Mathematical derivation

Chapter 4

In Chapter 4, the set of equations, Equations (4.1), (4.2), (4.3), (4.4), (4.5), and (4.6), are the ideal MHD equations that describe linear magneto-acoustic wave motions and are repeated below,

$$\rho_0 \frac{\partial v_r}{\partial t} = -\frac{\partial}{\partial r}\left(p_1 + \frac{B_0 b_z}{\mu_0}\right) + \frac{B_0}{\mu_0}\frac{\partial b_r}{\partial z}, \tag{A.1}$$

$$\rho_0 \frac{\partial v_z}{\partial t} = -\frac{\partial p_1}{\partial z}, \tag{A.2}$$

$$\frac{\partial b_r}{\partial t} = B_0 \frac{\partial v_r}{\partial z}, \tag{A.3}$$

$$\frac{\partial b_z}{\partial t} = -B_0 \frac{1}{r}\frac{\partial (r v_r)}{\partial r}, \tag{A.4}$$

$$\frac{\partial p_1}{\partial t} = -\rho_0 c_s^2 \left(\frac{1}{r}\frac{\partial (r v_r)}{\partial r} + \frac{\partial v_z}{\partial z}\right), \tag{A.5}$$

$$\frac{\partial \rho_1}{\partial t} = -\rho_0 \left(\frac{1}{r}\frac{\partial (r v_r)}{\partial r} + \frac{\partial v_z}{\partial z}\right). \tag{A.6}$$

Here, p is the gas pressure, ρ is the density and $\mathbf{b} = (b_r, b_\theta, b_z)$ is the perturbed magnetic field. We have assumed that the plasma motion is adiabatic. The subscripts 0 and 1 refer to unperturbed and perturbed states, respectively. The velocity perturbation is denoted as $\mathbf{v}_1 = (v_r, v_\theta, v_z)$.

We will assume that all the perturbed quantities have the form of a harmonic propagating wave, $v_r = \hat{v_r}\cos(kz - \omega t)$, where $\hat{v_r}$ is the amplitude of the perturbation and is a function of the radius, i.e., $A(r)$. With this information, it is possible to derive Equations (4.7), (4.8), (4.9), (4.10), (4.11) and (4.12).

To start, we can substitute the radial velocity perturbation into Equation (4.3) or (A.3) giving,

$$\omega \hat{b_r} \cancel{\sin(kz - \omega t)} = -B_0 k \hat{v_r} \cancel{\sin(kz - \omega t)} \tag{A.7}$$

$$\omega \hat{b_r} = -B_0 k \hat{v_r}, \tag{A.8}$$

$$\omega b_r = -B_0 k \hat{v_r} \cos(kz - \omega t), \tag{A.9}$$

$$\omega b_r = -B_0 k v_r, \tag{A.10}$$

which is Equation (4.7).

Next we can substitute the radial velocity perturbation into Equation (4.1) or (A.1) giving,

$$\rho_0 \omega \hat{v_r} \sin(kz - \omega t) = -\frac{\partial}{\partial r}\left(p_1 + \frac{B_0 b_z}{\mu_0}\right) + \frac{B_0}{\mu_0}\left(-\hat{b_r} k \sin(kz - \omega t)\right), \tag{A.11}$$

$$\left(\rho_0 \omega \hat{v_r} + \frac{B_0}{\mu_0}\hat{b_r} k\right)\sin(kz - \omega t) = -\frac{\partial}{\partial r}\left(p_1 + \frac{B_0 b_z}{\mu_0}\right). \tag{A.12}$$

As we know that $\hat{v_r} = A(r)$, and using Equation (A.8), we know that $\hat{b_r} = -\dfrac{B_0 k}{\omega} A(r)$, substituting these into Equation (A.12) gives,

$$\left(\rho_0 \omega A(r) - \frac{B_0^2 k^2}{\mu_0 \omega} A(r)\right)\sin(kz - \omega t) = -\frac{\partial}{\partial r}\left(p_1 + \frac{B_0 b_z}{\mu_0}\right), \tag{A.13}$$

$$\rho_0\left(\frac{B_0^2 k^2}{\mu_0 \omega \rho_0} - \omega\right) A(r)\sin(kz - \omega t) = \frac{\partial}{\partial r}\left(p_1 + \frac{B_0 b_z}{\mu_0}\right), \tag{A.14}$$

and since $v_A^2 = \dfrac{B_0^2}{\mu_0 \rho_0}$,

$$\rho_0\left(\frac{v_A^2 k^2}{\omega} - \omega\right) A(r)\sin(kz - \omega t) = \frac{\partial}{\partial r}\left(p_1 + \frac{B_0 b_z}{\mu_0}\right), \tag{A.15}$$

which is Equation (4.8).

Equation (4.2) or (A.2) is the same as Equation (4.9), so no further work is required.

If we integrate Equation (4.3) or (A.3), with respect to time,

$$\frac{\partial b_z}{\partial t} = -B_0 \frac{1}{r} \frac{\partial (r v_r)}{\partial r}, \tag{A.16}$$

$$b_z = \int -B_0 \frac{1}{r} \frac{\partial (r v_r)}{\partial r} dt, \tag{A.17}$$

$$b_z = -\frac{B_0}{r} \int \frac{\partial (rA(r)\cos(kz - \omega t))}{\partial r} dt, \tag{A.18}$$

$$b_z = -\frac{B_0}{r} \frac{\partial (rA(r))}{\partial r} \int \cos(kz - \omega t) dt, \tag{A.19}$$

$$b_z = -\frac{B_0}{r} \frac{\partial (rA(r))}{\partial r} \left(\frac{-1}{\omega}\right) \sin(kz - \omega t) dt, \tag{A.20}$$

$$b_z = \frac{B_0}{r\omega} \frac{\partial (rA(r))}{\partial r} \sin(kz - \omega t) dt, \tag{A.21}$$

which is Equation (4.10).

Next, using Equations (4.5) and (4.6) or Equations (A.5) and (A.6) and multiplying Equation (4.6) or (A.6) by c_s^2, it can be shown that,

$$\frac{\partial p_1}{\partial t} = c_s^2 \frac{\partial \rho_1}{\partial t} = -\rho_0 c_s^2 \left(\frac{1}{r} \frac{\partial (r v_r)}{\partial r} + \frac{\partial v_z}{\partial z} \right), \tag{A.22}$$

which is Equation (4.11).

Finally, integrating Equation (4.11) or (A.22) with respect to time gives,

$$p_1 = c_s^2 \rho_1 = \frac{-\rho_0 c_s^2}{r} \int \frac{\partial (r v_r)}{\partial r} dt - \rho_0 c_s^2 \int \frac{\partial v_z}{\partial z} dt, \tag{A.23}$$

$$= \frac{-\rho_0 c_s^2}{r} \int \frac{\partial (r(A(r))\cos(kz - \omega t))}{\partial r} dt - \rho_0 c_s^2 \int \frac{\partial v_z}{\partial z} dt, \tag{A.24}$$

$$= \frac{-\rho_0 c_s^2}{r} \frac{\partial (r(A(r))}{\partial r} \int \cos(kz - \omega t)) dt - \rho_0 c_s^2 \int \frac{\partial v_z}{\partial z} dt. \tag{A.25}$$

Integrating Equation (4.9) with respect to time gives,

$$v_z = \int -\frac{1}{\rho} \frac{\partial p_1}{\partial z} dt,$$

and then substituting this into Equation (A.25) gives,

$$p_1 = c_s^2 \rho_1 = \frac{\rho_0 c_s^2}{r\omega} \frac{\partial (r(A(r))}{\partial r} \sin(kz - \omega t) + \frac{\cancel{\rho_0} c_s^2}{\cancel{\rho_0}} \int \frac{\partial}{\partial z} \left(\int \frac{\partial p_1}{\partial z} dt \right) dt, \tag{A.26}$$

$$= \frac{\rho_0 c_s^2}{r\omega} \frac{\partial (r(A(r))}{\partial r} \sin(kz - \omega t) + c_s^2 \int \int \frac{\partial^2 p_1}{\partial z^2} dt dt. \tag{A.27}$$

If we let the pressure and density perturbations to be of the form, $p_1 = \hat{p_1}\mathrm{q}(kz - \omega t)$ and $\rho_1 = \hat{\rho_1}\mathrm{q}(kz - \omega t)$, respectively, where q is representative of a harmonic wave, i.e., it could be cos, sin or some combination, for example, $\mathrm{q} = a\sin(kz - \omega t) + b\cos(kz - \omega t)$. Then the right most term of Equation (A.27) will become,

$$\int\int \frac{\partial^2 \mathrm{q}}{\partial z^2} dtdt, \tag{A.28}$$

$$\frac{\partial^2 q}{\partial z^2} = -k^2 \mathrm{q}, \tag{A.29}$$

$$\int\int -k^2 \mathrm{q} dtdt = \frac{k^2}{\omega^2}\mathrm{q}. \tag{A.30}$$

This is because of the following,

$$\frac{\partial^2 \sin(kz - \omega t)}{\partial z^2} = -k^2 \sin(kz - \omega t), \tag{A.31}$$

$$\frac{\partial^2 \cos(kz - \omega t)}{\partial z^2} = -k^2 \cos(kz - \omega t), \tag{A.32}$$

$$\int\int \sin(kz - \omega t) dtdt = -\frac{1}{\omega^2}\sin(kz - \omega t), \tag{A.33}$$

$$\int\int \cos(kz - \omega t) dtdt = -\frac{1}{\omega^2}\cos(kz - \omega t), \tag{A.34}$$

and this is still valid for any linear combination of these terms.

Thus Equation (A.27) will become,

$$\hat{p_1}\mathrm{q} = \frac{\rho_0 c_s^2}{r\omega}\frac{\partial(r(A(r))}{\partial r}\sin(kz - \omega t) + \frac{c_s^2 k^2}{\omega^2}\hat{p_1}\mathrm{q}, \tag{A.35}$$

$$\hat{p_1}\mathrm{q}\left(1 - \frac{c_s^2 k^2}{\omega^2}\right) = \frac{\rho_0 c_s^2}{r\omega}\frac{\partial(r(A(r))}{\partial r}\sin(kz - \omega t), \tag{A.36}$$

$$p_1\left(1 - \frac{c_s^2 k^2}{\omega^2}\right) = \frac{\rho_0 c_s^2}{r\omega}\frac{\partial(r(A(r))}{\partial r}\sin(kz - \omega t), \tag{A.37}$$

$$p_1 = \frac{\rho_0 c_s^2}{\frac{\omega}{\omega^2}(\omega^2 - c_s^2 k^2)}\frac{1}{r}\frac{\partial(r(A(r))}{\partial r}\sin(kz - \omega t), \tag{A.38}$$

$$p_1 = -\frac{\rho_0 c_s^2 \omega}{c_s^2 k^2 - \omega^2}\frac{1}{r}\frac{\partial(r(A(r))}{\partial r}\sin(kz - \omega t), \tag{A.39}$$

which is Equation (4.12).